2017

Implosion and Blast Response of Metallic and Composite Structures in Underwater Environments

Helio David Sega Matos
University of Rhode Island, hmatos@uri.edu

IMPLOSION AND BLAST RESPONSE OF METALLIC AND COMPOSITE STRUCTURES IN UNDERWATER ENVIRONMENTS

BY

HELIO DAVID SEGA MATOS

A DISSERTATION SUBMITTED IN PARTIAL FULFILLMENT OF THE REQUIREMENTS FOR THE DEGREE OF

DOCTOR OF PHILOSOPHY

IN

MECHANICAL ENGINEERING AND APPLIED MECHANICS

UNIVERSITY OF RHODE ISLAND

2017

DOCTOR OF PHILOSOPHY DISSERTATION

OF

HELIO DAVID SEGA MATOS

APPROVED:

Dissertation Committee:

Major Professor Arun Shukla

James LeBlanc

James Miller

Nasser H. Zawia
DEAN OF THE GRADUATE SCHOOL

UNIVERSITY OF RHODE ISLAND

2017

ABSTRACT

Six different experimental studies were conducted to evaluate the dynamic response of marine structures. These studies examine the: implosion performance of polyurea coated aluminum shells; implosion process of marine grade metallic structures; implosion mechanics within a confining environment; the response of confined blast-initiated implosions; generation and mitigation of implosion induced hammer waves; and behavior of artificially aged composite structures subjected to blast loads. During the experiments, two high-speed cameras are used to record the event, and underwater pressure transducers are used to measure the pressure signatures. A high contrast speckle pattern is placed on the specimen so three-dimensional Digital Image Correlation can measure full field surface displacement, velocities, and strains. When explosives are in use, a third high-speed camera records the explosive's behavior and bubble mechanics. For the artificially aged composite study, a Coupled Eulerian-Lagrange finite element model was created to supplement the experimental results. The findings of these studies show that: polyurea coatings can drastically reduce the emitted energy of an implosion event; marine grade metals can release less energy during an implosion event if fracture is present; confined implosions have different collapse mechanics than free-field implosions; confined blast-initiated implosions can have devastating pressure signatures if the hammer pressure is in phase with the bubble pulse; high pressures from water hammer waves are mitigated if a sacrificial foam material is used at the hammer location; and weathered composites have a lower blast performance due to degraded material properties.

ACKNOWLEDGEMENTS

First and foremost I would like to thank Dr. Arun Shukla for his continuous guidance and support throughout my research. His enthusiasm, patience, and adamant work ethic have truly been motivating throughout my doctoral research. It has been an honor be one of Dr. Shukla's Ph.D. students. Moreover, I would like to thank Dr. James LeBlanc, Dr. James Miller, Dr. Hongyan Yuan, and Dr. Gopu Potty for providing me with invaluable support towards the completion of my Ph.D. Additionally, I would like to thank Sachin Gupta for being a friend and coauthor on many of my research projects (especially in Chapter 3 where he is responsible for half of the chapter) as well as all my other colleagues in the Dynamic Photomechanics Laboratory that has helped during my studies; specifically: Prathmesh Parrikar, Michael Pinto, Shyamal Kishore, Carlos Javier, Nicholas Denardo, Emad Makki, Koray Senol, Erin Gauch, Jefferson Wright, Craig Tilton, Christopher Shillings, Daniel Clarkin, Christopher Salazar, and Estefany Mejia. Also, I would like to thank everyone in the mechanical engineering department for their instrumental support especially: Dr. David Chelidze, Dr. Carl-Ernst Rousseau, Joe Gomez, Dave Ferriera, Jim Byrnes, Rob D'Ambrosca, Jen Cerullo, A.J. Bothun, Nancy Dubee, Nancy Santucci, Sally Marinelli, and Donna Mattera. Lastly, I am thankful for the financial support provided by the Office of Naval Research (ONR) under Grant Numbers N00014-12-1-0382 and N00014-15-1-2046 as well as the Naval Engineering Education Consortium (NEEC) under Grant Number N00174-16-C-0012.

PREFACE

This dissertation is submitted for the degree of Doctor of Philosophy in Mechanical Engineering and Applied Mechanics at the University of Rhode Island. The research shown herein is original and was conducted under the supervision of Professor Arun Shukla in the Department of Mechanical, Industrial & Systems Engineering. This work is presented in a manuscript format that consists of six chapters. Three of the chapters (Chapters 1, 3, and 4) have been published in the International Journal of Solids and Structures, The Journal of the Acoustical Society of America, and Mechanics of Materials (respectively). The remaining chapters (Chapters 2, 5, and 6) are being prepared for publication and will be submitted after the completion of this dissertation.

All the chapters presented are about the dynamic behavior of underwater marine structures in extreme environments. These harsh environments consist of, high hydrostatic pressures, explosive/blast loads, and a combination of both. This research was performed to increase the current knowledge base in the underwater dynamic behavior of mechanical components, so better and safer naval structures are designed and produced in the future. Most of the research techniques and conclusions of this research are not limited to the marine sector and could be applied to other industries such as automotive and aerospace.

Helio Matos

February 2017

TABLE OF CONTENTS

LIST OF TABLES

CHAPTER 6

LIST OF FIGURES

CHAPTER 1

CHAPTER 2

CHAPTER 3

CHAPTER 4

CHAPTER 5

CHAPTER 6

CHAPTER 1. Mitigation of Implosion Energy from Aluminum Structures

by

Helio Matos and Arun Shukla

Dynamic Photo Mechanics Laboratory, Department of Mechanical, Industrial and Systems Engineering, University of Rhode Island, Kingston, RI 02881

Published in the International Journal of Solids and Structures

Matos, H., & Shukla, A. (2016). Mitigation of implosion energy from aluminum structures. International Journal of Solids and Structures, 100-101, 566-574. doi:10.1016/j.ijsolstr.2016.09.030

Abstract

This study aims to develop an experimental scheme to determine the localized energy emitted during the dynamic collapse of aluminum structures. Upon collapse, these structures release damaging pressure pulses into the surrounding fluid; to mitigate this effect, the structures are coated with polyurea. The new energy scheme analyzes the energy emission from coated structures. Specifically, aluminum tubular structures with polyurea coatings on their interiors or exteriors are used. Furthermore, the technique combines the information obtained from pressure sensors, located near the collapsing structure, and high-speed images taken during the collapse event. These images are processed through a 3D Digital Image Correlation technique to obtain full deformation and velocity fields. Results show that the energy history can be successfully obtained experimentally. Moreover, the energy emitted from coated aluminum structures is significantly less than the uncoated structures; more so with interior coated structures, and doubling the coating volume does not significantly improve this mitigation effect. Additionally, collapse pressure does not have a direct relationship with the energy released during the implosion process; even though buckling velocities are proportional to collapse pressure. However, collapse volume does have a direct relationship with energy and is the dominant factor in determining the energy release.

1. Introduction

Submerged hollow structures will become unstable once a critical depth is reached. At this depth, environmental pressures cause the structure to rapidly collapse

onto itself (this process is known as dynamic buckling or implosion). During the collapse, the kinetic energy of the surrounding fluid increases and its potential energy decreases, causing a drop in local pressure. When opposite sides of the structure come into contact with one another, sharp acoustic pulses are released. Soon after, the water that surrounds the structure comes to a sudden stop which leads to an abrupt change in momentum, resulting in a considerably high-pressure pulse [1-5].

Implosion has been of interest since the mid-1900s [3-5]. However, there is one key accident that renewed the interest in this topic. This accident was the 2001 Super-Kamiokande laboratory accident in Japan where one photomultiplier tube imploded, and the pressure pulses from this implosion caused adjacent tubes to implode; leading to a chain reaction that destroyed 7000 photomultiplier tubes [6]. More recently in 2014, the multi-million dollar underwater vehicle, Nereus, imploded off the coast of New Zealand [7]. These recent events highlight implosion as an ongoing issue.

Early work on implosion characterized the acoustic pulses emitted during the collapse of glass structures, as well as their potential to damage nearby structures [1, 3]. This work led to the creation of robust computational models (for fluid-structure interaction during implosion) for the implosion of metallic structures [2]. Later work analyzed the implosion of aluminum structures with varying lengths to produce higher modes of failure (modes II and IV) [8]. Also, an experimental study on brass structures was made with varying geometries to examine the effect of collapse modes on the emitted pressure pulses [9]. Recently, the pressure pulses from imploding structures were linked to full deformation and velocity fields that were captured

through a Digital Image Correlation (DIC) technique coupled with high-speed photography [10-12].

Even though full-field measures can be obtained from DIC, only localized measures were used in the discussion and results of previous studies due to the human limitation of comparing four-dimensional fields (three spatial and one temporal). For this reason, most of the information available from the full-field analysis goes unused. To date, there is no work done in the mitigation of the energy emitted during implosion, or in measuring the kinetic energy on the surface of a DIC specimen [13]. Polyurea has gained research interest regarding blast mitigation due to its dynamic properties, such as its stiffness increase at high strain rates. Some of the work available on energy mitigation through polyurea coating is on blast/dynamic loading on structures [14-16]. More recently available is a study on coating thin-walled tubular structures with polyurea to mitigate longitudinal acceleration during crushing due to blast loading [17].

This study aims to develop an experimental scheme to determine the localized energy history emitted during the implosion of aluminum structures. Moreover, a numerical method will be established to combine the three spatial domains from the implosion DIC analysis into a volumetric measure. Finally, the new energy scheme will be used to analyze the mitigation effects of polyurea coated aluminum structures and to create an estimation method for the energy released during an implosion process.

2. Experimental Details

2.1. Specimen Geometry and Facility

Each specimen is comprised of a 6061-T6 Al tubular structure with 63.5 mm (2.5”) diameter and 381mm (15”) length (see Figure 1.1). The specimens are sealed from both ends with aluminum end-caps to prevent water penetration. Therefore, during the experiments high-pressure water surrounds the specimen while low-pressure air resides in the specimen.

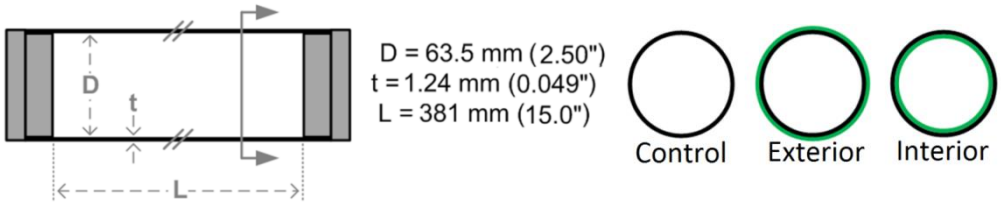

(a) **(b)**

Figure 1.1 Specimen details; (a) tubular structure dimensions and (b) polyurea coating locations

The experimental facility consists of a 2.1 m semi-spherical pressure vessel and two high-speed cameras. As shown in Figure 1.2, the specimen is suspended at the center of the tank, and then the tank is filled with water and pressurized with compressed nitrogen gas which is introduced into the top of the tank. This simulates increasing water depths in an underwater environment. For the experiments performed in this study, all specimens imploded at 1.69 +/- 0.03 MPa (equivalent to 164 m below sea level).

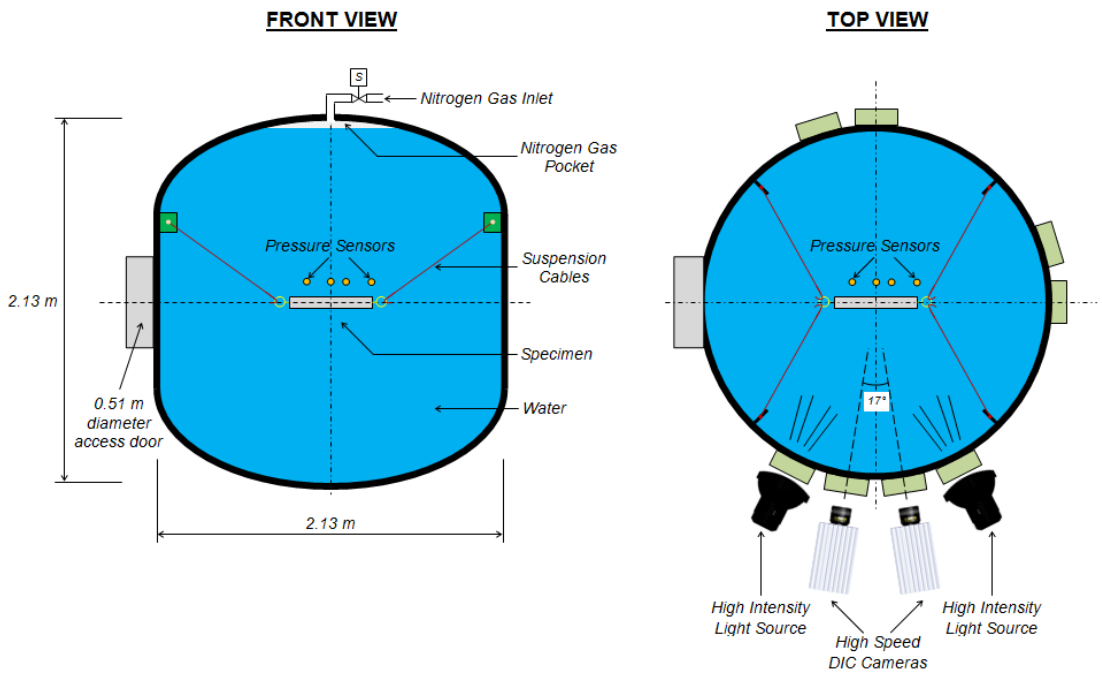

Figure 1.2. Detailed schematic of the implosion experimental facility

During the implosion event, eight pressure sensors (PCB 138A05 from PCB Piezotronics, Inc., Depew, NY) capture localized pressure histories at 2 MHz (through an Astro-med Dash® 8HF-HS from Astro-Med Inc., West Warwick, RI). The sensors are located above and behind the specimen at an 84 mm distance from the surface of the specimen. Also, Sensor 1 and Sensor 5 are mid-length of the tube (see Figure 1.3). Moreover, the high-speed cameras (Photron SA1 from Photron USA, Inc.) record the entire implosion event. The stereo images captured are then used to perform the DIC analysis (with the black and white speckled pattern shown in Figure 1.3) and obtain the full displacement and velocity fields. Previous work shows the DIC analysis error (for these experiments) to be below 2.5% (regarding out and in-plane displacements) [10].

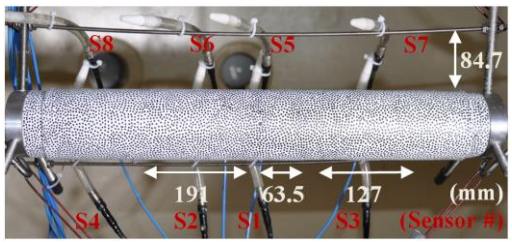

Figure 1.3 Specimen setup of exterior coated tube inside the pressure vessel

2.2. Polyurea Coating

The polyurea used was the commercially available product HM-VK™ from Specialty Products, Inc. (Lakewood, WA). This is a two-part polyurea that was manually applied over the aluminum tube as it rotated longitudinally. Tape was used at each end of the tube (set to a predetermined thickness) as a scraper guide to wipe off the excess polyurea. Figure 1.4 shows the set up for outside coating. For inside coating, the entire setup is angled so the polyurea can be poured from the center guide's end.

Specimens with polyurea coatings have a uniform coating placed outside or inside of the tube. There are two different coating thicknesses (based on volume ratios) for the outside and the inside coating. In total, there are five cases analyzed in this study as shown in Table 1.1. Each case studied has been repeated three times to ensure repeatability (discussed in later sections). Also, the inner, V_i, and outer, V_o, volumes shown in Table 1.1 represent air inside the specimen and water displacement (from a submerged specimen) respectively.

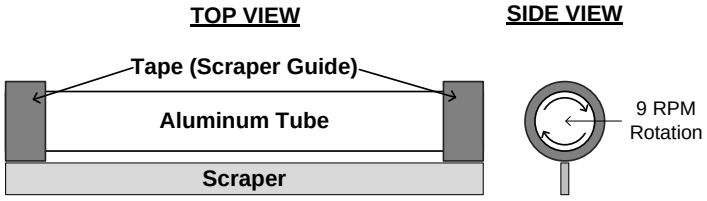

Figure 1.4 Polyurea coating setup

Table 1.1 Experimental series details

Cases	Polyurea Coating	Polyurea:Aluminum Volume Ratio	V_i (cc)	V_o (cc)
NC	None	N.A.	1114	1207
EC1	Exterior	1:1	1114	1299
EC2	Exterior	2:1	1114	1392
IC1	Interior	1:1	1021	1207
IC2	Interior	2:1	929	1207

3. Results and Discussion

3.1. Pressure and Impulse

The tubular structure's cross section during implosion is illustrated alongside local dynamic pressure in Figure 1.5 (a). The y-axis in this figure is in terms of dynamic pressure where the value of 0 represents hydrostatic pressure (1.68 +/- 0.01 MPa). The pressure history can be broken down into three main stages: I) Structure becomes unstable, II) emission of low-pressure pulses due to the decrease in potential energy, and III) emission of high-pressure pulses due to the abrupt change in water momentum. Also, immediately after the low-pressure region, there is a high acoustic spike (at t=0 ms) caused by structural contact. For structures with high diameter/thickness ratio (such as the one in this study), a second acoustic spike is seen when the opposing walls of the structure come into full contact. Figure 1.5 (b) shows the captured images that can be associated with the pressure history in Figure 1.5 (a). By comparing the images of *t=0* and *t = 0.15 ms*, it can be determined that the center cross section of the tube completely flattens from a "figure 8" shape, which is the cause of the second acoustic spike. Note that Figure 1.5 (b) is an in-plane image that illustrates out-of-plane deformation; hence, by focusing on the y-dimension change, the out-of-plane change can be intuitively understood.

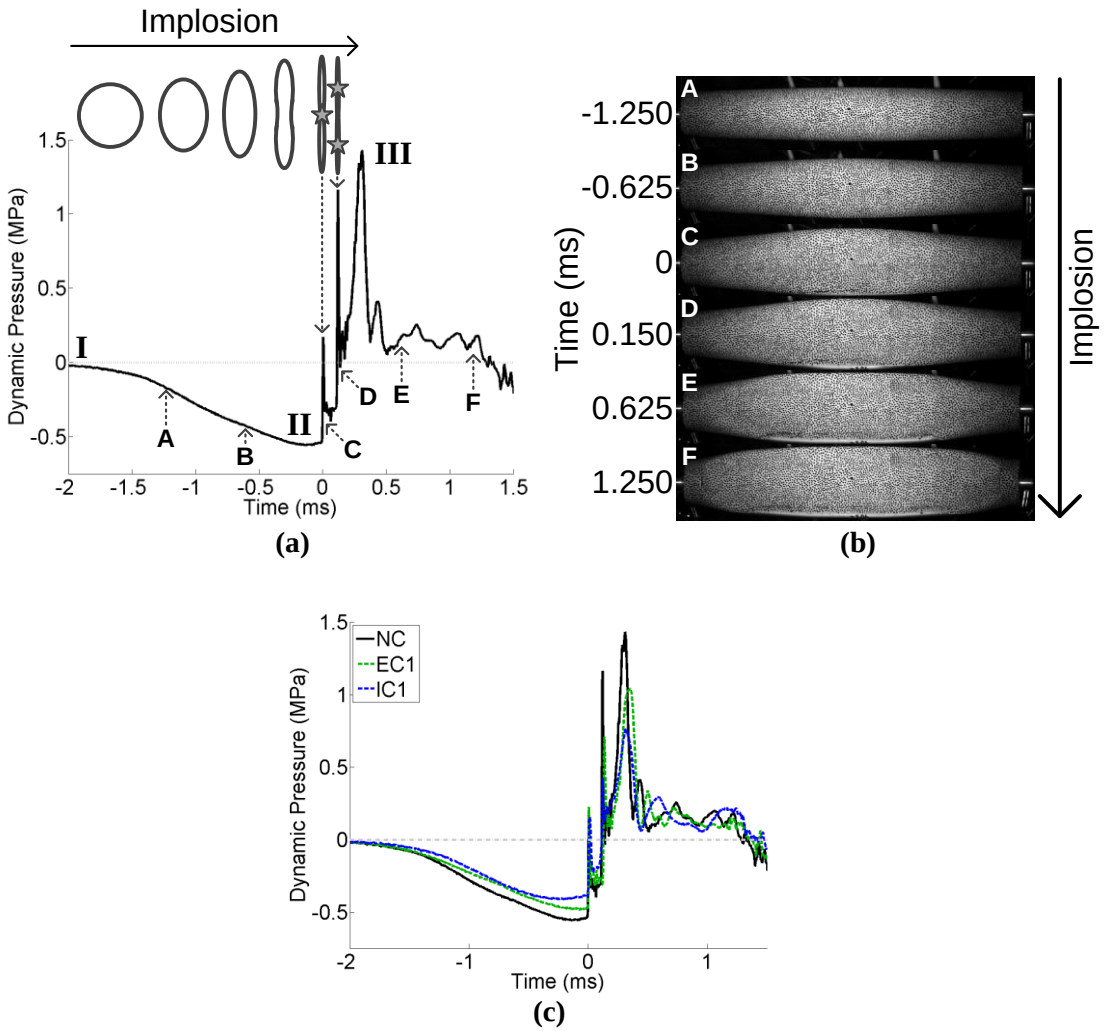

Figure 1.5 Dynamic pressure histories taken from sensor 1; (a) of the NC case and tubular cross section during implosion; (b) still images that correlate with the pressure history; and (c) of three major cases studied

Figure 1.5 (c) illustrates the effects of polyurea coating through the 1 polyurea: 1 aluminum volume cases in comparison to the NC (no coating) case. Applying coatings to the exterior or the interior of the structure show mitigating effects to the low and high-pressure regions of the pressure pulse. Interior coating has a stronger effect then the exterior coating. By doubling the coating volumes (not shown in the Figure) this effect slightly increases.

The pressure data can be better represented in terms of impulse by simply integrating the signal. Doing so will take into account the duration of acoustic spikes as well as their magnitude. After integration, an areal impulse is given in terms of $Pa{\cdot}s$. This areal impulse is a good representation of the force that adjacent structures to the implodable could experience [1, 2]. Figure 1.6 (a) shows the areal impulse of all five cases taken from sensor 1. It is shown that the structures coated with polyurea have the same behavior as the non-coated structure. Also shown is the diminishing of impulse with added coating (more so with interior coating). The maximum impulse for all five cases is given in Table 1.3 as I_{max}.

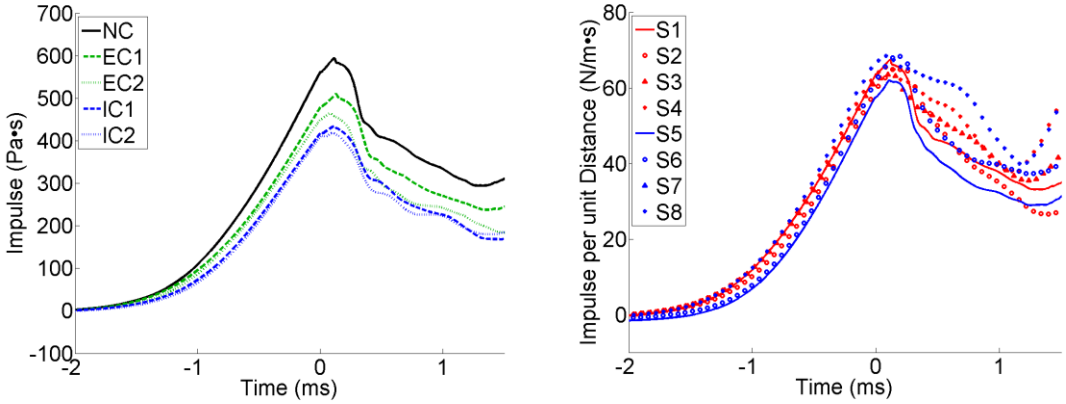

Figure 1.6 Impulse histories obtained from pressure sensors; (a) sensor 1's areal impulse histories for all five cases; and (b) all sensors' normalized impulse history for the NC case

A closer look can be taken in the impulse data if multiplied by the distance from the center of the structure to the sensor location, R_s. This new impulse value will be referred to as normalized impulse, I_N. Figure 1.6 (b) shows all eight I_N histories for the NC case (see Figure 1.3 for sensor locations). It is seen on this plot that most of the normalized history and peak values (of 65.8 +/- 4.2 %) are in good correlations. This

implies that the pressure wave is traveling with an attenuation factor of $1/R$, in turn confirming previous assertions [2, 18] of a spherical wave [19].

3.2. Collapse Velocities

The reduction in low pressures waves is accompanied by lower collapse velocities. The EC1 and IC1 (exterior and interior coating with 1:1 volume ratio respectively) cases are seen to have ~15 and 25% reduction in minimum pressure when compared to the NC case, as shown in Figure 1.5 (c). However, the CenterPoint velocities for all five cases are comparable as depicted by their maximum velocities in Table 1.2. The polyurea is a strain rate sensitive material, and it can reduce the bulking velocities during high strain rates. The CenterPoint is located in the "valley" of the tube's cross section, which is a region that experiences relatively low strain rates. It is in the "lobes" of the tube's cross section that high strain rates are expected to occur. Additionally, this specific tubular geometry tends to collapse into a "figure 8" shape before flattening completely; hence, in this case, the collapse resistance from the polyurea happens mostly near the lobes. However there is still a small reduction in maximum CenterPoint velocity (up to 10%), and this discrepancy increases as measurements are taken closer to the lobes. This is predominantly the cause of the initial reduction in low-pressure waves seen in Figure 1.5 (c) for $t<0$. Moreover, there is a compressibility effect at the lobe locations for the IC cases that impede complete hinging, leading to even lower pressures as seen in Figure 1.5 (c) at $-0.5\ ms < t < 0$.

Table 1.2 CenterPoint and buckle velocities

Cases	Maximum Local Center Velocity (m/s)	Mean Buckle Velocity (m/s)
NC	22.5 +/- 1.4	249 +/- 5
EC1	19.6 +/- 2.0	217 +/- 4
EX2	21.1 +/- 1.3	207 +/- 4
IC1	20.8 +/- 1.8	198 +/- 3
IC2	20.3 +/- 1.1	179 +/- 6

After wall contact, the buckle starts to propagate longitudinally. This longitudinal propagation is ~10x faster than the wall collapse velocity as shown by the mean buckle velocity for each case in Table 1.2. The highest strain rates during collapse can be found at the longitudinal buckle front. Thus, it is during this time that the strain rate sensitive properties of the polyurea become important. The polyurea coating slows down the longitudinal buckle propagation by ~15% and ~25% for the exterior and interior coated cases respectively. This change in velocity leads to the reduction in high-pressure waves seen in Figure 1.5 (c) for $t>0$.

3.3. Volumetric Flow

Through the DIC technique, displacement and velocity information are obtained from the images taken during the experiments. Figure 1.7 (a) (left) illustrates how the full-field out-of-plane (z-direction) displacements, for the NC case, looks after the DIC analysis. The specimen initially buckles from the center until it makes structural contact, and then the buckle propagates longitudinally.

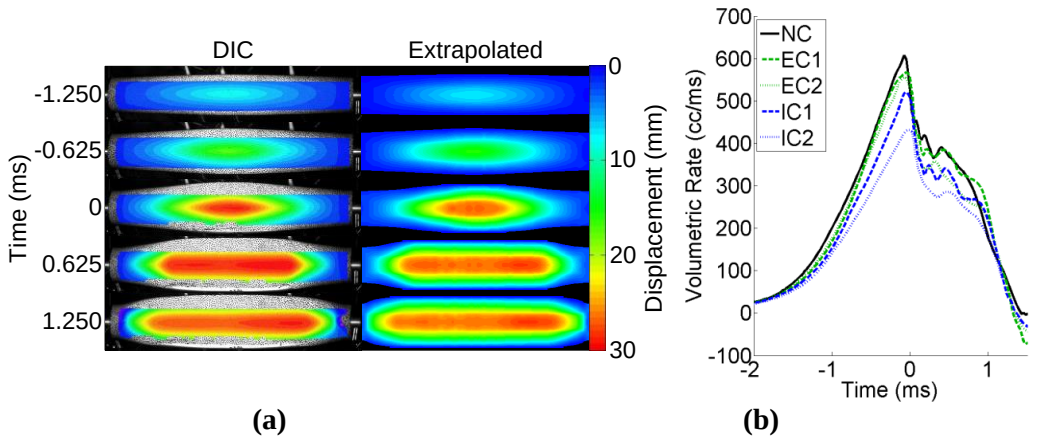

Figure 1.7 DIC analysis results; (a) displacement & extrapolated images of the DIC analysis of the NC case; and (b) volumetric flow rate for all five cases

To better summarize this information, both in-plane (x and y directions) and out-of-plane spatial domains are combined into a volumetric unit through a numerical scheme developed. The scheme extrapolates missing/lost DIC edge information through the collapse as illustrated in Figure 1.7 (a) (right). This is easily attainable when there is symmetry in the xy-plane that lies at the structural center (verified during postmortems), especially for mode II collapses.

The numerical scheme measures volume as a function of time, $V(t)$, with a series of horizontal lines from the DIC displacements that is extracted from the center, $W_0(x=0:L, y=0, t)$, towards the top or bottom, $W_1(x=0:L, y= y_1, t)$, $W_2(x=0:L, y= y_2, t)$ …. $W_n(x=0:L, y= y_n, t)$ (only one direction suffices due to symmetry). Since edge information, and information from locations not seen in the first reference image is always lost during DIC analysis, an additional line is artificially created as compensation, $W_{end}(x=0:L, y=1/2\ W_0|_x, t)$. This additional line takes into account that for mode II collapses, the displacements of the lobes of the tube is ~1/2 of the valleys'. Also, W_{end} emulates the deformation shape of the tubular structure seen in Figure 1.7

(a). For each time value, a piecewise cubic interpolation is done vertically across the horizontal lines to complete the deformation contour. With a complete contour, the volume at each time value can be obtained, and *V(t)* can be compiled.

There is only a need for three horizontal lines for convergence within 2% error since the deformation contour is relatively simple. This error can be obtained by measuring the collapsed (residual) volume post-experiment and compare it to the final value of *V*. Moreover, *V* can be differentiated with respect to time to obtain volumetric flow rate, $\dot{V}$. The volumetric flow can be used as a macro visualization of the implosion process.

Figure 1.7 (b) shows $\dot{V}$ for all five cases. It is seen that there is little change in flow for the NC, EC1 and EC2 cases. Also, following structural contact at *t=0*, there is a significant drop in flow followed by a gradual drop until contact with the end-caps is made near *t = 1.5 ms*. For more details, a summary of maximum volumes and volume flow rates can be seen in Table 1.3 as V_{max} and $\dot{V}_{max}$ respectively.

Table 1.3 Summary of experimental results

Cases	% Mass Change	P_{cr} (MPa)	I_{max} (Pa·s)	V_{max} (cc)	$\dot{V}_{max}$ (cc/ms)	E_1 (J)	E_2 (J)	E_3 (%)
NC	N.A.	1.68 +/- 0.01	595 +/- 37	924 +/- 27	608 +/- 24	320 +/- 5	267 +/- 11	N.A.
EC1	31.6 +/- 1.0	1.67 +/- 0.03	509 +/- 24	913 +/- 31	567 +/- 29	266 +/- 7	197 +/- 7	83.1 +/- 3.2
EC2	62.1 +/- 0.3	1.70 +/- 0.02	464 +/- 15	907 +/- 29	555 +/- 15	239 +/- 5	163 +/- 8	75.0 +/- 1.9
IC1	33.9 +/- 0.7	1.69 +/- 0.01	433 +/- 21	814 +/- 11	521 +/- 18	205 +/- 4	142 +/- 7	64.1 +/- 2.5
IC2	63.0 +/- 0.6	1.72 +/- 0.04	418 +/- 17	726 +/- 17	431 +/- 14	177 +/- 6	132 +/- 5	55.3 +/- 2.9

E_1: Peak energy of the energy history obtained from the Volumetric Flow Method at 116.45 mm away from the structural center.
E_2: Energy obtained from the Flow Energy Method at 116.45 mm away from the structural center.
E_3: Percentage of energy emitted from the coated structures with respect to the NC case.

3.4. Fluid Energy

The areal impulse can be combined with the volumetric rate of change to give an energy measurement as a function of time as shown in equation (1). This energy is directly related to the kinetic energy of the moving fluid. Also, since the impulse data used is from a sensor, then the energy obtained is a localized measure of energy. However, since pressure travels at $1/R$ spherically then energy will travel at $1/R^2$, also spherically [19]; meaning that the energy value reported will be the same on the surface of a sphere with radius equal to the sensor distance from the structural center.

$$I(t) \cdot \dot{V}(t) = E(t) \tag{1}$$

Equation (1) is only valid with the assumption that the fluid flow of the specimen is the same as of the fluid; in other words, any compressibility effect is neglected. In the case of high collapse pressure implosions, where surface cavitation is often common, this method could over predict the energy emitted.

The fluid energy during implosion as a function of time is shown in Figure 1.8 (a) (obtained from sensor 1). The NC case shows more energy release than the coated cases, as expected. Since the time span of energy release is roughly the same, peak energy values can be used as a representation of the polyurea coating's mitigation effects (performance). Interestingly, since the values for all cases scales equally at $1/R^2$, then the performance shown as E_3 in Table 1.3 is the same anywhere in the fluid (neglecting viscous losses). Moreover, Figure 1.8 (a) illustrates that doubling the coating volume does not drastically change the performance of the polyurea.

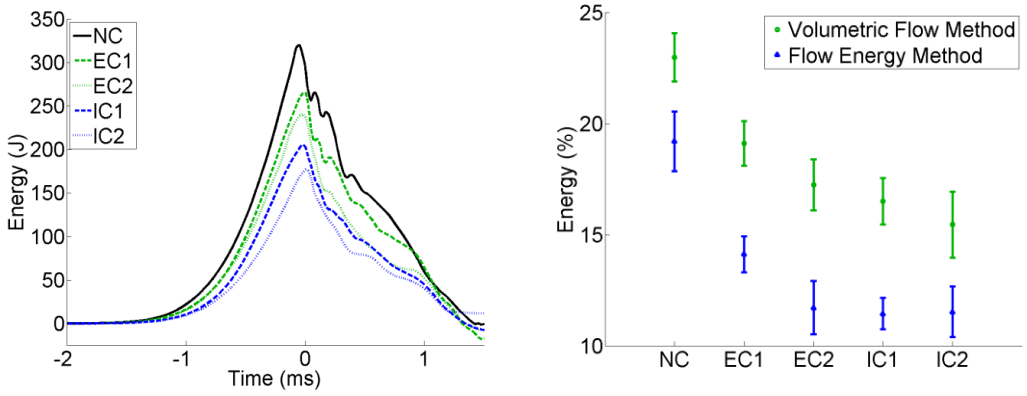

(a) **(b)**

Figure 1.8 Energy emitted during implosion; (a) energy as a function of time of all five cases measured from sensor 1; and (b) energy method comparison for all five cases taken from sensor 1 location

3.5. Energy Methods Comparison

Previous work shows a method of obtaining the maximum energy release during an implosion by using the peak areal impulse [18, 20] as shown in equation (2). Moreover, this value is taken as a percentage of the total available potential energy, E_{max}, prior implosion as shown in equation (3). This method will be referred to as Flow Energy Method, while the method described in this study will be referred to as Volumetric Flow Method. Both methods are compared in Figure 1.8 (b).

$$E = \left[\frac{I^2}{2\rho_0 R_s}\right][4\pi R_s^2] \tag{2}$$

$$E_{max} = P_{cr} V_c \tag{3}$$

In equation (2), the $[4\pi R_s^2]$ factor represents the surface area of a sphere with radius initializing from the structural center and ρ_0 is the fluid density. Also, the potential energy in the previous study was obtained with the volume displaced by the implodable (outer volume in Table 1.1); but the displaced volume (or collapse volume,

V_c) is used instead (inner volume in Table 1.1 minus remaining volume post implosion) to compensate for the polyurea in the interior coated tubes.

Both methods in Figure 1.8 (b) are apart by ~4% of the total available potential energy. As mentioned earlier, if cavitation was present during implosion the Volumetric Flow Method could over predict the energy emitted. In contrast, if cavitation was present, the Flow Energy Method could under predict the energy due to the density term in equation (2). Moreover, the percentage in Figure 1.8 (b) could be scaled by R_s^2/R^2, where R is the distance in interest and R_s is the sensor distance (116.45 mm in this case). By scaling with an $R>R_s$, then the discrepancies between the two methods will decrease; conversely, by scaling with an $R<R_s$, then the discrepancies would increase towards a singularity at $R=0$.

3.6. Influence of Collapse Volume

The critical collapse pressure and collapse volume are the two key parameters when estimating the damage potential of an implodable as shown by equation (3). However, equation (3) overestimates this damage potential since collapse pressure drops significantly during the implosion process. Surrounding pressures drop to extremely low values, especially at the buckle front as the implodable collapses longitudinally and reaches high velocities. Additionally, collapse pressure and velocities are proportional to one another; hence, at higher collapse pressures the quicker and further the surrounding pressures will fall. Assuming that for a general implosion cases, the surface pressures momentarily plateaus at near-cavitation levels

early during the implosion; then the collapse volume is the dominant parameter for estimating the damage potential of an implosion.

To better study the on-going collapse volume theory, and further demonstrate the Volumetric Flow Method as a useful research tool, three additional experimental cases of implosion from previous work [10] are introduced in Table 1.4 alongside to the NC case. These cases collapse in free-field implosion, have no polyurea coatings, have different geometric parameters, and are made from AL 6061-T6. Only the cases in Table 1.4 will be used and referred to for the remainder of the results and discussion section.

Table 1.4 Implosion of non-coated aluminum tubes

D **(mm)**	***L*** **(mm)**	***h*** **(mm)**	P_{cr} **(MPa)**	**Inner Volume (cc)**	**Collapse Volume (cc)**	**PE (J)**	**E (J)**
63.5	381.0	1.245	1.68	1114	829	1393	320
38.1	203.2	0.889	2.71	211	151	409	89
38.1	304.8	0.889	2.04	316	256	522	140
38.1	406.4	0.889	1.81	422	362	655	160

The actual collapse volume can be calculated using DIC and the Volumetric Flow Method at $t = t_{final}$, or measured during postmortems by water displacement (however, the latter cannot be done for every material). For cylindrical shells with rigid ends, there will always be residual volume at near these ends if there is no rupture at the boundaries. The relative collapse volume is inversely proportional to the L/D ratio, and it converges to 1 as $L/D \rightarrow \infty$. For, this reason and for mode II collapse, the general trend shown in equation (4) was assumed. The *z* value in equation (4), which is related to the material's flexibility, was solved to be 1.6 by optimizing for the coefficient of determination. This relationship is illustrated by Figure 1.9 (a) in terms

of %. Note that this *z* parameter is expected to decrease for more flexible materials and vice versa.

$$\frac{V_c}{V_i} = 1 - z\left(\frac{L}{D}\right)^{-1} \tag{4}$$

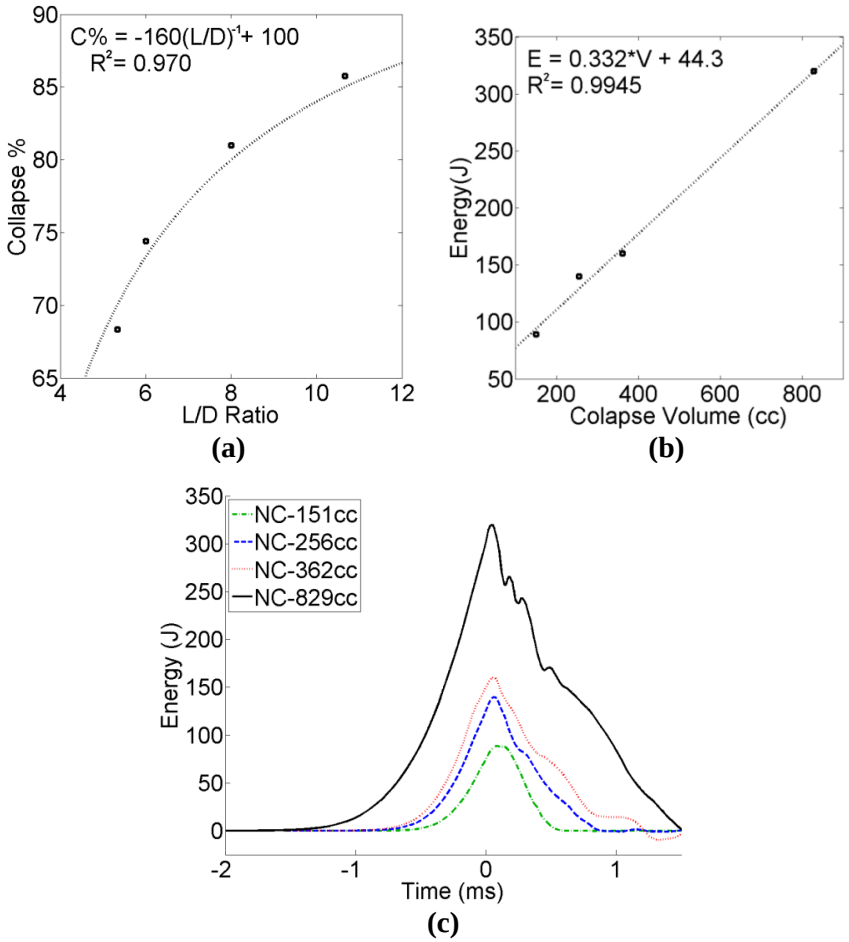

Figure 1.9 (a) Collapse volume per inner volume as a function of the L/D ratio; (b) energy as a function of collapse volume; and (c) energy as a function of time for different tubular geometries

The energy of all four non-coated cases is plotted in Figure 1.9 (c) and labeled by their respective collapse volumes. As mentioned earlier, the collapse volume plays a dominant part in determining the energy released during the implosion. This fact is illustrated by Figure 1.9 (c), where the energy emitted is proportional to collapse volume and not collapse pressure. Moreover, if the released energy is assumed to be

solely a function of collapse volume, then a highly linear trend can be found as shown in Figure 1.9 (b).

4. Conclusions

This study aimed to develop an experimental scheme to determine the localized energy history emitted during the implosion of aluminum structures. Moreover, a numerical method was established to combine the three spatial domains from the implosion DIC analysis into a volumetric measure. The new energy scheme created was used to analyze the mitigation effects of polyurea coated aluminum structures. The completion of this work resulted in the following conclusions (see Table 1.3 and Table 1.4 as reference when needed):

- Coating aluminum structures with polyurea does not notably affect their collapse pressure.
- Pressure pulses released from coated aluminum structures have mitigated effects, in turn, diminishing the impulse emitted.
- Interior coated structures have a higher mitigating effect than exterior coated structures due to the stiffening of the polyurea at high strain rates and structural contact during the longitudinal buckle propagation and interference with the hinging process.
- Normalized impulse data from sensors at various locations can be used to deduce the shape of the pressure wave.
- Volume and volumetric rate of change can be obtained for a structure by using the DIC information in a numerical scheme, as long as symmetry conditions can be

used, to compensate for the missing information in the DIC data. This is not limited to implosion events, and would work for many types of symmetrical structural deformations.

- The volumetric flow rate for aluminum structures has little change when exterior polyurea coating is applied. In contrast, interior coated structures have a lower volumetric flow due to the constant structural contact during buckle propagation and the lower velocities seen in Table 1.2.
- Through the combination of two different experimental measuring techniques (sensors and DIC) energy as a function of time can be obtained for an implosion phenomenon. Neither technique alone can obtain the entire energy history without making many assumptions.
- The energy emitted during the implosion of coated aluminum structures follows a similar trend than the impulse emitted. Exterior and interior coated structures emit less energy than the uncoated structure, with the interior coated releasing the least energy.
- The Flow Energy Method and the Volumetric Flow Method agree with each other when measuring the peak energy emitted during an implosion event within; they are apart by ~4% of the total potential energy available at an 116.45 mm distance from the center of the structure.
- Doubling the coating volume does not significantly improve the mitigation effects of the polyurea for both interior and exterior coatings.
- Collapse volume has an inversely proportional relationship with the L/D ratio for a cylindrical shell implodable.

- Collapse volume has a direct relationship with the energy released during the implosion and is a dominant factor in determining the energy release. An energy release estimate model could be created as a function of collapse volume for a given collapse pressure for cases similar to the ones reproduced in this study.

Acknowledgements

The authors kindly acknowledge the financial support provided by Dr. Thomas Fu under the Office of Naval Research (ONR) Grant No. N00014-15-1-2046.

References

[1] Turner, S. (2007). Underwater implosion of glass spheres. The Journal of the Acoustical Society of America, 121(2), 844-52.

[2] Turner, S., & Ambrico, J. (2012). Underwater Implosion of Cylindrical Metal Tubes. Journal of Applied Mechanics, 80(1), 1-11.

[3] Urick, R. (1963). Implosions as Sources of Underwater Sound. The Journal of the Acoustical Society of America, 35.

[4] Vath, F. (1968). Development of buoyancy material for the deep submergence search vehicle. Evaluation of sympathetic implosion of buoyancy modules. Defense Technical Information Center. Naval Applied Science Laboratory, Brooklyn, New York

[5] Orr, M., & Schoenberg, M. (1976). Acoustic signatures from deep water implosions of spherical cavities. The Journal of the Acoustical Society of America, 59(5), 1155-1159.

[6] Accident Grounds Neutrino Lab. (2001). Retrieved August 31, 2015, from http://physicsworld.com/cws/article/news/2001/nov/15/accident-grounds-neutrino-lab

[7] Robotic Deep-sea Vehicle Lost on Dive to 6-Mile Depth. (2014). Retrieved August 31, 2015, from http://www.whoi.edu/news-release/Nereus-Lost

[8] Farhat, C., Wang, K., Main, A., Kyriakides, S., Lee, L., Ravi-Chandar, K., & Belytschko, T. (2013). Dynamic implosion of underwater cylindrical shells: Experiments and Computations. International Journal of Solids and Structures, 50(19), 2943-2961.

[9] Ikeda, C., Wilkerling, J., & Duncan, J. (2013). The implosion of cylindrical shell structures in a high-pressure water environment. Proceedings of the Royal Society A: Mathematical, Physical and Engineering Sciences, 469(2160), 20130443-20130443.

[10] Gupta, S., Parameswaran, V., Sutton, M., & Shukla, A. (2014). Study of dynamic underwater implosion mechanics using digital image correlation. Proceedings of the Royal Society A: Mathematical, Physical and Engineering Sciences, 470(2172), 20140576-20140576.

[11] Pinto, M., Gupta, S., & Shukla, A. (2014). Study of implosion of carbon/epoxy composite hollow cylinders using 3-D Digital Image Correlation. Composite Structures, 119, 272-286.

[12] Pinto, M., Gupta, S., & Shukla, A. (2015). Hydrostatic Implosion of GFRP Composite Tubes Studied by Digital Image Correlation. Journal of Pressure Vessel Technology, 137(5), 051302-051302.

[13] Gish, L., & Wierzbicki, T. (2015). Estimation of the underwater implosion pulse from cylindrical metal shells. International Journal of Impact Engineering, 77, 166-175. doi:10.1016/j.ijimpeng.2014.11.018

[14] Tekalur, S., Shukla, A., & Shivakumar, K. (2008). Blast resistance of polyurea based layered composite materials. Composite Structures, 84(3), 271-281.

[15] Bahei-El-Din, Y., Dvorak, G., & Fredricksen, O. (2006). A blast-tolerant sandwich plate design with a polyurea interlayer. International Journal of Solids and Structures, 43(25-26), 7644-7658.

[16] Gardner, N., Wang, E., Kumar, P., & Shukla, A. (2012). Blast Mitigation in a Sandwich Composite Using Graded Core and Polyurea Interlayer. Experimental Mechanics, 52(2), 119-133.

[17] Bonsmann, J., Fourney, W. (2015). Mitigation of Accelerations Caused by Blast Loading Utilizing Polymeric-Coated Metallic Thin-Walled Cylinders. Journal of Dynamic Behavior of Materials, 259-274. doi:10.1007/s40870-015-0023-5

[18] Pinto, M., Matos, H., Gupta, S., & Shukla, A. (Accepted 2016). Comparison of Implosion Phenomenon in Thin-walled Composite and Metallic Structures. Journal of Pressure Vessel Technology. doi:10.1115/1.4032703

[19] Lurton, X. (2010). Underwater acoustic Wave Propagation. In An introduction to underwater acoustics: Principles and applications (2nd ed., pp. 22-23). Heidelberg: Springer Verlag, published in association with Praxis Publishing.

[20] Cole, R. (1948). Underwater Explosions. Princeton: Princeton Univ. Press.

CHAPTER 2. Underwater Dynamic Implosion of Marine-Grade Metallic Shells in Extreme Hydrostatic Pressures

by

Helio Matos and Arun Shukla

Dynamic Photo Mechanics Laboratory, Department of Mechanical, Industrial and Systems Engineering, University of Rhode Island, Kingston, RI 02881

In preparation for publication

Abstract

An experimental study was conducted to investigate the dynamic response of metallic grade implodables subjected to high hydrostatic pressures. Specifically, underwater implosions of AL 7075 and SS316 cylindrical shells during mode 2 and mode 3 collapses were investigated. The implodable specimens are sealed from the water with end caps and suspended inside a large pressure vessel that simulates a free-field marine environment. The hydrostatic pressure inside the pressure vessel was gradually increased until the specimens became unstable and collapsed. The collapse velocities and localized pressures of the imploding metallic structures were captured during the experiments. Two high-speed cameras recorded the imploding structures while dynamic pressure transducers measured the emitted pressure pulses. The results of these experiments indicate that the emitted pressure signals are mainly dictated by the collapse pressure alone. However, the collapse mechanics itself is strongly influenced by the mechanical properties. Moreover, additional compressive tests were performed in order to develop a new method for better estimating the potential energy of an implodable structure.

1. Introduction

An experimental study is conducted to evaluate the implosion pressure pulses and surface velocities of marine grade metallic shells under high hydrostatic pressures. This research arises from the concern of damage to naval and marine structures such as underwater pipelines, submarines, and autonomous underwater vehicles (AUVs). When these structures are submerged deep underwater and experience high

hydrostatic pressures, they can instantaneously collapse inward and release strong propagating shock waves in the process known as implosion [1-5].

The implosion phenomenon has been of importance to the marine community since the mid-1900s [3-5]. However, one key accident renewed the interest in this topic. This was the 2001 Super-Kamiokande laboratory accident in Japan where one photomultiplier tube imploded, and the pressure pulses from this implosion caused adjacent tubes to implode. The implosion of one single tube caused a chain reaction that destroyed 7000 photomultiplier tubes [6]. More recently in 2010, an AUV known as ABE was lost off the coast of Chile due to the buoyancy control glass sphere imploding [7]. Also, in 2014 the multi-million dollar AUV, Nereus, imploded off the coast of New Zealand [8]. These recent events highlight that implosion is still an ongoing issue.

Early work on implosion characterized the acoustic pulses emitted during the collapse of glass structures as well as their potential to damage nearby structures [1, 3]. This led to the creation of robust computational models (for fluid-structure interaction during implosion) for the implosion of metallic structures [2]. Later work analyzed the implosion of aluminum structures with varying lengths to produce higher modes of failure (modes 3 and 4) [9]. Furthermore, an experimental study on brass structures was made with varying geometries to examine the effect of collapse modes on the emitted pressure pulses [10]. Studies were also conducted to estimate the structural energy absorption during implosion [11-13]. Recently, the pressure pulses from imploding structures were linked to full deformation and velocity fields that were captured through a Digital Image Correlation (DIC) technique coupled with high-

speed photography [12-17]. None of the studies mentioned characterize the implosion process for marine grade materials, such as AL7075 and SS316, even though these types of materials is typically used in marine applications.

This study aims to understand the fundamental collapse mechanics and failure characteristics of marine grade materials. Specifically, underwater implosions of AL 7075 and SS316 cylindrical shells during mode 2 and mode 3 collapses will be investigated. Also, the failure mechanisms evolution of AL 7075 will be studied by varying collapse pressures. Lastly, a new technique for evaluating the potential energy of a collapse will be demonstrated.

2. Experimental Details

2.1. Facility and Specimen Geometry

The experimental facility consists of a 2.1 m semi-spherical pressure vessel and two high-speed cameras. The specimens are sealed from both ends with aluminum end-caps to prevent water penetration. Therefore, during the experiments, high-pressure water surrounds the specimen while low-pressure air resides inside. As shown in Figure 2.1, the specimen is then suspended at the center of the tank, and the tank is filled with water and pressurized with compressed nitrogen gas which is introduced from the top of the tank. This simulates increasing water depths in a marine environment. For the experiments performed in this study, the specimens were subjected to pressures ranging from 1.37 to 5.50 MPa (equivalent to 133 to 532 m below sea level respectively).

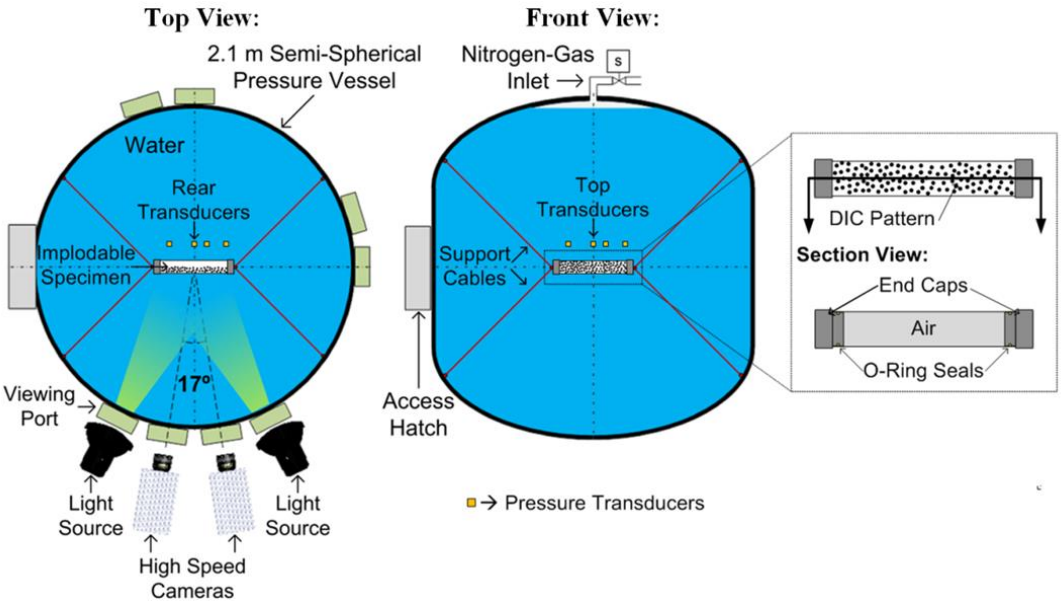

Figure 2.1 Detailed schematic of the implosion experimental facility

The high-speed cameras (Photron SA1 from Photron USA, Inc.) record the entire implosion event. The stereo images captured are then used to perform the DIC analysis (with the black and white DIC pattern shown in Figure 2.1) and obtain the full displacement and velocity fields. Previous work shows the DIC analysis error to be below 2.5% (in terms of 3D displacements and velocities) [14]. Moreover, during the implosion, 8 pressure transducers (PCB 138A05 from PCB Group, Inc.) capture localized pressure histories at 2 MHz (through a Dash 8HF-HS from Astro-Med, Inc.). These sensors are located above and behind the specimen as shown in Figure 2.2 (a). The geometrical parameters illustrated in Figure 2.2 are length, L, outer diameter, D, and wall thickness, h. Additionally, specimens can collapse in different modes depending on their geometry as illustrated in Figure 2.2 .

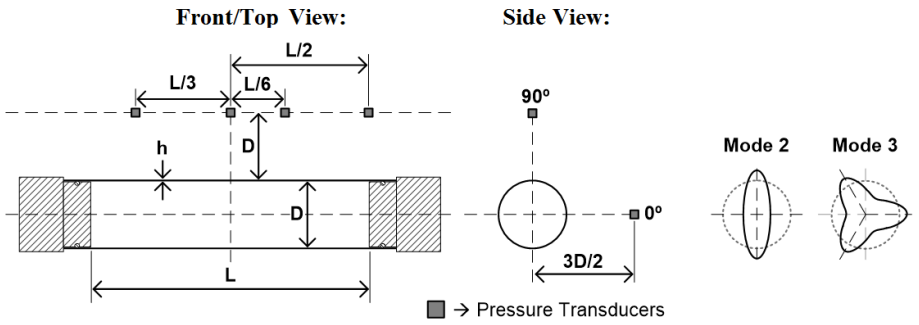

Figure 2.2 Sensor locations and side view of the 2nd & 3rd collapse modes

The specimens are made out of Al 7075-T6 and SS 316 piping. The availability of these metals is extremely limited at geometries adequate for implosion experiments. Therefore, piping with relatively thicker walls had their outer diameters machined down to satisfactory thickness. Thicknesses were determined based on the Von Mises stability equation (1) [18]; where Collapse Pressure, P_c, is a function of elastic modulus, E, poisons ration, υ, nominal radius, r, and mode number, m.

$$P_c = \frac{Eh}{r\left(m^2+\frac{1}{2}\left(\frac{\pi r}{L}\right)^2-1\right)}\left(\frac{1}{\left(\left(\frac{Lm}{\pi r}\right)^2+1\right)^2}+\frac{h^2\left(m^2+\left(\frac{\pi r}{L}\right)^2-1\right)^2}{12r^2(1-\upsilon^2)}\right) \quad (1)$$

Cylinders with large L/D ratio (>6) collapses in a mode 2 shape, while lower ratios will tend to collapse in higher modes [10]. The collapse pressure in equation (1) will be lowest at the dominant collapse mode. Thus, by adjusting the length of the specimen, the collapse mode can be predetermined. Similarly, by adjusting wall thickness, the collapse pressure can be predetermined.

Overall there are seven cases analyzed in this study, which is listed in Table 2.1. The first four cases (AL1-AL4) are performed to analyze the failure mechanism evolution. For this, a similar geometry is used with increasing collapse pressure. The last four cases (AL4, AL5, SS1, and SS2) are performed to examine the collapse

mechanics of different materials and collapse modes. Three experiments were conducted for each case to ensure consistency accuracy in the results.

Table 2.1 Experimental series details

Case	Material	*m*	L (mm)	ID (mm)	h (mm)	P_c (MPa)
AL1	AL 7075-T6	2	355.6	45.97	0.889	1.35 +/- 0.05
AL2					1.105	2.42 +/- 0.08
AL3					1.245	3.41 +/- 0.12
AL4					1.511	5.36 +/- 0.21
AL5		3	152.4		1.067	5.42 +/- 0.15
SS1	SS 316	2	355.6	47.49	1.105	4.44 +/- 0.14
SS2		3	152.4		0.775	4.35 +/- 0.23

3. Results and Discussion

3.1. Compressive Strength

The compressive loading characteristics for AL 6061-T6 (reference material), AL 7075-T6, and SS 316 were obtained for quasistatic and dynamic loading conditions in accordance to ASTM Standard D2412 [19]. The quasistatic and dynamic tests were performed with an Instron 5585 and an Instron 9210 drop weight tower (done with an 8 kg weight and a 5 m/s impact velocity) respectively. A schematic for tests performed is shown in Figure 2.3 (a). The typical result from ASTM Standard D2412 is pipe stiffness; however, the work per unit volume was obtained instead using Eq. (2) to account for the geometrical discrepancies of each material.

$$W_V = \frac{F(\Delta Y)}{V} \tag{2}$$

Where F is force, ΔY is tube compression, and V is the material volume to the tube.

In Figure 2.3 (b), work per unit volume is plotted versus the normalized displacement (with respects to the inner diameter, ID). Work per unit volume is

analogous to total strain energy, and a steeper slope in Figure 2.3 (b) is indicative that more energy is required to collapse the tube (meaning higher stiffness and collapse pressures for the same tube geometry). The quasistatic experiments yield in an initially linear work per unit volume up to ΔY/ID = 0.5, then the relationship grows exponentially as the tube fully closes (the stiffness from the fixed boundary transmits through the closed tube). For the dynamic experiments, the same linear trend and values were observed; however, the drop weight rebounds once the tube collapses to ΔY/ID = 0.7 (hence, no exponential growth). Also, the AL 7075 tubular material fractured quasistatically at to ΔY/ID = 0.8 and dynamically at ΔY/ID = 0.6. The compressive trends for these three metals are nearly strain rate independent, but strain failure of AL 7075 is strain rate dependent.

The average linear slope for each material can be obtained from Figure 2.3 (b) as: 5.57 MJ/m^3 for AL 6061-T6; 5.74 MJ/m^3 for AL 7075-T6; and 10.48 MJ/$m^3$for SS 316. Assuming that the work required to collapse the tubes by parallel-plate loading is the same as hydrostatic loading, the work potential (or potential energy) can be estimated for each implosion case as shown in Figure 2.3 (c) (neglecting the changes in collapse shape near the end caps). Total potential energy available for each case would be when ΔY/ID = 1. The usual method for estimating potential energy is by multiplying collapse pressure to cylindrical volume [12-13]; however, since collapse pressure drastically drops throughout the implosion process, using a constant pressure leads to unrealistically high estimated values for potential energy.

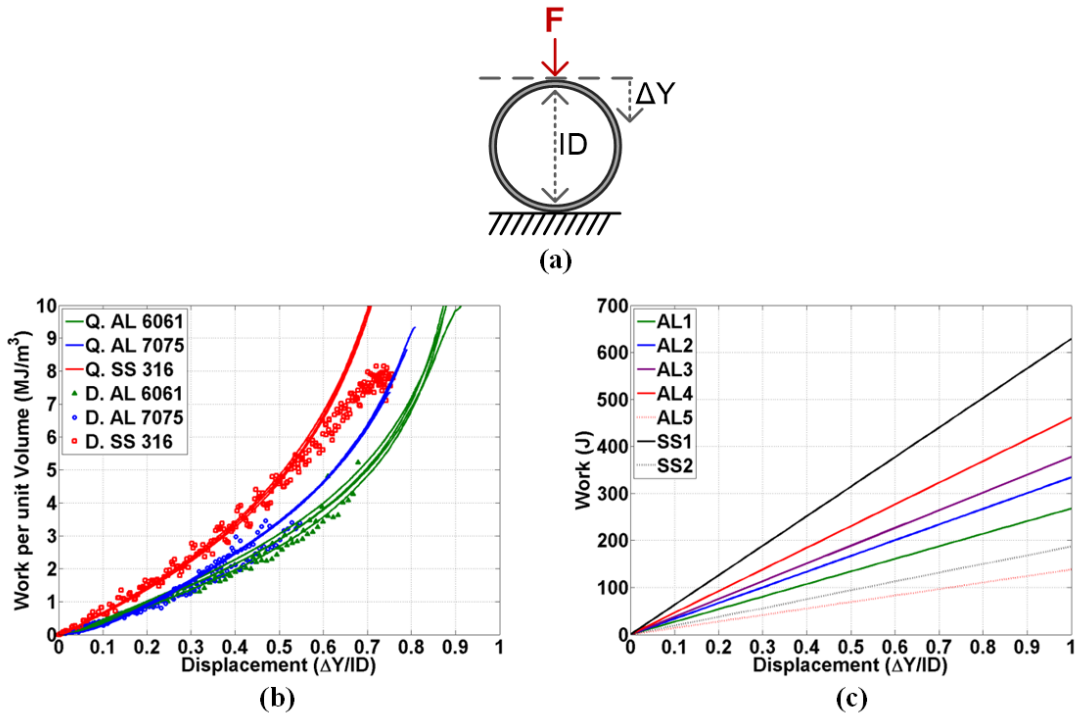

Figure 2.3 (a) Parallel-plate loading fixture schematic and (b) compressive characteristics for different tubular materials and (c) work potential for the collapse of each tube case

3.2. Collapse Damage

The post-mortem image of one representative implosion experiment for each case is given in Figure 2.4. The front and top view of the specimen are provided for the mode 2 collapses, and the front view is provided for the mode 3 collapses. Figure 2.4 (a) illustrates the damage evolution as collapse pressure increases for the mode 2 aluminum cases. All aluminum tubes have longitudinal fracture along both lobes of the collapse tubes and fractures at the end cap boundaries. As collapse pressure increases, the severity of the damage also increases. AL2 has greater fractures longitudinally and at its boundaries than AL1. If the collapse pressure is sufficiently high, the growth in collapse velocity in combination if the geometric restrictions near the end caps lead to radial branching of the longitudinal fractures as seen for the AL3

and AL4 cases. Furthermore, AL4 had more fractures in its valley due to its extremely high collapse pressure, in turn, buckle velocities. The stainless steel mode 2 implosion (Figure 2.4 (b)) does not contain any visible fracture. Lastly, for mode 3 collapses, the aluminum tube sustained fractures at its lobes, valleys, and end cap locations while the stainless steel did not endure any fracture as shown in Figures 2.4 (c) and (d) respectively.

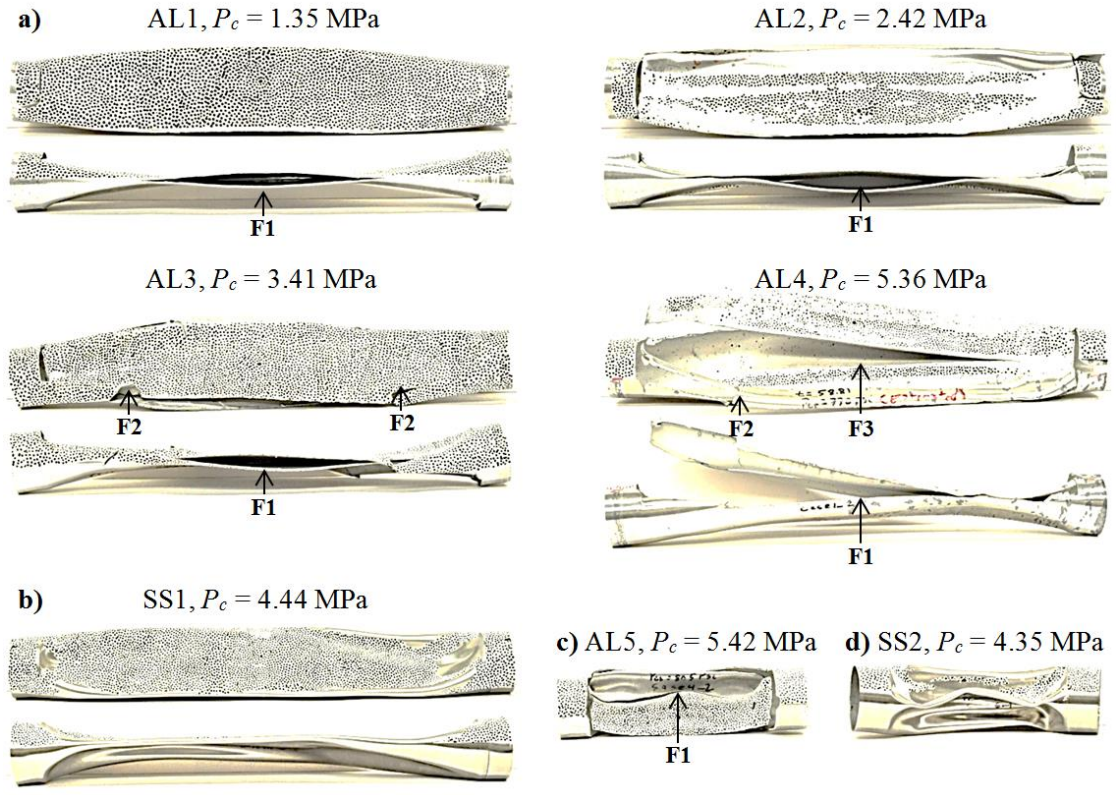

F1- Longitudinal ductile tearing along the lobes
F2- Radial ductile tearing along off of the lobes
F3- Longitudinal ductile tearing along the valley

Figure 2.4 Post-mortem images for the (a) mode 2 aluminum cases, (b) mode 2 stainless steel case, (c) mode 3 aluminum case, and (d) mode 3 stainless steel case

3.3. Pressure and Velocity Histories

The dynamic pressure histories for the aluminum cases collapsing at mode 2 and mode 3 are shown in Figures 2.5 (a) and (b) respectively. The vertical axis on Figures

2.5 (a) and (b) shows the emitted pressure waves after it is normalized by its respective collapse pressure (P/P_c= 1 represents the collapse pressure; see Table 2.1 for collapse pressure values). The horizontal axis shows time (t = 0 represents structural wall contact between opposing inner surfaces of the cylindrical tube). A representative experiment is shown in these plots and not the average from three experiments.

As collapse pressure increases, there is a decrease in collapse duration as illustrated in Figure 2.5 (a). The normalized minimum pressures are the same for the implosion cases that sustained similar damage. Moreover, the normalize maximum pressures are similar regardless of sustained damage as shown in Figure 2.5 (a). The constant maximum normalized pressure for the mode 2 aluminum cases signifies that the maximum pressure is linearly proportional to collapse pressure. Additionally, normalized pressure histories for similar aluminum and stainless steel cases (modes 2 and 3) are shown in Figure 2.5 (b). The similar aluminum and stainless steel cases also have similar pressure with one minor discrepancy. The collapse behavior of stainless steel is smoother due to its absence of fracture during the collapse.

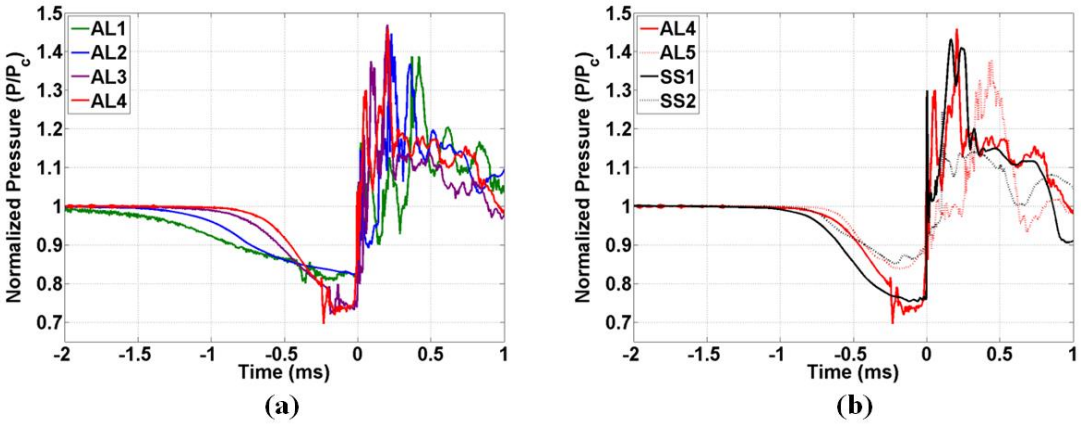

Figure 2.5 Pressure history for the (a) aluminum cases collapsing at mode 2 at different collapse pressure and (b) aluminum and stainless steel cases collapsing at mode 2 and 3 at similar collapse pressures

The center point velocity for all implosion cases that was obtained from the DIC technique are shown in Figure 2.6 (a). All mode 2 collapse structures have a gradual increase in velocity until a drastic drop in velocity happens when there is structural wall contact between opposing inner surfaces at t = 0. For mode 3 collapse, the opposing inner surfaces (or valleys) are 120 degrees apart, and the contact between these three surfaces is not as abrupt as mode 2 contact, hence the smoother drop in pressure. The collapse velocities between the aluminum and stainless steel cases in Figure 2.6 (a) are driven predominately by the collapse pressure and not material property. The peak velocities from each mode 2 aluminum collapse experiment are plotted in Figure 2.6 (b). The repeatability of the implosion experiments, as well as the velocities linear relationship to collapse pressure (with the same tube geometry), is illustrated in Figure 2.6 (b). The linear increase in velocity means a linear increase in kinetic energy. Moreover, the linear increase in kinetic energy is responsible for the steady growth in damage seen in Figure 2.4 (a) and is indicative of an increase in emitted energy.

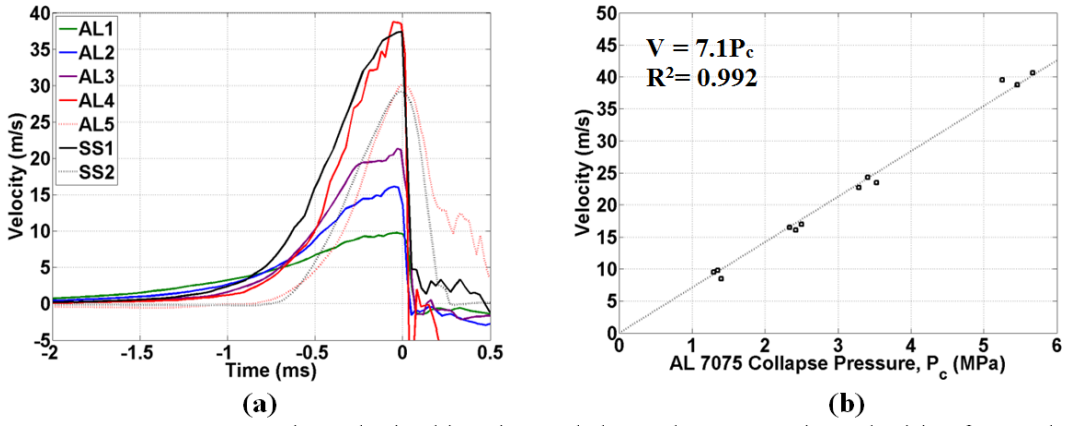

Figure 2.6 (a) Center point velocity histories and (b) peak center point velocities for mode-2 aluminum collapses vs. collapse pressure

3.4. Emitted Energy

The energy emitted/released during implosion can be obtained from the measured pressure, p, history [12-13]. The energy flux, E_F, from a collapsing volume is calculated from the integral of pressure squares times the inverse of the fluid density, ρ_0, and two times the sensor's standoff distance, R_c, as shown in Eq. (3). The flux in Eq. (3) represents the energy released during the under-pressure region of the pressure history ($t < 0$), which is also the energy stored in the implodable (in the form of compressed air) during collapse [20, 21]. The stored energy is released during the over-pressure region of the pressure history ($t > 0$) similarly to a gas bubble collapse; in other words, the impulse from $t < 0$ is equal and opposite to the impulse from $t > 0$ [1-2]. Furthermore, Eq. (3) can be simplified as Eq. (4), where the integral of pressure is the implosion's impulse, I. Lastly, since the pressure emitted from an implodable is a spherical pulse [1-2,13] , then the surface area of a sphere of radius R_c can be used to calculate total emitted energy, E_T, as shown in Eq. (5).

$$E_F = \frac{1}{2\rho_0 R_c}\left[\int_0^t p dt\right]^2 \quad (3)$$

$$E_F = \frac{I^2}{2\rho_0 R_c} \quad (4)$$

$$E_T = E_F[4\pi R_s^2] \quad (5)$$

The total energy emitted for each implosion case is shown in Figure 2.7 (a) as a function of time. The initial increase in energy in Figure 2.7 (a) represents energy being stored in the compressible gas inside the implodable (in the form of low-pressure pulses). Once the tube fully collapses, it starts to release the stored energy into the fluid (in the form of high-pressure pulses) until the stored energy goes back to zero. The peak energy represents the maximum stored energy as well as the total energy released.

As collapse pressure increases, it is expected that the emitted energy also increases. Therefore, to evaluate tubes of different collapse pressures, the total emitted energy needs to be normalized with respect to potential energy during the collapse. In previous studies, the maximum potential energy is estimated by multiplying collapse pressure to cylindrical volume [12-13]. The normalization of the total emitted energy with respect to this maximum potential energy (P_cV) is illustrated in Figure 2.7 (b). Since the driving pressure drastically drops during the implosion process, using a constant pressure leads to an unrealistically high estimation for the maximum potential energy. The new method for estimating potential energy is also used to calculate a normalized emitted energy as shown in Figure 2.7 (c).

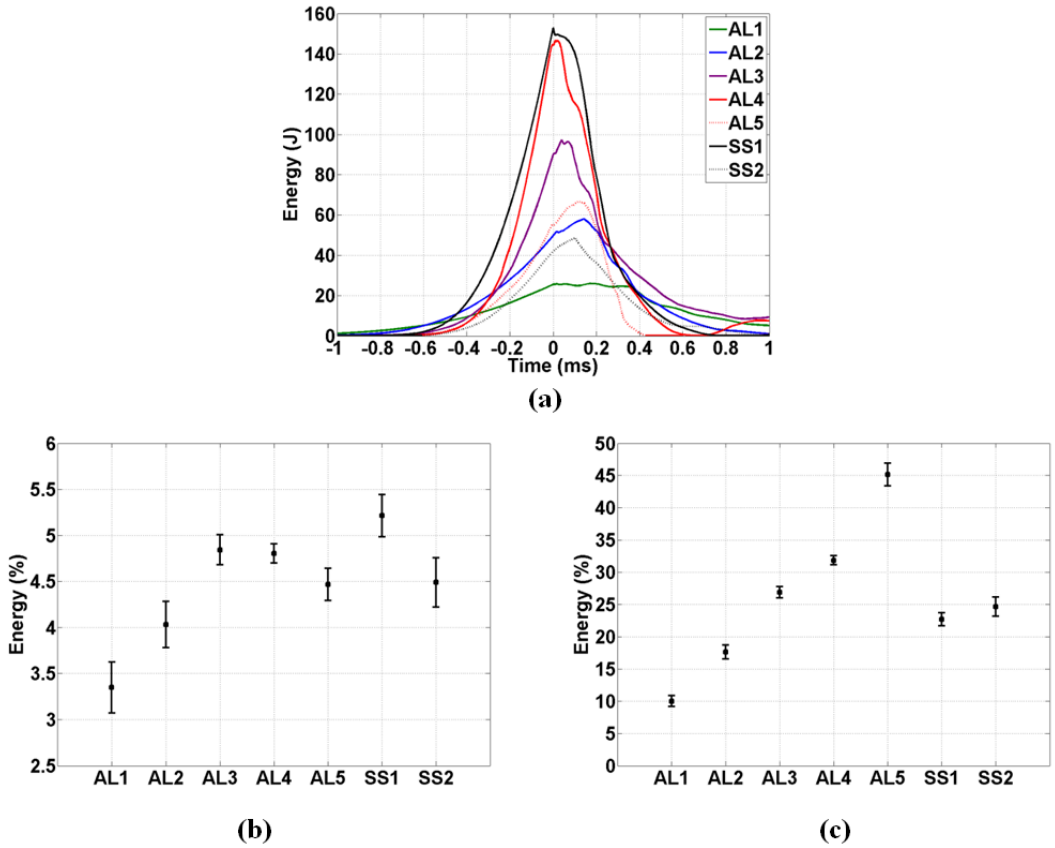

Figure 2.7 (a) Emitted flow energy history, (b) peak normalized emitted flow normalized with respect to maximum potential energy (PcV), and (c) peak normalized emitted flow normalized with respect to collapse potential energy

The maximum potential energy (P_cV) normalization (Figure 2.7 (b)) implies that 95% to 97 % of the implosion energy is transferred in the form of heat, vibrations, and sounds. However, the collapse energy normalization (Figure 2.7 (c)) implies that 55%-90% of the implosion energy is transferred to forms of energy other than pressure; which is more reasonable than the latter. Also, the AL1 to AL4 implosion cases shows a similarly emitted energy trend in Figure 2.7 (c) as the increase in kinetic energy trend and growth in collapse damage.

For the Mode 3 collapses, the estimated potential energy from based on the parallel plate technique is low. Since the collapsed tube has three lobes and valleys instead of two, its total strain energy is nearly 3/2 of a mode 2 collapse. Hence, more

energy from the implosion is used in damaging the specimen so relatively less energy should be transmitted into the fluid in the form of pressure. Table 2.2 summarizes the experimental results and adjusts the collapse potential energy for the Mode 3 collapse (from Figure 2.3 (c) when ΔY/ID = 1) by a 3/2 factor. An alternative to applying this adjustment factor would be to perform compressive tests using a 3 point compressive fixture with contacts set 120 degrees apart. Table 2.2 shows that mode 3 collapses will release relatively less energy than a mode 2 collapse.

Table 2.2 Experimental results summary

Case	Material	m	P_c (MPa)	Maximum Emitted Energy, E_{max} (Pa)	Collapse Potential Energy (Pa)	Normalized Emitted Energy (%) [a]
AL1	AL 7075-T6	2	1.35 +/- 0.05	26.70 +/- 2.24	267.6	9.99
AL2			2.42 +/- 0.08	58.88 +/- 3.66	334.1	17.62
AL3			3.41 +/- 0.12	101.50 +/- 3.03	337.6	26.88
AL4			5.36 +/- 0.21	146.86 +/- 3.17	460.9	31.86
AL5		3	5.42 +/- 0.15	62.41 +/- 2.42	207.3 [b]	30.11
SS1	SS 316	2	4.44 +/- 0.14	142.67 +/- 6.32	668.7	22.69
SS2		3	4.35 +/- 0.23	46.30 +/- 2.77	281.6 [b]	16.45

a. Based on the collapse potential method
b. Adjusted by a 3/2 factor

4. Conclusions

An experimental investigation is conducted to understand the fundamental collapse mechanics and failure characteristics of marine grade materials. Specifically, underwater implosions of AL 7075 and SS316 cylindrical shells during mode 2 and mode 3 collapses were investigated. Both pressure measurements along with high-speed DIC measurements are carried out to correlate the structural deformation with pressure history. The main findings of this study are as follows:

- Assuming that the work required to collapse the tubes by parallel-plate loading is the same as hydrostatic loading, the work potential (or potential energy) for implosion can be estimated from simple compression tests.

- All 7075 aluminum tubes have longitudinal fracture along both collapsed lobes and fractures at the end cap boundaries. As collapse pressure increases, the severity of the damage also increases. For the higher collapse pressures, the longitudinal fractures branched radially, and fractures along the valley were also observed.
- The normalized minimum pressures are the same for the implosion cases that sustained similar damage. Moreover, the normalize maximum pressures are similar regardless of sustained damage. The constant maximum normalized pressure for the mode 2 aluminum cases signifies that the maximum pressure is linearly proportional to collapse pressure.
- The similar aluminum and stainless steel cases have similar pressure histories (same normalized maximum and minimum values). However, the collapse behavior of stainless steel is smoother due to its absence of fracture during the collapse.
- The peak and profile of the collapse velocities between the similar aluminum and stainless steel cases in this study are driven predominately by the collapse pressure and not material property.
- The linear increase in velocity means a linear increase in kinetic energy. Moreover, the linear increase in kinetic energy is responsible for the steady growth in damage seen in Figure 2.4 (a) and is indicative of an increase in emitted energy.
- The collapse energy normalization (from Table 2.2) implies that 70%-90% of the implosion energy from the cases studied is transferred to forms of energy other than pressure. Also, the AL1 to AL4 implosion cases shows a similarly emitted

energy trend in Figure 2.7 (c) as the increase in kinetic energy trend and growth in collapse damage.

- Since the collapsed tube has three lobes and valleys instead of two, its total strain energy is nearly 3/2 of a mode 2 collapse. Hence, more energy from the implosion is used in damaging the specimen so relatively less energy should be transmitted into the fluid in the form of pressure. When estimating the potential energy from parallel plate loading, a 3/2 factor should be used to correct for available energy.

Acknowledgements

The authors kindly acknowledge the financial support provided by Dr. Thomas Fu under the Office of Naval Research (ONR) Grant No. N00014-15-1-2046.

References

[1] Turner, S. (2007). Underwater implosion of glass spheres. The Journal of the Acoustical Society of America, 121(2), 844-52.

[2] Turner, S., & Ambrico, J. (2012). Underwater Implosion of Cylindrical Metal Tubes. Journal of Applied Mechanics, 80(1), 1-11.

[3] Urick, R. (1963). Implosions as Sources of Underwater Sound. The Journal of the Acoustical Society of America, 35.

[4] Vath, F. (1968). Development of buoyancy material for the deep submergence search vehicle. Evaluation of sympathetic implosion of buoyancy modules. Defense Technical Information Center. Naval Applied Science Laboratory, Brooklyn, New York

[5] Orr, M., & Schoenberg, M. (1976). Acoustic signatures from deep water implosions of spherical cavities. The Journal of the Acoustical Society of America, 59(5), 1155-1159.

[6] Accident Grounds Neutrino Lab. (2001). Retrieved August 31, 2015, from http://physicsworld.com/cws/article/news/2001/nov/15/accident-grounds-neutrino-lab

[7] R.I.P. A.B.E. (2010). Retrieved January 13, 2016, from http://www.whoi.edu/oceanus/feature/rip-abe

[8] Robotic Deep-sea Vehicle Lost on Dive to 6-Mile Depth. (2014). Retrieved August 31, 2015, from http://www.whoi.edu/news-release/Nereus-Lost

[9] Farhat, C., Wang, K., Main, A., Kyriakides, S., Lee, L., Ravi-Chandar, K., & Belytschko, T. (2013). Dynamic implosion of underwater cylindrical shells: Experiments and Computations. International Journal of Solids and Structures, 50(19), 2943-2961.

[10] Ikeda, C., Wilkerling, J., & Duncan, J. (2013). The implosion of cylindrical shell structures in a high-pressure water environment. Proceedings of the Royal Society A: Mathematical, Physical and Engineering Sciences, 469(2160), 20130443-20130443.

[11] Gish, L., & Wierzbicki, T. (2015). Estimation of the underwater implosion pulse from cylindrical metal shells. International Journal of Impact Engineering, 77, 166-175.

[12] Pinto, M., & Shukla, A. (2015). Mitigation of pressure pulses from implosion of hollow composite cylinders. Journal of Composite Materials, 50(26), 3709-3718. doi:10.1177/0021998315624254

[13] Matos, H., & Shukla, A. (2016). Mitigation of implosion energy from aluminum structures. International Journal of Solids and Structures, 100-101, 566-574. doi:10.1016/j.ijsolstr.2016.09.030

[14] Gupta, S., Parameswaran, V., Sutton, M., & Shukla, A. (2014). Study of dynamic underwater implosion mechanics using digital image correlation. Proceedings of the Royal Society A: Mathematical, Physical and Engineering Sciences, 470(2172), 20140576-20140576.

[15] Pinto, M., Gupta, S., & Shukla, A. (2014). Study of implosion of carbon/epoxy composite hollow cylinders using 3-D Digital Image Correlation. Composite Structures, 119, 272-286.

[16] Pinto, M., Gupta, S., & Shukla, A. (2015). Hydrostatic Implosion of GFRP Composite Tubes Studied by Digital Image Correlation. Journal of Pressure Vessel Technology, 137(5), 051302-051302.

[17] Pinto, M., Matos, H., Gupta, S., & Shukla, A. (2016). Comparison of Implosion Phenomenon in Thin-walled Composite and Metallic Structures. Journal of Pressure Vessel Technology. doi:10.1115/1.4032703

[18] R. Von Mises (1929). The critical external pressure of cylindrical tubes under uniform radial and axial load, translated by D. F. Windenburg. Stodolas Festschr, 418–430

[19] ASTM Standard D2412-11. (2011). Standard Test Method for Determination of External

Loading Characteristics of Plastic Pipe by Parallel-Plate Loading. ASTM International, West Conshohocken, PA. doi: 10.1520/D2412-11

[20] Cole, R. (1948). Underwater Explosions. Princeton: Princeton Univ. Press.

[21] Arons, A. B., & Yennie, D. R. (1948). Energy Partition in Underwater Explosion Phenomena. Reviews of Modern Physics, 20(3), 519-536. doi:10.1103/revmodphys.20.519

CHAPTER 3. Pressure Signature and Evaluation of Hammer Pulses during Underwater Implosion in Confining Environments

by

Sachin Gupta[1], Helio Matos[1], James LeBlanc[2], and Arun Shukla[1]

1 Dynamic Photo Mechanics Laboratory, Department of Mechanical, Industrial and Systems Engineering, University of Rhode Island, Kingston, RI 02881

2 Naval Undersea Warfare Center (Division Newport), Newport, RI 02841

Published in The Journal of the Acoustical Society of America

Gupta, S., Matos, H., Shukla, A., & Leblanc, J. M. (2016). Pressure signature and evaluation of hammer pulses during underwater implosion in confining environments. The Journal of the Acoustical Society of America, 140(2), 1012-1022. doi:10.1121/1.4960591

Abstract

The fluid structure interaction phenomenon occurring in confined implosions are investigated using high-speed 3-D digital image correlation (DIC) experiments. Aluminum tubular specimens are placed inside a confining cylindrical structure that is partially open to a pressurized environment. These specimens are hydrostatically loaded until they naturally implode. The implosion event is viewed, and recorded, through an acrylic window on the confining structure. The velocities captured through DIC are synchronized with the pressure histories to understand the effects of confining environment on the implosion process. Experiments show that collapse of the implodable volume inside the confining tube leads to strong oscillating water hammer waves. The study also reveals that the increasing collapse pressure leads to faster implosions. Both peak and average structural velocities increase linearly with increasing collapse pressure. The effects of the confining environment are better seen in relatively lower collapse pressure implosion experiments in which a long deceleration phase is observed following the peak velocity until wall contact initiates. Additionally, the behavior of the confining environment can be viewed and understood through classical water hammer theory. A one-degree-of-freedom theoretical model was created to predict the impulse pressure history for the particular problem studied.

1. Introduction

The buckling of cylindrical shell structures has been investigated extensively because of their application in the design of underwater and aerospace structures.

These structures undergo extreme external pressures when used in underwater applications. If the external hydrostatic pressure exceeds a certain value for a given design, the structure loses its structural stability and undergoes buckling. This buckling in underwater situations is a rapid process and causes the entire structure to collapse onto itself. This event commonly referred as “implosion” is shown to be highly violent in nature with resulting high-velocity water motion, strong shock waves, and sound [1]. Several investigations have been reported by researchers in naval and marine communities on the mechanics and fluid-structure interaction during a free-field implosion process [2-13]. From the study conducted by Turner and Ambrico [8], the mechanism of implosion process for metallic structures can be described as follows: (1) the initial collapse phase, prior to wall contact, is accompanied by a smooth decrease in pressure in the surrounding water, (2) at the moment that contact is made between opposing sides of the collapsing cylinder at the center, a short duration pressure spike is emitted in the surrounding water, (3) a large positive pressure is produced at the instant that contact between the two opposing sides extends the full width of the cylinder, and (4) as the buckle propagates toward the ends, the pressure pulse continues, but at a lower magnitude, until the buckle reaches the end cap, and the collapse of the cylinder completes.

Although the mechanics of implosion is well established for free-field implosion situations, the studies reporting the implosion occurring in confining environments are very limited. The authors have recently reported the mechanics of implosion of cylindrical shells in a closed confining environment [14-16]. The result of these studies indicated that the limited hydrostatic potential energy present in water

significantly affects the implosion process in confining environments. The rate and extent of the collapse progression of the implodable volume are dramatically reduced due to the sudden decrease of potential energy inside the confining tube, and the magnitude of the hammer pressure wave is always smaller than the hydrostatic pressure. If the confining tube is open at one end, the mechanics of implosion changes drastically and it leads to generation of extremely strong water hammer waves with significant time period as shown previously by Costa and Turner [17]. Author's recent study on sympathetic implosion inside an open-ended confining tube indicates that these hammer waves can potentially damage even relatively stronger implodable volumes inside the confining tube [17]. Both of these studies measured the dynamic pressure history inside the open ended confining tube to understand the evolution of water hammer waves at the onset of implosion [17-18]. As the development of such implosion waves is a highly fluid structure interaction process, the structural deformations coupled with the surrounding fluid leads to the generation of water hammer waves. Any changes in the design of the structure will alter the fluid structure interaction process and thus the strength of hammer waves. Therefore, in a real design, the mechanics of collapse can be completely different depending upon the geometry/location of the implodable volume inside the confining tube. Thus, there is a need to understand the evolution of these waves from both structural deformation and the fluid mechanics point of view in order to predict the peak strength and total impulse of these harmful water hammer waves. To the best of author's knowledge, there have been no studies reported on relating the generation of water hammer waves with the measured structural deformations of the implodable volume. Hence, this

article addresses this research gap by investigating the underwater implosion mechanics in the open-ended confining tube using 3-D digital image correlation.

The implosion experiments are conducted with 38.1 mm outer diameter and 254 mm long implodable volumes with four different wall thicknesses such that the collapse pressure varies from 1.50 MPa to 4.24 MPa. This variation in critical collapse pressure allows identifying the changes in open-ended confining tube's implosion mechanics with increasing collapse pressure. Results of this study show that an increase in collapse pressure increases the structural velocity significantly leading to a faster implosion process. In turn, the entering water velocities are higher at the open end of the confining tube, which generates stronger water hammer waves for relatively higher collapse pressures. Contrary to a free-field implosion process in which the structural velocity is highest right before the initiation of wall contact [10], the confined open tube implosion shows that the structural velocity reaches a peak value well before the wall contact initiation. This is followed by a deceleration phase until the initiation of wall contact.

This chapter has been structured as follows. Section 2 describes the open-ended confining tube pressure vessel facility used to conduct the experiments. This section also details the 3-D DIC calibration procedure followed for quantifying the accuracy of the DIC measurements made through a curved acrylic window. Section 3 discusses the real-time deformation measurements captured using 3-D DIC along with the pressure history. The evolution of structural deformation along with the key parameters such as peak hammer pressure and peak structural velocity are discussed in this section. This section also discusses a single degree of freedom model to describe

the evolution of hammer impulse as a function of time and has been compared with experimental results. Section 4 summarizes the major findings of this study.

2. Experimental Setup

2.1. Implodable Volume and Open-ended Confining Tube

The implosion experiments are conducted inside an underwater pressure vessel facility at the University of Rhode Island. The implodable volumes chosen in this study are made out of commercially available aluminum 6061-T6 seamless extruded tubing with a nominal outer diameter of 38.1 mm (1.5 in) and an unsupported length of 254 mm (10.0 in). The wall thickness of the implodable volume is increased from 0.73 mm (0.029 in) to 1.09 mm (0.043 in) in order to achieve an observable variation in the collapse pressure. Table 3.1 provides a layout of the implosion experiments conducted in this study. The implodable volumes are sealed on both ends using solid aluminum end-caps, which utilize circumferential O-rings for sealing the specimen for underwater experiments.

Table 3.1 Layout of the experiments

Experiment Label	Unsupported Length	Outer Diameter	Wall Thickness	Experimental Collapse Pressure (P_c)
W29	254 mm (10 in)	38.1 mm (1.500 in)	0.73 mm (0.0287 in)	1.50 MPa (218 psi)
W35		38.1 mm (1.500 in)	0.89 mm (0.0349 in)	2.05 MPa (297 psi)
W38		37.5 mm (1.478 in)	0.98 mm (0.0385 in)	3.14 MPa (456 psi)
W43		37.8 mm (1.488 in)	1.10 mm (0.0432 in)	4.24 MPa (615 psi)

The implodable volumes are placed concentrically inside a confining tube with one open end which sits inside the underwater pressure vessel facility [10]. The schematic of pressure vessel facility with confining tube and implodable volume is shown in

Figure 3.1. The pressure vessel has a cylindrical section of 2.13 m (84 in) diameter and 1.07 m (42 in) length with hemispherical domes. A longitudinal section indicating the position of the confining tube along with the implodable volume is shown in Figure 3.1 (a). The total internal height of the vessel is 2.13 m (84 in). A section through the mid length of the vessel indicating the exact location of the view ports and cameras is shown in Figure 3.1 (b). The cylindrical segment of the vessel has eight circular viewports each having a 76 mm (3 in) thick clear acrylic window of diameter 102 mm (4 in) for viewing and illumination (see Figure 3.1 (b)). The pressure vessel is pressurized using compressed nitrogen gas from the top of the chamber using an inlet solenoid valve. On the onset of implosion, the volume of the specimen decreases leading to a small change in the hydrostatic pressure in the surrounding water. Expansion of nitrogen gas on the top compensates for this change and aids in simulating a constant hydrostatic pressure free-field environment inside the pressure vessel.

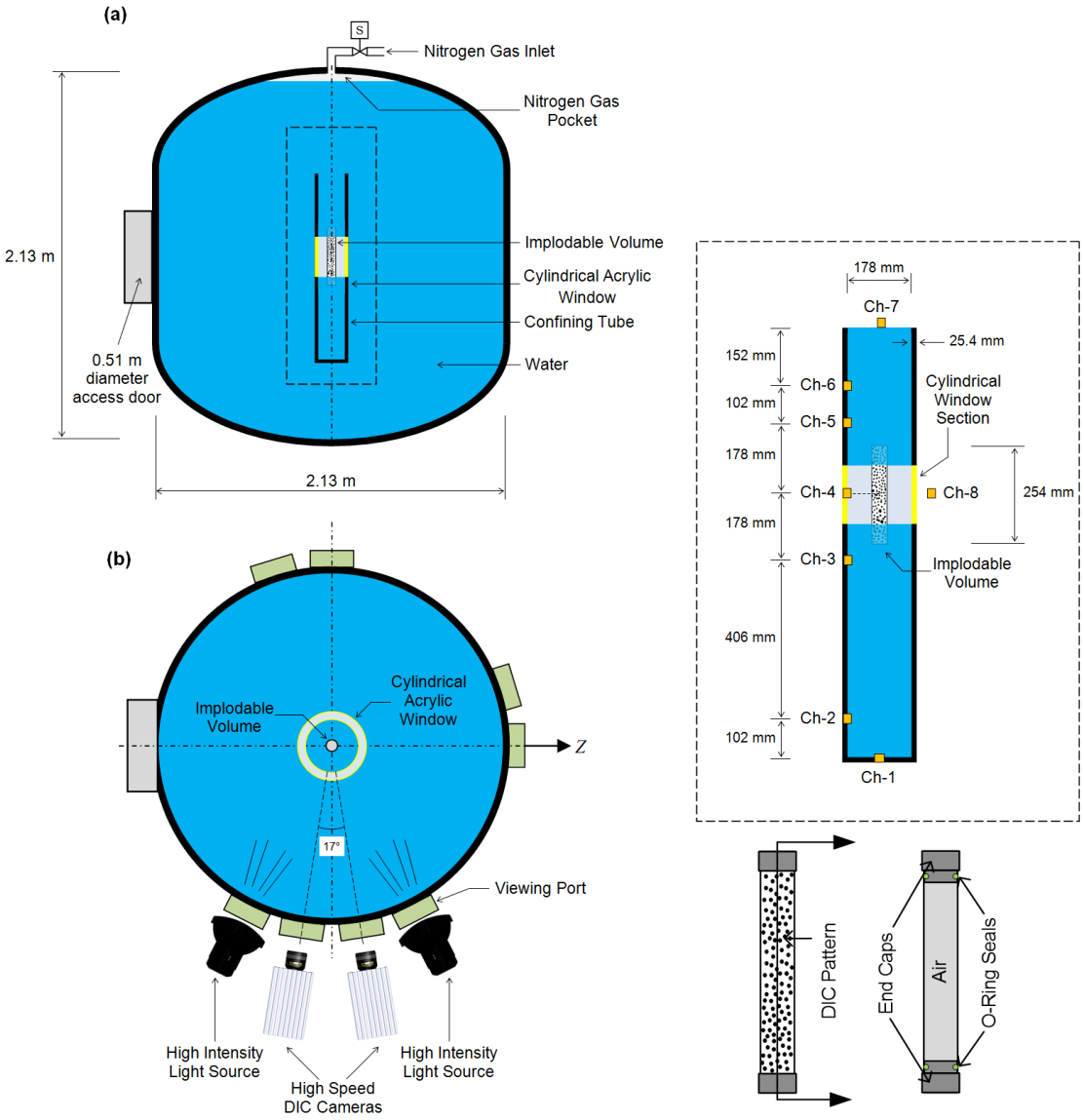

Figure 3.1 Schematic of the open-ended confining tube implosion facility. (a) Longitudinal section of the underwater pressure vessel. The confining tube is placed at the center of the pressure vessel. (b) Section through mid-length of the pressure vessel. A detailed schematic of the open-ended confining tube, as well as specimen details, are shown on the right

The schematic of the open-ended confining tube utilized in this study can also be seen in Figure 3.1. The confining tube has an inner diameter (D) of 178 mm (7.0 in) with 25.4 mm (1.0 in) wall thickness (h) and is made out of aluminum 6061-T6. The confining tube is equipped with a 152 mm long (6.0 in) cylindrical transparent acrylic window section in order to facilitate the visualization of the implodable during

implosion event. The inner diameter and the wall thickness of cylindrical window section are identical to the aluminum section to maintain constant cross-sectional area throughout the length of the confining tube. The total length (L) of the confining tube is 1.12 m (44 in). The bottom end of the confining tube is closed with an end-plate, and the top end is open to the high-pressure water environment of the pressure vessel. The implodables are placed inside the confining tube such that the distance between the bottom end-plate and the center of the implodable is 686 mm (27 in). Both high-frequency dynamic face pressure sensors (PCB-113B22) and tourmaline blast pressure sensors (PCB 138A05) are installed in the inner wall of the confining tube at various locations to capture the water hammer wave evolution during the implosion event. The signal from the pressure sensors is recorded using a 200 KHz bandwidth recorder at a sampling rate of 2 MHz.

The real time deformation of the implosion event is captured using a pair of Photron SA-1 high-speed cameras at 30,000 frames/second. A random intensity pattern is applied on the surface of the implodable volume using flat paint, and the pattern is illuminated using a pair of high-intensity arc lamps [10].

2.2. Calibration of 3-D Digital Image Correlation Technique

The authors have recently shown that calibration of extrinsic and intrinsic parameters by using a submerged calibration target can result in high accuracy for both in-plane and out-of-plane displacement measurements using 3-D DIC [10]. As the experimental setup used in this article contains an additional medium in the optical path of the cameras (i.e. cylindrical acrylic window as shown in Figure 3.1), the

technique proposed by Gupta *et al.* [10] requires recalibration in order to estimate the accuracy of measured DIC in-plane/out-of-plane displacements for objects placed inside a cylindrical window. Therefore, two sets of calibration are conducted in this study. The first is an experimental-calibration which is performed in the experimental setup (Figure 3.1) in order to obtain the relative camera parameters needed to run experiments. The second is an accuracy-calibration which is performed in a custom designed tank (shown in Figure 3.2) to re-evaluate the DIC accuracy.

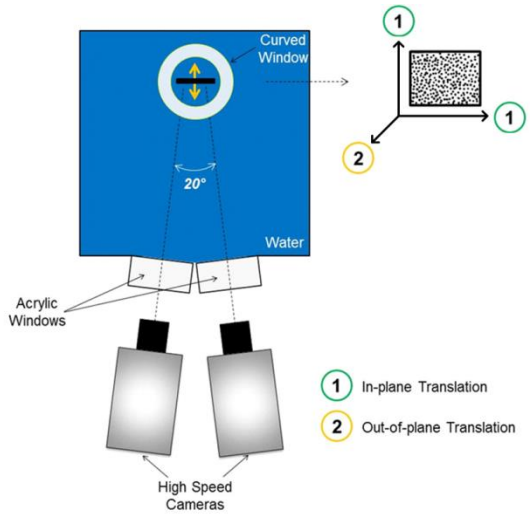

Figure 3.2 Custom designed tank setup for underwater DIC calibration experiments

The accuracy-calibration custom tank utilizes the identical cylindrical window section described in Sec. 2.1. Hence, this setup replicates the optical effect of submersion of implodable volume inside the cylindrical window section of the confining tube using a more accessible smaller tank. The setup is approximately 600 mm (24 in) long and 350 mm (14 in) wide with a height of ~150 mm (6 in). A 76 mm x 51 mm (3 in x 2 in) speckled flat aluminum specimen is placed inside the cylindrical window on a precision translation stage, which can provide translations with 0.01 mm accuracy. The aluminum specimen is placed at ~20 mm in front of the central axis of

the cylindrical window towards cameras, which represents a typical location of 38.1 mm outer diameter implodable volume inside the confining tube.

The SA-1 high-speed cameras, with the same front-end optics, are used to capture images of the translated specimen during accuracy-calibration experiments. The resolution of the camera image is 1024 × 1024 pixels, corresponding to an approximate magnification factor of 4.02 pixels/mm. Calibration of intrinsic and extrinsic parameters is performed using a submerged calibration grid (12 dots x 9 dots, 7 mm interspacing). Using the translation stage, the specimen is translated in 1 mm increments in both in-plane and out-of-plane directions (towards the window's central axis) and the corresponding images are captured. Displacement of the specimen at each translation increment is estimated with Vic-3-D 2012 software using 45 × 45 pixels subsets and a step size of 7 [19].

The out-of-plane 3-D DIC accuracy-calibration results for submerged objects are shown in Figure 3.3. Both displacements and strains (von-Mises) are calculated from the 3-D DIC measurements. To quantify the precision of the measured displacement and strains, the average surface displacement and standard deviation over the whole area for each given displacement is calculated. A plot of the true out-of-plane displacement and the measured average DIC displacement of the specimen is shown in Figure 3.3 (a). The measured average DIC displacements are in good agreement with the true displacements and the percentage error between true and measured out-of-plane displacement is less than 5%. The range of pseudo strain is calculated across the area such that 95% of the values lie in the range. The value of pseudo strains is found to be increasing with increasing out-of-plane displacement, and the maximum pseudo

strains are found up to 0.5% for 10 mm displacement (see Figure 3.3 (b)). This monotonic increase in pseudo strains is possibly due to the effect of the cylindrical acrylic window. The translation changes the effective distance between the window and aluminum target causing curvature of the window to distort the image leading to higher pseudo strain values for larger translations.

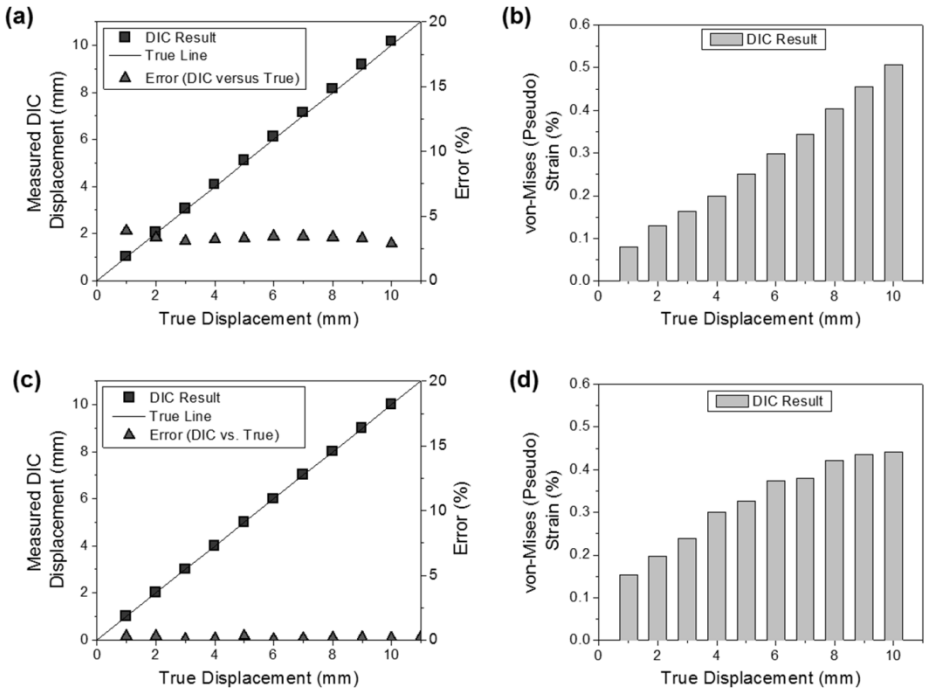

Figure 3.3 Underwater DIC calibration experiments (a) Out-of-plane displacement (b) measured von-Mises (pseudo) strain during out-of-plane translation (c) in-plane displacement (d) measured von-Mises (pseudo) strain during in-plane translation

The in-plane 3-D DIC accuracy-calibration results for submerged objects are also shown in Figure 3.3. A comparison of true in-plane displacement and measured average DIC displacement as shown in Figure 3.3 (c) indicates that the two are in good agreement. The magnitude of error is < 1% for all in-plane displacements. The range of pseudo strains is found to be up to 0.4% (see Figure 3.3 (d)). As the measurement of displacements is the primary interest in the implosion experiments, it

can be concluded that both in-plane and out-of-plane displacements can be measured with adequate precision using this accuracy-calibration DIC procedure in the case of submerged object viewed through a cylindrical acrylic window. The extraction of camera's intrinsic and extrinsic parameters using submerged calibration grid can successfully account for both flat/cylindrical acrylic viewing window and the change in refractive index due to water. Note that this method of measuring accurate displacement holds only when cameras are placed perpendicular to the curved acrylic window. Other recalibrations or modifications in procedures may be necessary to the camera setup different from described in this article.

After performing the experimental-calibration, the precision of measured DIC displacement is further estimated quantifying the radius of the implodable using 3-D DIC technique inside the experimental setup (Figure 3.1). A typical plot of local radius of the implodable volume is shown in Figure 3.4. The measurement of radius agrees very well with the true radius of the implodable volume. The radius is found to 19.07 mm ± 0.22 mm (with 95% confidence interval). As the true radius of the specimen is 19.05 mm, the maximum deviation from true radius is found to be 2.25%. Thus, it can be established that both the shape and 3-D deformation of submerged objects behind a cylindrical window can be measured accurately using the accuracy calibration process.

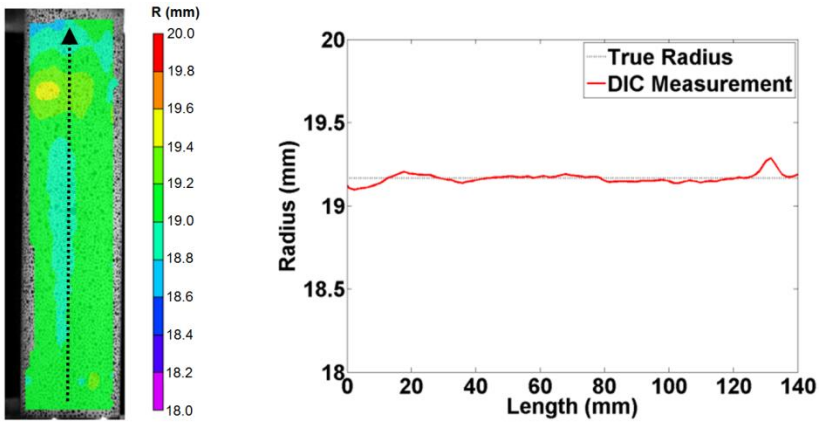

Figure 3.4 Measurement of the radius of the implodable volume using 3-D DIC

3. Results and Discussions

3.1. Full-field Structural Velocity Variation with Collapse Pressure

The experimental cases in Table 3.1 are named after their relative wall thickness; for instance, W29 represents a case with 29 thousands of an inch wall thickness. The DIC velocity contours for the lowest collapse pressure experiment, W29, and for the highest collapse pressure experiment, W43, are shown in Figure 3.5. 3-D DIC measurements are also conducted for W35 and W38, but only the min/max collapse pressure experiments are discussed in detail to understand the effect of collapse pressure on the deformation history of implodable. Time t = 0 ms indicates the time when the dynamic pressure at the nearest sensor drops to 99% of the collapse pressure.

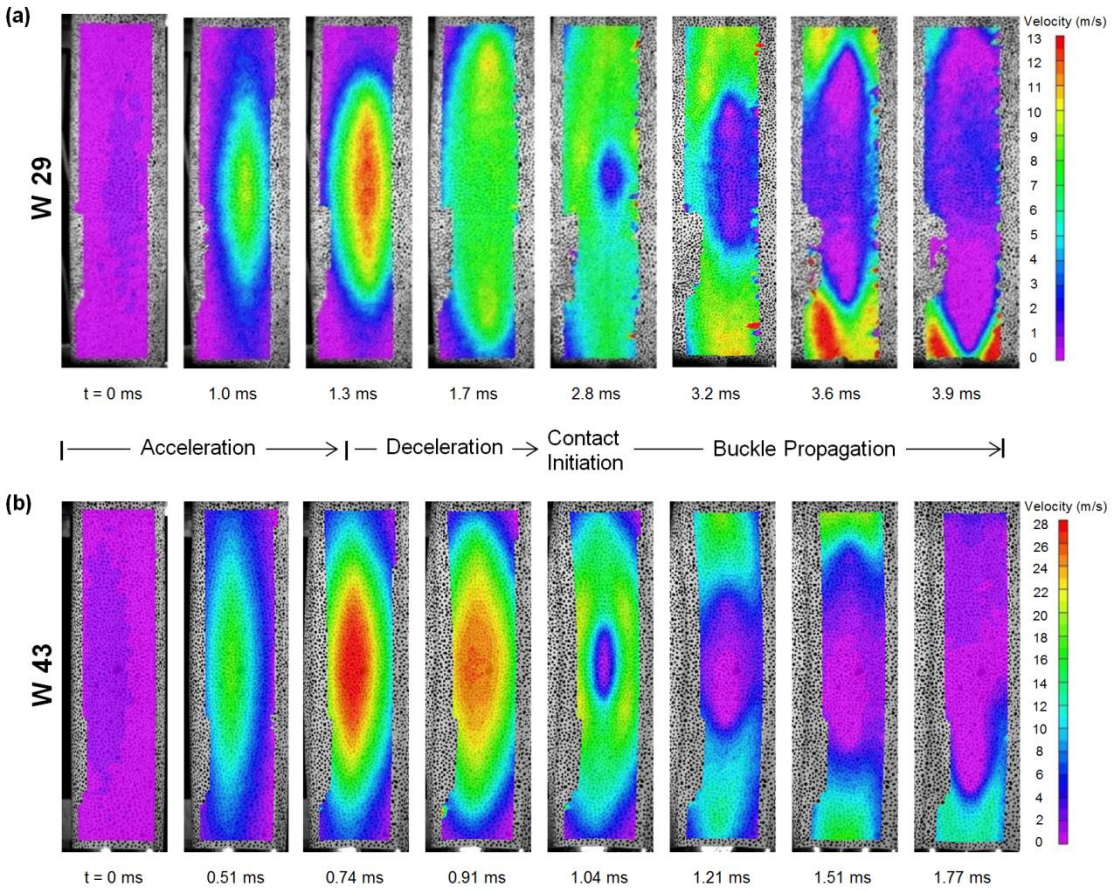

Figure 3.5 Full-field out-of-plane velocity contours for W29 and W43. Distance between M and M+/M- is equal to l/4

The velocity contours for W29, as shown in Figure 3.5 (a) show that the evolution of velocity is significantly different from a free-field implosion experiments. The implodable accelerates up to time t = 1.3 ms and reaches a peak center point velocity of 12 m/s. During this period, the velocity variation along the length is almost linear similar to earlier studies [20]. The deformation process after this instance differs from free-field situations. In a free field case, the implodable reaches its maximum velocity just before contact initiation. Thus, the kinetic energy of the implodable reaches its maxima prior to contact initiation. On the contrary in the open tube confined implosion case, the implodable undergoes deceleration at the center for about 1.5 ms

prior to contact. From a structural perspective, this phenomenon suggests that the resistance to deformation for implodable exceeds beyond the driving force applied by surrounding fluid's pressure in open tube confined implosion. In turn, the kinetic energy gained during acceleration phase is consumed in further plastically deforming the implodable. From a fluid perspective, there is a limited amount of potential energy, in the form of hydrostatic pressure, due to the confinement. As the implodable collapses, the low pressure emitted, effectively lowers the hydrostatic pressure within the confinement, slowing the collapse, and initiating particle velocity from the open top towards to closed bottom. As the water flow restores some of the hydrostatic pressure, the deceleration slows down prior to wall contact. Additionally, for lower collapse pressures, such as the W29 experiment, a second acceleration phase starts prior to wall contact and for higher collapse pressures, such as the W43 experiment, the first acceleration phase is sufficiently high to cause wall contact prior to the deceleration phase.

Another change in deformation mechanics is also observed during the W29 experiment as compared to a free-field case. The deformation profile along the longitudinal direction has been earlier shown to be a linear/half-sine wave for mode-2 cylindrical geometry [20-21]. In W29 experiment, the linear profiled deformation mode is observed till the instance of peak velocity. Subsequently, it is seen that the points away from the center along the longitudinal direction gain velocity as seen between t = 1.3 – 2.8 ms, while central region undergoes deceleration. This deformation behavior appears to be unique to open tube confined implosion. This essentially indicates the transition of the longitudinal deformation mode from a lower

order mode (half-sine wave) to a higher order mode (multiple sine waves). The primary reason for such transition is that the strain energy associated with higher-order longitudinal modes at this instance is lower than the strain energy of lower order mode.

The deceleration in the implodable is followed by contact initiation at the center point at t = 2.8 ms. Later, the point contact grows in both diametrical and longitudinal direction as seen in time t = 3.2 ms. This contact front is seen to increase with an average velocity of 70 m/s, which is smaller as compared to that from free-field implosion experiments (between 150 – 200 m/s) [10]. This lower contact front propagation velocity and the deceleration of walls prior to wall contact are the effects of the open-tube confined environment. A typical implosion is a relatively longer event (of the order of ~ 1 ms) as compared to the radial reflection-free time period inside the confining tube (~ 120 μs). Thus, the confining tube inhibits the free-propagation of low-pressure implosion waves during initial collapse period of implodable. As a result, these waves reflect back from the inner walls of the confining tube and superimpose leading to significant dynamic pressure drop. Therefore, the pressure in near-field of implodable is always smaller as compared to a similar free-field implosion experiment. With significant pressure drop, the driving forces to continue the implosion process decreases over time and hence the overall structural velocities are smaller as seen in Figure 3.5.

It is interesting to note that the velocity contours for W43, shown in Figure 3.5 (b), are relatively similar as seen in free-field situations due to high collapse pressure of the geometry. The implodable accelerates till time t = 0.81 ms, reaching a peak

velocity of 28 m/s. In comparison to W29, a relatively smaller deceleration phase (~ 0.2 ms) is seen, which causes a slight drop in velocity (from 28 m/s to 24 m/s) prior to contact initiation at t = 1.03 ms. The average velocity of contact growth for W43 is ~ 95 m/s, which is 35% higher than W29.

3.2. Velocity History Comparison

In order to compare the velocity history for each collapse pressure, the center point velocity for each experiment is plotted in Figure 3.6 (a). Figure 3.6 (b) and (c) plots the following parameters: 1) peak velocities, 2) velocities prior to contact initiation, 3) average velocities, 4) acceleration time, and 5) deceleration time. It is seen that experiments at higher collapse pressures (W43) tend to maintain similar signature as of free-field experiments while at lower collapse pressures (W29, W35, and W38) show significant changes in velocity by undergoing deceleration prior to contact making under pressure phase to be relatively longer, as shown in both Figure 3.6 (a) and (c).

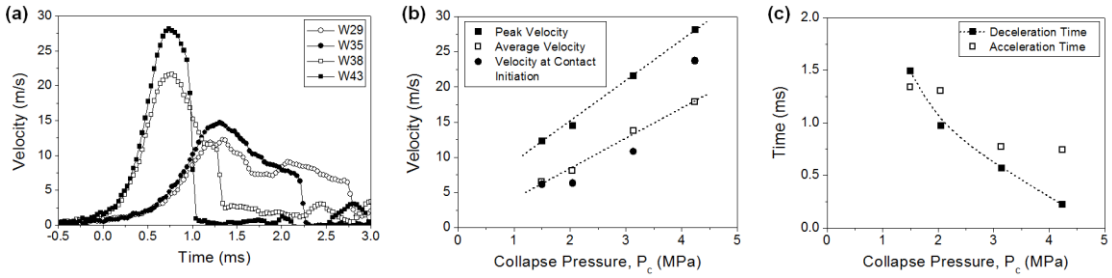

Figure 3.6 (a) Center point velocity (b) Peak/average velocity and velocity at contact initiation (c) Acceleration and deceleration time

Both the peak velocity and the average velocity indicate an approximately linearly increasing trend as P_c increases. The velocity at contact initiation is also an important parameter because the free-field implosions exhibit contact initiation during its highest

velocity while implosions in confining tube exhibit only a fraction of its highest the velocity during contact initiation. In this study, all experiments except W43 indicate that the velocity at contact initiation is ~ 50% of the peak velocity; W43 exhibits contact at 85% of its peak velocity. Thus, it can be seen that the effect of a confinement on structural deformations is significant in lower collapse pressure.

3.3. Pressure History Comparison

The evolution of implosion waves is very similar to all the experiments in this study. To understand the overall behavior of pressure evolution throughout the space, a time evolution of the pressure for each case is shown in Figure 3.7. The pressure contour levels have been normalized with respect to the collapse pressure for relative comparison.

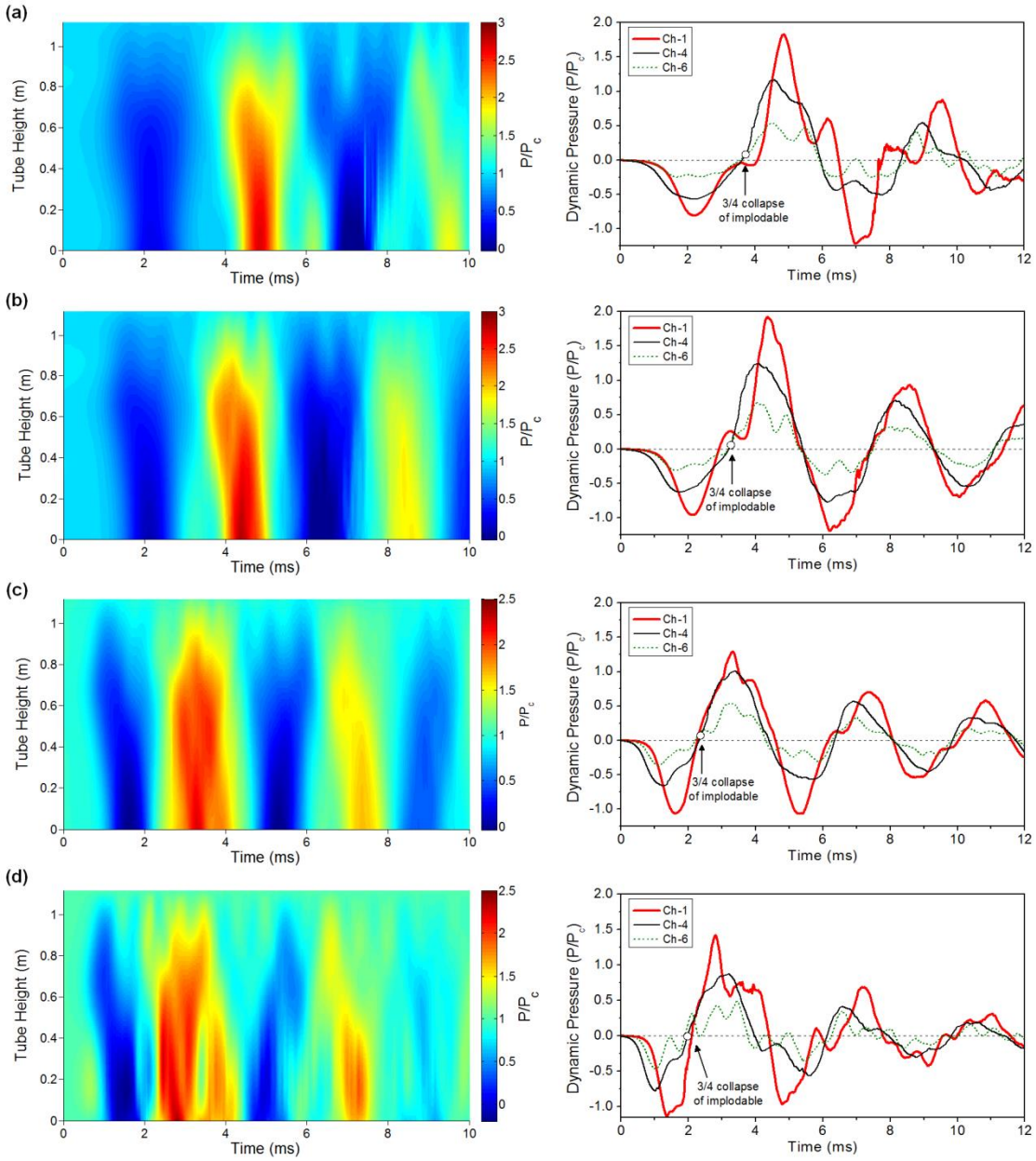

Figure 3.7 Pressure history and its evolution throughout space (a) W29 (b) W35 (c) W38 and (d) W43

The incompressible nature of water causes a sudden drop in the pressure at the nearest sensor (Ch-4) with the progress of implosion process, and these low-pressure waves travel in both axial directions (Ch-4 → Ch-1 (downwards) and Ch-4 → Ch-7 (upwards)). As the upward end is open to the hydrostatic pressure, these waves reflect as a free boundary and generate high water velocity at the open end towards inside.

The low-pressure wave from the implosion leads to the in-rush of water from the open end to compensate for the low pressure present in the confining tube.

At the completion of the collapse of the implodable, the velocity of water at the open end is still in the downwards direction. This in-rushing water hits the bottom end-plate, leading the momentum of the water at the end-plate to change abruptly. Thus the following in-rushing water over-compresses the water in front and a high-pressure water hammer forms inside the confining tube at the closed end-plate. As the highest change of momentum occurs at the closed end-plate, the intensity of the hammer pressure is highest at this location similar to seen in [16]. For experiments conducted in this study, the maximum pressure at the end-plate is seen to be between $1.35\,P_c$ and $1.92\,P_c$.

3.4. Correlation between Pressure History and Structural Deformations

In order to correlate the features in pressure history with structural deformations, the instance is marked by o in Figure 3.7 at which the collapse has propagated to half longitudinal length resulting in the ¾ collapse of the implodable volume. As soon as the collapse is complete, the high-pressure hammer wave is seen to evolve inside the confining tube. This observation can also be understood by the interaction of implosion wave with the confining tube. During collapse, the low-pressure waves are emitted from the surface of implodable. Hence, the low pressures within the confinement don't allow the dynamic pressure surrounding the implodable to rise beyond P_c. Only after wall contact, the high pressures above P_c are emitted inside the confining tube to rise above P_c. Therefore, the time duration of under-pressure region

observed near implodable during confined implosions is approximately equal to the duration of the implodable's collapse.

As seen from DIC measurements, higher values of P_c generate faster implosions, and so smaller collapse durations. Therefore, the hammer wave evolves faster for higher P_c as shown in Figure 3.7. The hammer wave evolves at ~ 2.1 ms for W43, while it evolves at ~ 4.1 ms (approximately two times that for W43) for W29.

3.5. Average Hammer Pressure

The average hammer pressure of the first cycle observed at the end-plate during the water hammer wave impact is found to be increasing linearly with P_c as shown in Figure 3.8. It is also seen that the peak hammer pressure also has an increasing trend, but not in linear fashion. It indicates that the generation of peak hammer pressure occurs in a transient manner, in which the changes in fluid velocity history significantly affect its value. On the other hand, the average hammer pressure represents the overall strength of the hammer wave, which directly correlates to the critical collapse pressure of the experiment.

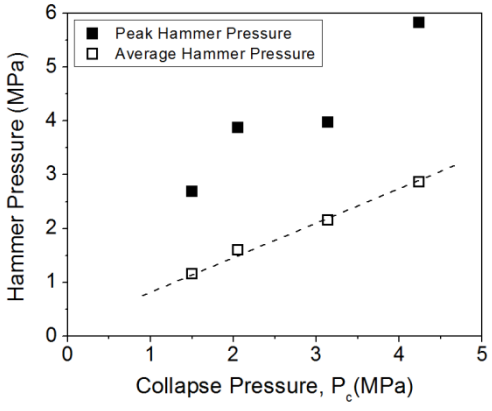

Figure 3.8 Average and Peak Hammer Pressure for all the experiments

3.6. Hammer Pressure Behavior

The behavior of pressure waves inside the semi-confining environment seen during these experiments can be predominantly explained through fluid mechanics of piping systems. Specifically, the impulses caused by the hammer pressures can be derived from Joukouwsky's Equation [22], Eq. (1); where pressure, P, is expressed as a function of fluid density, ρ, coupled pressure wave speed, c_f, fluid velocity, v and time, t.

$$\frac{dP}{dt} = \rho c_f \frac{dv}{dt} \tag{1}$$

The impulse, I, caused from the pressure surge at the closed end of the confining tube, can be obtained through the integration of its force with respect to time; where force is assumed to be uniform and planar and is a product of hammer pressure and cross-sectional area of the confining tube, A. This method leads to a constant value of $\rho c_f V$ for the total impulse as seen in Eq. (2); where V is the volume change in the confining tube (or the volume of air inside the implodable).

$$I = A\iint \frac{dP}{dt} dtdt = \rho c_f \iint \frac{d(Av)}{dt} dtdt = \rho c_f \iint \frac{d^2V}{dt^2} dtdt = \rho c_f V \tag{2}$$

The, coupled pressure wave speed inside a pipe, c_f, can be estimated as,

$$c_f = \left(\frac{L_{al}}{L_{ac}+L_{al}}\right)\frac{c_w}{\sqrt{1+\frac{KD}{E_{al}h}}} + \left(\frac{L_{ac}}{L_{ac}+L_{al}}\right)\frac{c_w}{\sqrt{1+\frac{KD}{E_{ac}h}}} \tag{3}$$

, which represents a weighted average of coupled pressure wave speeds in the aluminum section ($c_w \Big/ \sqrt{1+\frac{KD}{E_{al}h}}$) and the acrylic section ($c_w \Big/ \sqrt{1+\frac{KD}{E_{ac}h}}$) [22-23]. This averaging takes into account for the 152 mm acrylic window section placed at the

longitudinal location same as of implodable. The details of parameters employed in Eq.(3) can be found in Table 3.2.

Table 3.2 Dimensions and Properties of Confining Tube

Parameter	Value
c_w (Wave speed in water)	1483 m/s
K (Bulk modulus of water)	2.2 GPa
h (Wall thickness of confining tube)	25.4 mm (1.00 in)
D (Diameter of confining tube)	177.8 mm (7.00 in)
E_{ac} (Elastic modulus of aluminum)	69 GPa
E_{al} (Elastic modulus of acrylic)	3.17 GPa
L_{al} (Length of aluminum section)	965 mm (38.00 in)
L_{ac} (Length of acrylic section)	152 mm (6.00 in)

From Eq. (3), c_f is found to be 1226 m/s. The frequency of pressure wave oscillation, f , in a confining open tube that is partially open to the environment can be obtained as a function of wave speed (c_f) and the total length of the confining tube, $L = L_{al} + L_{ac}$, as seen in Eq. (4) [17]. Also, assuming that as each wave passed through the specimen, the part of the wave that interacts with the cross-sectional area of the specimen, A_s , is blocked and does not propagate, then a loss factor, l , can be defined as the ratio of areas. Since the cross-sectional area of the specimen is relatively small (< 5%) when compared to the total cross-sectional area of the confining tube, any viscous damping during fluid flow can be ignored, and the losses can be estimated to be solely a ratio of areas as shown in Eq. (5).

$$f = \frac{c_f}{4L} \tag{4}$$

$$l = 1 - \left(\frac{A - A_s}{A} \right) = \frac{A_s}{A} \tag{5}$$

Experimentally, it is seen that pressure, *p*, has a sinusoidal behavior that decays at every cycle n by the factor of l as seen in Eq. (6). From this pressure behavior, the total impulse from Eq. (2) can be distributed throughout time (after normalizing it with a factor α) in order to create a function for impulse as shown in Eq. (7).

$$p(t) = \cos(2\pi ft) - (n)(l)\cos(2\pi ft) \tag{6}$$

$$I(t, P_c) = K\frac{\rho c_f V}{\alpha(t)}\int_0^t p(t)dt; \quad \text{where} \quad \alpha(t) = \int_0^t |p(t)|dt \quad \text{and} \quad \begin{cases} K > 1 & \text{for} \quad n < 1 \\ K = 1 & \text{for} \quad n > 1 \end{cases} \tag{7}$$

Note that the specimen collapse due to the implosion process adds additional energy to the hammer pressure that is not accounted for in the hammer theory by itself. The maximum impulse was observed to be linear with respect to collapse pressure as seen in Figure 3.9 (a), in turn, a correction factor, K, was added to the impulse function in Eq. (7) and is only significant during the first cycle of oscillation. For the particular case studied, K is also linear with respect to collapse pressure and can be obtained from Figure 3.9 (c) (note that K could also be a function of velocity since there is a relationship between collapse pressure and velocity).

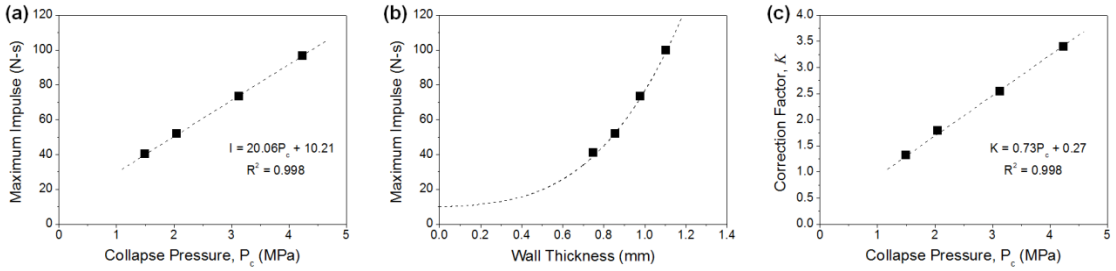

Figure 3.9 Trend of maximum peak impulse value as a function of (a) collapse pressure, (b) implodable wall thickness, and (c) correction factor as a function of collapse

The theoretical function in Eq. (7) can be plotted versus the experimental results for each of the four cases as shown in Figure 3.10. It is seen that impulse calculation from experimental results correlates well with that from the hammer theory model. For

higher collapse pressures, the frequency of oscillations and magnitudes from hammer theory becomes prominent.

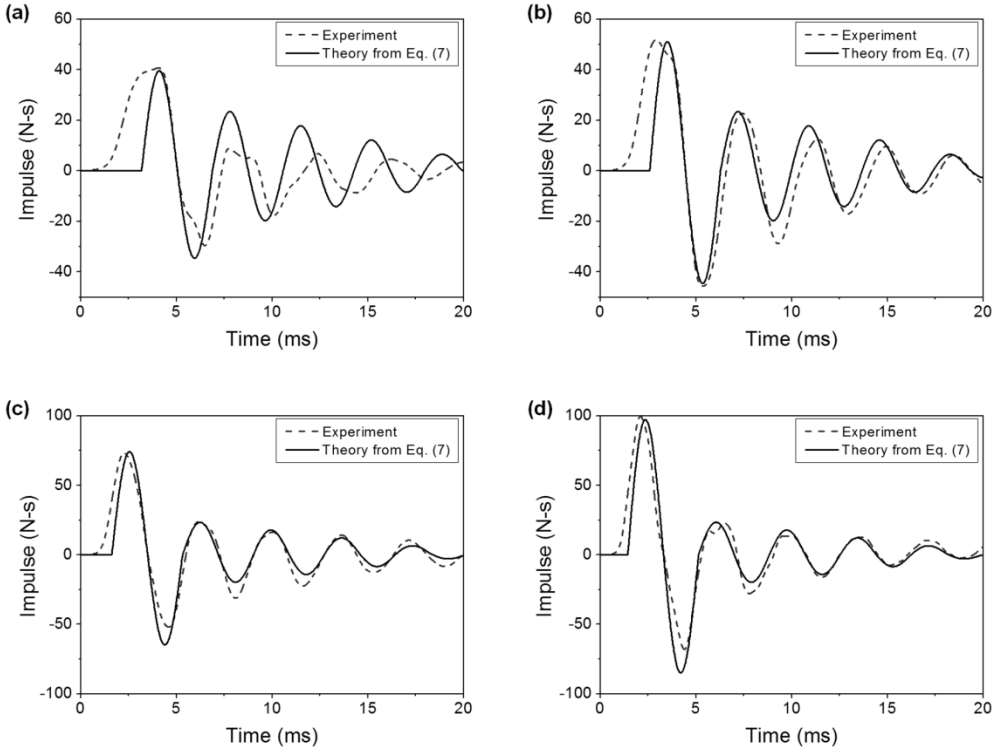

Figure 3.10 Experimental vs. theoretical results for: (a) W29 (= 1.50 MPa); (b) W35 (= 2.05 MPa); (c) W38 (= 3.14 MPa); and (d) W43 (= 4.24 MPa)

The maximum impulse from Eq. (7) can also be represented as a function of the implodable structure's geometry, elastic properties, and collapse mode number, m, through the use of the mon-Mises stability Eq. (8). [24] Figure 3.9 (b) shows maximum impulse at the closed end as a function of wall thickness. Note that zero wall thickness ($w = 0$) would also yield in $P_c = 0$, thus it implies an instantaneous disappearance of the implodable volume at atmospheric pressure; which leads to water flow then a hammer wave (of $I = 10.21\,Ns$). As shown by Figure 3.9 (b), wall thickness has a significant impact in the maximum impulse. However, as wall thickness increases (assuming outer diameter and length are held constant) the air

volume inside the tube marginally decreases, in turn the impulse contribution from the volumetric change slightly decreases. From this observation, the maximum impulse at the closed end will converge to the maximum impulse released from implosion as $w \to r$. In other words, hammer waves from imploding "thick walled" structures can be expected to have similar magnitude to the waves released from the implosion.

$$P_c = \frac{Ew}{r\left(m^2+\frac{1}{2}\left(\frac{\pi r}{L}\right)^2-1\right)}\left(\frac{1}{\left(\left(\frac{Lm}{\pi r}\right)^2+1\right)^2}+\frac{w^2\left(m^2+\left(\frac{\pi r}{L}\right)^2-1\right)^2}{12r^2(1-\upsilon^2)}\right) \tag{8}$$

4. Conclusions

An experimental investigation is conducted to understand the evolution of water hammer type waves resulting from an implosion occurring inside an open-ended confining tube. Both pressure measurements along with high-speed 3-D DIC measurements are conducted to correlate the structural deformation with pressure history. The key findings of this study are as follows:

- The presence of open-ended confining tube around an implodable significantly affects the implosion process. The velocity during the collapse is highly reduced due to the significant pressure drop from the superposition of low-pressure implosion waves inside the confining tube. The peak velocity and the average velocity prior to wall contact are found to be linearly varying with the collapse pressure.
- The environment of the open-ended confining tube causes the implodable volume to decelerate well before the initiation of wall contact. This duration is also found to increase with decreasing collapse pressure, and it reaches a significant duration of 1.5 ms for the lowest collapse pressure experiments conducted in this study.

- The peak strength of water hammer wave in this study is found to be in between 1.35 P_c and 1.92 P_c . The average strength of water hammer wave is 0.7 to 0.75 P_c .
- The hammer impulse at the closed end is obtained by the superposition of two different impulse waves. The first is generated by the abrupt momentum changes when the specimen implodes. The strength of this wave is a function of collapse pressure. The second wave is produced by the changes in water momentum at the closed end. The strength of this second wave is a function of volumetric displacement as shown by Eq. (2).
- Water hammer theory can accurately predict the behavior of open tube confined implosions if the size of the implodable is small when compared to the size of the confinement.
- The calibration using a submerged calibration grid can successfully account for the refractive index mismatch between the water/cylindrical acrylic window/flat acrylic window/air. The calibration experiments reveal that the both the in-plane and out-of-plane measurements can be measured using this modified 3-D DIC calibration procedure within 5% error.

Acknowledgements

The authors kindly acknowledge the financial support provided by Dr. Thomas Fu and Dr. Stephen Turner of the Office of Naval Research under Grant Nos. N00014-15-1-2046 and N00014-12-1-0382 respectively.

References

[1] J. LeBlanc, J. Ambrico, and S. Turner, "Underwater implosion mechanics: experimental and computational overview". Blast Mitig. - Exp. Numer. Stud. (2014).

[2] J. Isaacs, and A. Maxwell, "The ball-breaker; a deep water signaling device". J Mar Res 11:63–68 (1952).

[3] J. Urick, "Implosions as sources of underwater sound". J Acoust Soc Am 35:2026–2027. doi: 10.1121/1.1918898 (1963).

[4] B. Vanzant, J. Russell, A. Schraeder, and E. DeHart, "Near-Field Pressure Response Due to a Sphere Imploding in Water". Southwest Research Institute (1967).

[5] F. Vath, and W. Colletti, "Development of Buoyancy Material for the Deep Submergence Search Vehicle: Evaluation of Sympathetic Implosion of Buoyancy Modules". Material Sciences Division , U.S. Naval Applied Science Laboratory, Brooklyn, New York (1969).

[6] M. Orr,and M. Schoenberg, "Acoustic signatures from deep water implosions of spherical cavities". J Acoust Soc Am 59:1155–1159. doi: 10.1121/1.380977 (1976).

[7] S. Turner, "Underwater implosion of glass spheres". J Acoust Soc Am 121:844–852. doi: 10.1121/1.2404921 (2007).

[8] S. Turner, and J. Ambrico, "Underwater implosion of cylindrical metal tubes". J Appl Mech 80:011013. doi: 10.1115/1.4006944 (2012).

[9] C. Farhat, K. Wang, A. Main, et al., "Dynamic implosion of underwater cylindrical shells: Experiments and Computations". Int J Solids Struct 50:2943–2961. doi: 10.1016/j.ijsolstr.2013.05.006 (2013).

[10] S. Gupta, V. Parameswaran, M. Sutton, and A. Shukla , "Study of dynamic underwater implosion mechanics using digital image correlation". Proc R Soc Math Phys Eng Sci 470:20140576. doi: 10.1098/rspa.2014.0576 (2014).

[11] M. Pinto, S. Gupta, and A. Shukla, "Hydrostatic Implosion of GFRP Composite Tubes Studied by Digital Image Correlation". J Press Vessel Technol 137:051302–051302. doi: 10.1115/1.4029657 (2015).

[12] M. Pinto, S. Gupta, and A. Shukla, "Study of implosion of carbon/epoxy composite hollow cylinders using 3-D Digital Image Correlation". Compos Struct 119:272–286. doi: 10.1016/j.compstruct.2014.08.040 (2015).

[13] R. Chamberlin, E. Guzas, and J. Ambrico, "Energy balance during underwater implosion of ductile metallic cylinders". J Acoust Soc Am 136:2489–2496. doi: 10.1121/1.4896744 (2014).

[14] S. Gupta, J. LeBlanc, and A. Shukla, "Mechanics of the implosion of cylindrical shells in a confining tube". Int J Solids Struct 51:3996–4014. doi: 10.1016/j.ijsolstr.2014.07.022 (2014).

[15] S. Gupta, J. LeBlanc, and A. Shukla, "Implosion of longitudinally off-centered cylindrical volumes in a confining environment". J Appl Mech 82:051001. doi: 10.1115/1.4029917 (2015).

[16] S. Gupta, H. Matos, J. LeBlanc, and A. Shukla, "Shock initiated instabilities in underwater cylindrical structures". Journal of the Mechanics and Physics of Solids, 95, 188-212. doi:10.1016/j.jmps.2016.05.034 (2016).

[17] L. Costa, and S. Turner, "Implosion testing within a pipe". NAVSEA NUWC-NPT Technical Memo (2008).

[18] S. Gupta, J. LeBlanc, A. Shukla, "Sympathetic underwater implosion in a confining environment". Extreme Mech Lett 3:123–129. doi: 10.1016/j.eml.2015.03.007 (2015).

[19] Correlated Solutions Inc., http://www.correlatedsolutions.com (date last viewed 02/19/16).

[20] L. Gish, and T. Wierzbicki, "Estimation of the underwater implosion pulse from cylindrical metal shells". Int J Impact Eng 77:166–175. doi: 10.1016/j.ijimpeng.2014.11.018 (2015).

[21] S. Timoshenko, and J. Gere, "Theory of elastic stability". Dover Publications, Mineola, N.Y (1963).

[22] N. Joukowsky , "Über den hydraulischen Stoss in Wasserleitungsröhren [Hydraulic shock in water supply pipes]". Mémoires de l'Académie Impériale des Sciences de St.-Pétersbourg, Series 8, 9(5), 1-71 (1900).

[23] D. Korteweg, "Ueber die Fortpflanzungsgeschwindigkeit des Schalles in elastischen Röhren. Annalen der Physik und Chemie [Sound propagation velocity in elastic tubes]". Annalen der Physik und Chemie, New Series 5, 525-542 (1878).

[24] R. Von Mises, "The critical external pressure of cylindrical tubes under uniform radial and axial load", translated by D. F. Windenburg. Stodolas Festschr, 418–430 (1929).

CHAPTER 4. Structural Instability and Water Hammer Signatures from Shock-Initiated Implosions in Confining Environments

by

Helio Matos, Sachin Gupta, and Arun Shukla

Dynamic Photo Mechanics Laboratory, Department of Mechanical, Industrial and Systems Engineering, University of Rhode Island, Kingston, RI 02881

Published in the Mechanics of Materials journal

Matos, H., Gupta, S., & Shukla, A. (2017). Structural instability and water hammer signatures from shock-initiated implosions in confining environments. Mechanics of Materials. doi:10.1016/j.mechmat.2016.12.004

Abstract

An experimental study is conducted to investigate the dynamic response and instability of cylindrical structures subjected to hydrostatic pressure in conjunction with explosive loading. Full-field displacements/velocities, and localized pressures, of imploding aluminum structures within a confining environment are captured during the experiments. Also, polyurea coatings of 1:1 volume ratios are evaluated as a possible energy mitigation technique. Two high-speed cameras are used to capture the imploding structures while various dynamic pressure transducers measure the emitted pressure pulses. The specimens are confined inside a thick-walled cylindrical structure that had one end open to the hydrostatic pressure inside the pressure vessel and the other end closed. This confinement configuration generates a water hammer at the closed end of the confinement. The results of these experiments indicate that after the collapse, pressure profiles of hydrostatic and explosive initiated implosions are about the same. Moreover, the energy from the implosion's high-pressure pulses, present at the confinement's closed end, was greater than the energy of the explosive itself due to the water hammer effect. The polyurea coatings used in this study caused a sufficient phase shift in the implosion pressures such that the hammer and implosion high-pressure pulses were not superimposed; thus, the maximum pressures and energy after the implosion was reduced. However, the polyurea coatings did not significantly mitigate neither the hammer nor the implosion pressures individually. Finally, a non-linear Riks model from ABAQUS was used to show that the energy input requirement for dynamic-initiated implosions decreases rapidly as initial hydrostatic pressure increases.

1. Introduction

In this study, an experimental investigation is conducted to evaluate the implosion pressure pulses, water hammer waves, and their mitigation in a confined environment while subjected to shock loadings. This research arises from the concern of damage to naval and marine structures such as underwater pipelines, submarines, and autonomous underwater vehicles (AUVs). When these structures are submerged deep underwater and experience high hydrostatic pressures, they can instantaneously collapse inward and release strong propagating shockwaves in a process known as implosion [1-5]. In a confining environment, the implosion's pressure waves and any induced particle velocity can interact with its surroundings leading to a water hammer wave that is even stronger and more destructive than the implosion's pressure waves. Previous work shows the water hammer pressures reaching values of 150-200% the implosion's peak pressures [6-8].

Implosion has been of interest to the marine community since the mid-1900s [3-5]. However, one key accident that renewed the interest in this topic was the 2001 Super-Kamiokande laboratory accident in Japan where one photomultiplier tube imploded, and the pressure pulses from this implosion caused adjacent tubes to implode; leading to a chain reaction that destroyed 7000 photomultiplier tubes [9]. More recently in 2010, an AUV known as ABE was lost off the coast of Chile due to the glass sphere (that controls buoyancy) imploding; which created high pressure pulses that destroyed all onboard systems [10]. Also, in 2014 the multi-million dollar AUV, Nereus, imploded off the coast of New Zealand [11]. These recent events highlight implosion as an ongoing issue.

The current work available on implosion characterizes the collapse mechanics for free-field environments [12-17]; meaning that the pressure pulses emitted during the implosion travel undisturbed. There is very limited work available on implosions within confining environments. These include implosions within a fully confined environment [18-20]; where it was shown that the limited hydrostatic pressure drastically affects the implosion process. Also, the implosions within a confining environment that are open to a larger water body (held at the same hydrostatic pressure) leads to water hammers [6-8]. Water hammer is a well-established phenomenon in terms of piping mechanics [21-24], but there is no work done on implosion-induced water hammers in terms of shock-initiated implosions.

Polyurea has gained research interest in recent years due to its energy absorbing characteristics under dynamic loading. Some of the latest work was done in the mitigation of the energy emitted during a free-field environment implosion, specifically through polyurea coating [25-27]. No work is available for the mitigation of energy emitted during a confining environment implosion; where the implosion is initiated hydrostatically or with an underwater explosive (UNDEX).

This study develops an experimental scheme to determine the localized pressure history emitted during the implosion of aluminum structures within a confining environment as well as the instability of these structures. The Digital Image Correlation (DIC) technique captures real-time high-speed deformation for understanding fluid-structure interaction during implosion event. Implosions are initiated hydrostatically in conjunction with an UNDEX. Moreover, the mitigation effects of polyurea coated aluminum structures are analyzed.

2. Experimental Procedures

2.1. Specimen Geometry and Experimental Facility

To perform the implosion experiments, a 1.12 m (44.0 in) long, 25.4 mm (1 in) thick walled, cylindrical confinement is placed inside a 2.1 m diameter semi-spherical pressure vessel as shown in Figure 4.1 (a), (b), and (c). The confinement is made of three modular pieces; (1) an upper aluminum section that has the top open to the pressure vessel's environment; (2) a middle optically clear acrylic section that views the implodable specimen; and (3) a bottom aluminum section that has a closed end as shown in Figure 4.1 (c). All confinement sections have 178 mm (7.0 in) inner diameter and are stacked concentrically. Eight dynamic pressure sensors (PCB 138A05, PCB Piezotronics, Inc., Depew, NY) are located along the walls of the confinement and are used to obtain pressure data at 2 mega samples per second. Additionally, two high-speed cameras (Photron SA1 from Photron USA, Inc., San Diego, CA) outside the vessel are used to capture high-speed images at 40,000 frames per second (each image has a 192x656 spatial pixel resolution). The photographs from the high-speed cameras are captured through optically clear windows located along the midspan of the vessel, and the center acrylic section of the confinement. These images are later used in Digital Image Correlation analysis.

Two implosion initiation cases are studied. The first is a hydrostatic case, where the implodable collapses due to a critical collapse pressure. The second is an explosive case, where an UNDEX (RP-80 explosive charge) is placed inside the confining structure, 50.8 mm (2.0 in) below the open end (shown in Figure 4.1(c)). The UNDEX

is ignited at 70% of the critical collapse pressure of the implodable. The RP-80 explosive charge is composed of 80 mg PETN (initiating explosive) and 123 mg RDX (output explosive). The explosive material is sealed inside a cylindrical aluminum jacket that is 0.18 mm (0.007 in) thick, 20.9 mm (0.824 in) long, and has a 7.5 mm (0.295 in) outer diameter.

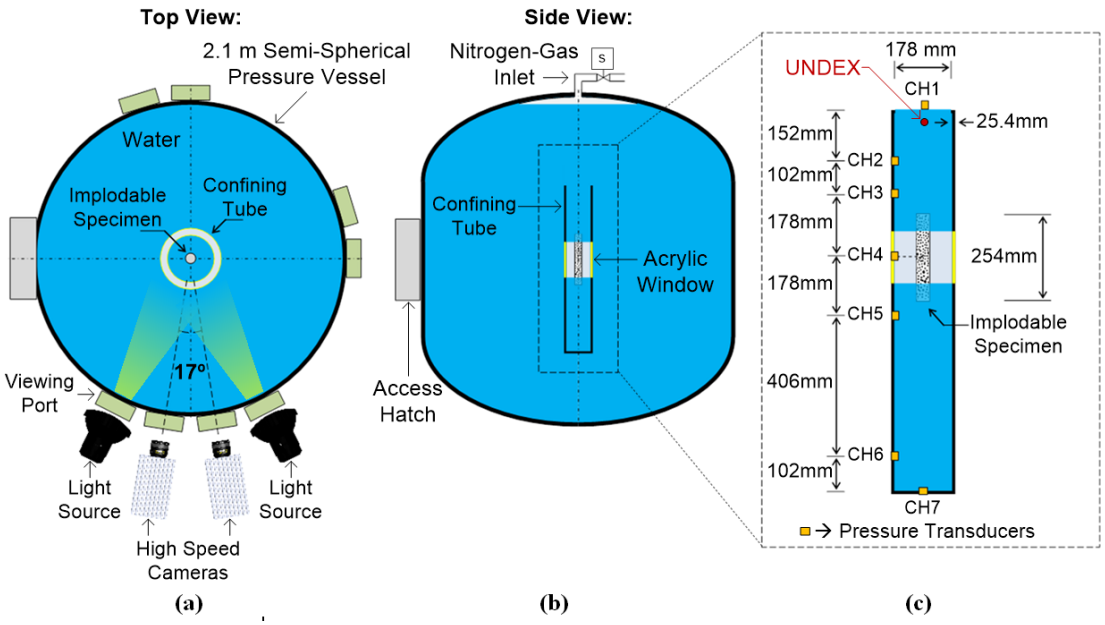

Figure 4.1 Experimental setup viewed from the (a) top, (b) side, and (c) detailed side section

The implodable specimens are aluminum 6061-T6 tubes with a 38.1 mm (1.5 in) outer diameter, 0.71 mm (0.028 in) wall thickness, and 254 mm (10.0 in) of unsupported length and are coated with high-contrast speckle patterns. The speckle patterns are created by randomly placing flat-black paint dots (sized 9-12 pixels per dot) on a flat-white painted background until approximately 50% of the surface area of the specimens are covered by the black dots. The specimens are sealed using two aluminum end caps with o-ring seals and placed concentric to the confining cylindrical structure as shown in Figure 4.1 (c). The end caps prevent water penetration in the specimen; therefore during the experiments high-pressure water surrounds the

specimen while low-pressure air resides inside. To perform the experiments, the pressure vessel is filled with filtered water, then slowly pressurized with compressed nitrogen gas until (1) the specimen implodes (at 1.51 MPa) or (2) the desired hydrostatic pressure for the UNDEX experiments is reached (1.06 MPa in this case). The tank's water is re-filtered (to remain optically clear) and re-used between experiments.

The high-speed images are analyzed using commercially available DIC software (VIC3D 7 from Correlated Solutions, Inc., Columbia, SC) to measure full-field displacements across the viewable surface of the specimen by triangulating the position of each unique feature in the speckle pattern. Previous work [6, 15] outlines the calibration procedures that validate the accuracy of the DIC results in the underwater environment (where changes in refractive index are present). It was found that the flat-surface windows (located at the midspan of the pressure vessel) need to be perpendicular to the viewing axis [15], and the cylindrical window (from the confining structure) needs to be concentric to where viewing axis of both cameras meets (optical center) to minimize DIC displacement errors [6]. For this study, the in-plane displacement errors are ~2%, and the out-of-plane errors are ~5%.

2.2. Polyurea Coating

The polyurea used (HM-VK^{TM} from Specialty Products, Inc., Lakewood, WA) is a two-part product that is manually applied to the aluminum tube as it rotated longitudinally. Prior to application, the specimen tube was lightly sanded and cleaned with acetone to improve adhesion. Masking tape was used at each end of the tube (set

to a predetermined thickness) as a scraper guide to wipe off the excess polyurea. For interior coating, the entire setup is angled so the polyurea can be poured from the center guide's end.

Specimens with polyurea coatings have a uniform coating placed on the exterior or interior of the tube similar to previous work [26, 27]. The coating thicknesses used are based on a 1 polyurea: 1 aluminum volume ratio for both exterior and the interior coatings; meaning an average coating thickness of 0.69 mm (0.027 in) for exterior coatings, and 0.74 mm (0.029 in) for interior coatings. In total, there are six cases analyzed in this study as shown in Table 4.1. Each case has been repeated three times to validate the results.

Table 4.1 Experimental series details

Cases	Polyurea Coating	Collapse Method	Collapse Pressure (MPa)
Hydrostatic No Coating	None	Hydrostatic	1.51 +/- 0.03 (Critical Pressure)
Hydrostatic External Coating	Exterior		
Hydrostatic Internal Coating	Interior		
UNDEX No Coating	None	UNDEX	1.06 +/- 0.01 (Pre-Pressure)
UNDEX External Coating	Exterior		
UNDEX Internal Coating	Interior		

3. Results and Discussion

3.1. UNDEX Charge Characterization

Experiments were performed without the implodable specimen, and the environmental pressure was set to 1.06 MPa to mimic the UNDEX implosions conditions in order to characterize the explosive and bubble dynamics as shown in Figure 4.2 (a). Moreover, the modular cylindrical confinement structure was re-arranged such that the acrylic window is located at the top (while keeping the same sensor locations) as shown in Figure 4.2 (b).

The UNDEX pressure can be visualized inside the confinement and throughout time using the history pressure map shown in Figure 4.2 (c). The vertical axis in Figure 4.2 (c) represents the confinement location, the horizontal axis is time given in ms (where t* = 0 denotes the UNDEX ignition time), and the color contour represents pressure in MPa. After the UNDEX combusts, high-pressure wave (shown in Figure 4.2 (c) as P^{+}) travels down the confining structure, followed by cavitation along the confinement walls (shown in Figure 4.2 (c) as P^{-}). The high pressures and velocities from the explosive charge lead to the formation of a cavitation bubble at the charge location. The bubble grows until the surrounding pressure is sufficiently large to cause the bubble to collapse. When the bubble fully collapses, it emits high-pressure waves which lead to a subsequent cavitation bubble to form and so on [28]. The high pressures of some of the bubble cycles can be seen in Figure 4.2 (c).

A pressure frequency map can also be constructed using the UNDEX pressure data as shown in Figure 4.2 (d). The vertical axis in Figure 4.2 (d) represents the confinement location; the horizontal axis is the frequency of the pressure waves, and the color contour stands for the system's gain which is indicative of the frequency's prominence. It is shown that the bubble collapse cycles leads to the prominent frequency responses seen between 300 and 400 Hz about the UNDEX locations. Also, the 225 Hz response at the closed end of the confinement is indicative of a water hammer [21].

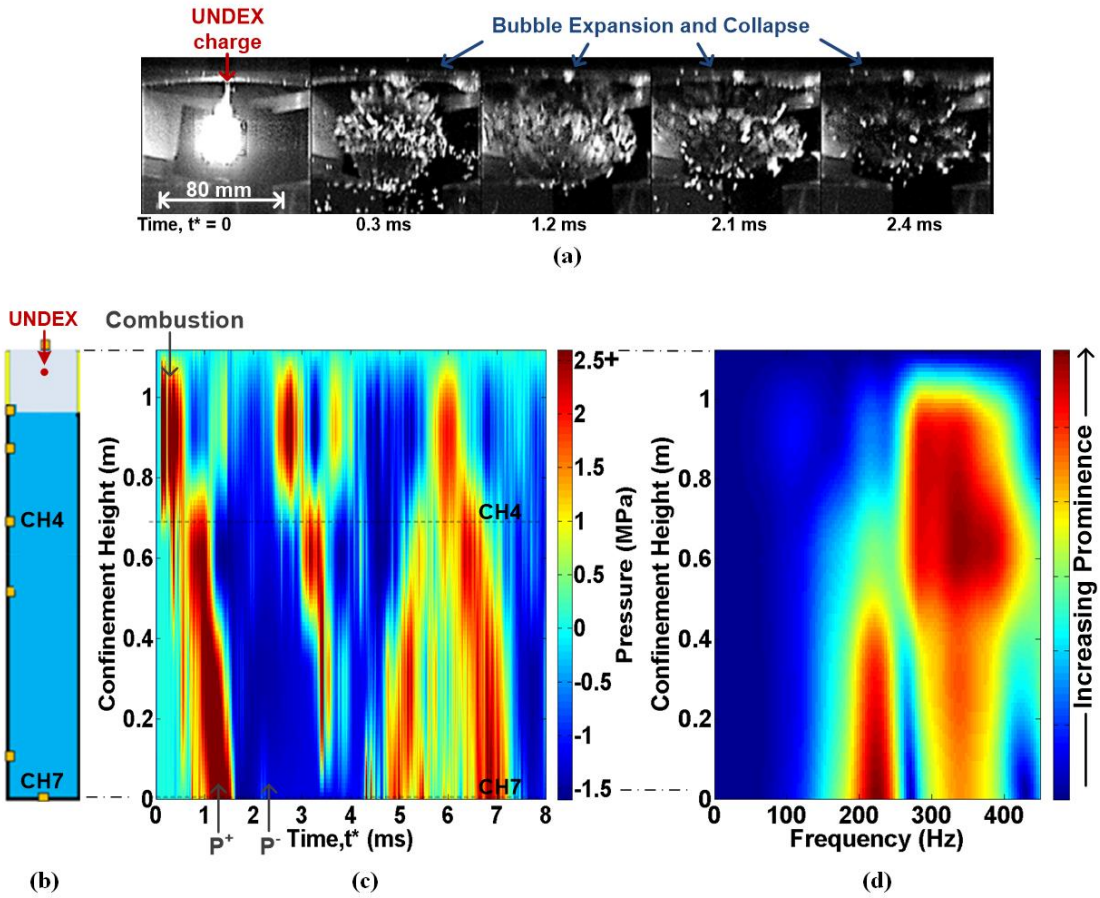

Figure 4.2 Bubble dynamics characterization. (a) First bubble cycle images; (b) confinement reconfiguration; (c) pressure history map; and (d) frequency map

The fluid wave speed inside the confining structure, c_f, can be estimated using Eq. (1) which is derived using piping mechanics and represents a weighted average between coupled pressure wave speeds in the aluminum section ($c_w \Big/ \sqrt{1+\frac{KD}{E_{al}h}}$) and the acrylic section ($c_w \Big/ \sqrt{1+\frac{KD}{E_{ac}h}}$) [22]. This averaging takes into account the acrylic window section from the confinement. The details of parameters used in Eq.(1) can be found in Table 4.2. Note that the water's wave speed was determined by the Newton–Laplace equation ($\sqrt{(K/\rho)}$); where K and ρ are the water's bulk modulus and density at room temperature (20˚C) respectively.

$$c_f = \left(\frac{L_{al}}{L_{ac}+L_{al}}\right)\frac{c_w}{\sqrt{1+\frac{KD}{E_{al}h}}} + \left(\frac{L_{ac}}{L_{ac}+L_{al}}\right)\frac{c_w}{\sqrt{1+\frac{KD}{E_{ac}h}}} \quad (1)$$

Table 4.2 Dimensions and properties of the confining structure

Parameter	Value
c_w (Wave speed in water)	1483 m/s
K (Bulk modulus of water)	2.2 GPa
h (Wall thickness of confining tube)	25.4 mm (1.00 in)
D (Diameter of confining tube)	177.8 mm (7.00 in)
E_{al} (Elastic modulus of aluminum)	69 GPa
E_{ac} (Elastic modulus of acrylic)	3.17 GPa
L_{al} (Length of aluminum section)	965 mm (38.00 in)
L_{ac} (Length of acrylic section)	152 mm (6.00 in)

From Eq. (1), c_f is found to be 1226 m/s. The frequency of pressure wave oscillation, f, in a confinement that is partially open to the environment can be obtained as a function of wave speed (c_f) and the total length of the confining tube, $L = L_{al} + L_{ac}$, using Eq. (2) [21, 22]. The water hammer frequency for an equivalent one-dimensional system from Eq. (2) is 274 Hz. This implies that the 225 Hz response in Figure 4.2 (d) is a hammer cycle likely caused due to the water flow during the bubble contraction phase as well as the high pressure waves from the bubble collapse.

$$f = \frac{c_f}{4L} \quad (2)$$

The frequency of the bubble expansion and collapse cycles can be obtained from the change in bubble diameter (see Figure 4.3 (a)). The bubble diameter expands and contracts in time in a cycloidal shape and loses energy between cycles; thus, each subsequent cycle is smaller in duration and size. Furthermore, Figure 4.3 (b) shows the pressure history at the closed end of the confinement. After the charge is ignited, the high-pressure from the explosive arrives at t* ~ 0.7 ms and the high-pressure from the

first bubble collapse arrives at t* ~ 4.1 ms. The plateau region between high-pressures are indicative of cavitation on the closed end's surface. Note that the first bubble collapsed around t* ~ 2.4 ms and the high-pressure from the bubble did not arrive at the closed end until t* ~ 4.1 ms; this means that the initial portion of the first bubble pulse arrived during cavitation and did not cause a pressure rise. Moreover, after t* ~ 9.0 ms, the fluctuations in pressures are relatively small in magnitude (but consistent in frequency as illustrated by the 225 Hz response in Figure 4.2 (d)).

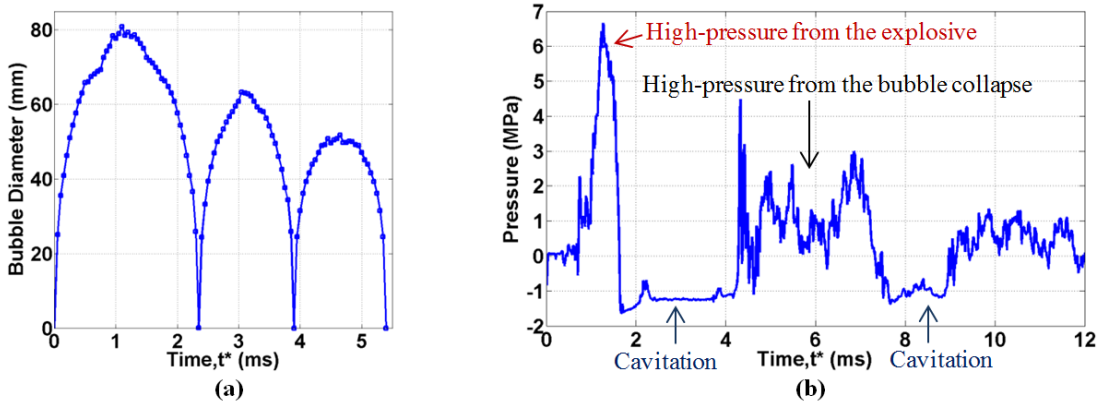

Figure 4.3 (a) Bubble diameter during the first three collapse cycles and (b) pressure history at the closed end of the confinement from CH7

3.2. Implodable Collapse Behavior

During hydrostatic implosions inside the confining structure water rushes from the open end towards the closed end as the specimen collapses. Soon after the specimen fully collapses, the rushing water impacts against the closed end causing immense pressure surge (hammer pressure wave). The pressure differential between the environment and confinement causes cyclic loading conditions inside the confinement [21]. The dynamic pressure history (where 0 MPa represents the hydrostatic collapse pressure) inside the confining structure is illustrated in Figure 4.4 (a) (where t =0 is the time of interest that represents initial specimen structural/wall contact).

UNDEX implosions have comparable pressure history maps to the charge characterization map in Figure 4.2 (c). After the charge combusts at t = -6 ms, high-pressure wave travels down the confining structure, followed by cavitation along the confinement walls which are shown in Figure 4.4 (b) as P^+ and P^- respectively. Moreover, as discussed earlier, the charge ignition causes various bubble cycles. Once the initial shock wave passes through the specimen, it vibrates in a mode-2 shape (seen through DIC analyses). When the high-pressure pulse from the first bubble reaches the bottom of the confinement, it reflects as a high-pressure wave (seen between -2 and 0 ms in Figure 4.4 (b)). These high pressures from the first bubble collapse supply sufficient energy to the specimen to make it unstable and collapse. The specimen collapse also emits a high-pressure wave that causes a hammer (shown in Figure 4.4 (b) as Hammer). After this hammer wave, the cyclic behavior (similar in magnitude of a hydrostatic implosion) can be seen at the bottom closed end of the confinement (CH7).

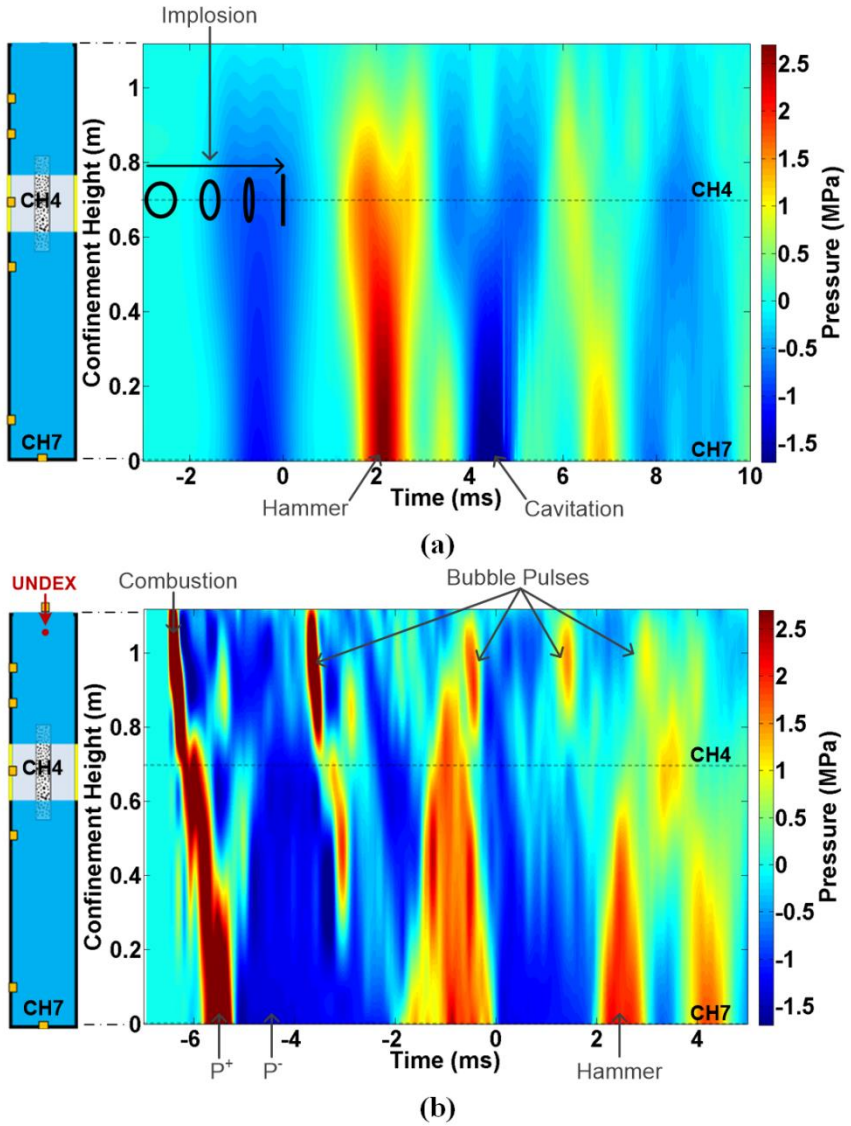

Figure 4.4 Pressure history diagram of the (a) hydrostatic and (b) UNDEX cases without polyurea coatings

Real-time deformation values from the specimen's surface can be obtained through the DIC analysis as shown in Figure 4.5. For the hydrostatic case, the implosion happens relatively smooth over time. For the UNDEX case, the specimen oscillates for about two cycles before instability. One of these oscillation cycles is illustrated in Figure 4.5 between -4.6 and -0.3 ms.

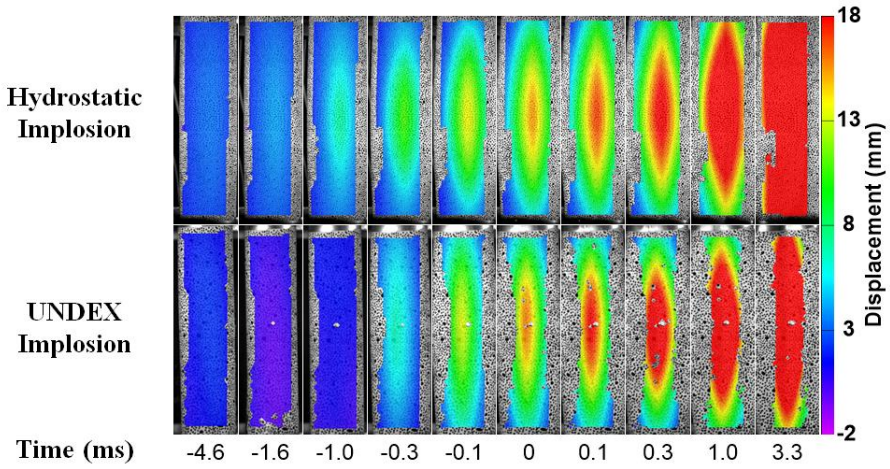

Figure 4.5 Full-field DIC displacement contours for the hydrostatic and UNDEX implosion cases without polyurea coatings

The collapse can be better visualized and compared if the center point (point of initial wall/structural contact at t =0) data is extracted and plotted versus time. Figure 4.6 (a) shows the center point velocity for the cases without polyurea coatings. During DIC correlation, there is transient cavitation along the inner surface of the confining structure due to the high pressures in the UNDEX case; this is represented by a gray box in Figure 4.6 (a). Within this cavitation period, the exact magnitudes of the velocity could be distorted due to changes in refractive index (which affects the camera's focus and magnification), but the velocity information during this time period can be viewed qualitatively.

The hydrostatic implosion starts at rest, and the specimen rushes into itself rapidly until it reaches 12 +/- 1 m/s and there a sufficient drop in surrounding pressure to decrease the collapse speed to 8 +/- 1 m/s, followed by wall contact at t =0 (see Figure 4.6 (a)). This two-phase velocity behavior is common in a confined hydrostatic initiated implosion [6]. The UNDEX implosion starts with cyclic movement caused by the UNDEX and bubble pressure waves. The high-pressure pulse from the first bubble

collapse of 2 MPa is seen at t =-2 ms in Figure 4.6 (b). As mentioned previously, this high pressure leads to an instability initiation in the specimen. The implosion happens while the specimen is experiencing the 2 MPa over-pressure, leading to the high collapse velocities of 26 +/- 1.5 m/s (see Figure 4.6 (a)). The subsequent bubble collapses are relatively small in magnitude and have little contributions (as seen at t* > 9 ms from Figure 4.3 (b)) at the closed end of the confinement; which is why the cyclic pressure behavior is similar at the closed end after 2 ms (shown in Figure 4.6 (b)).

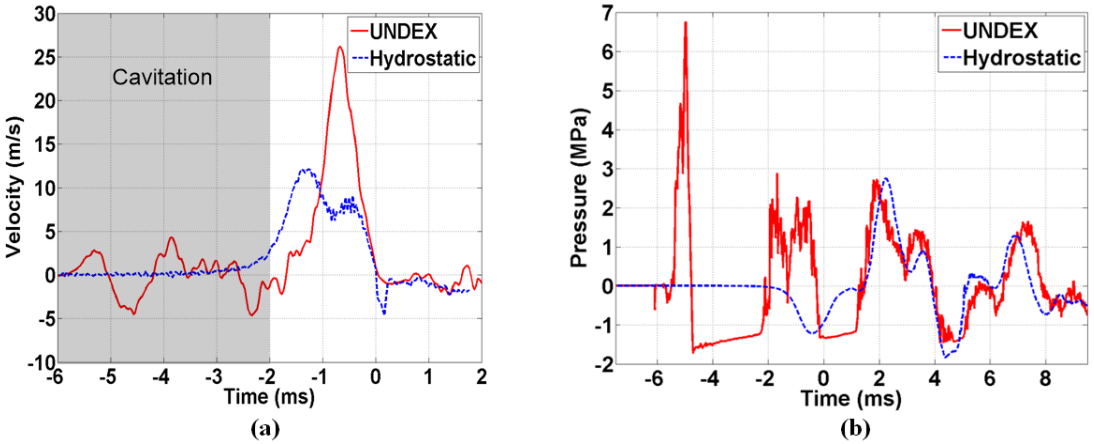

Figure 4.6 Comparison between the (a) center point velocities and (b) hammer pressures from CH7

There are three noticeable pulses seen in the UNDEX case from Figure 4.6 (b). The first is the pulse from the explosive itself (seen between -6 and -4 ms); the second is the bubble pulse (seen between -2 and 0 ms); and the third is the implosion pulse/hammer (seen between 1 and 4 ms). The areal impulse (defined as $\int_{t_i}^{t_f} Pdt$ and is regarded a good representation of the damage potential of an implosion [1]) of each of these three pulses are compared in Figure 4.7. This impulse is obtained by integrating the pressures from the beginning of each event. For comparison purposes, the low-

pressure cavitation/plateau regimes (seen between -5 and -2 ms as well as 0 and 1 ms in Figure 4.6 (b)) are not taken into account; resulting in the areal impulses from the high-pressures only.

The resultant high-pressure impulses from Figure 4.7 (a) can be used to illustrate the damage potential from each component of an UNDEX implosion. The explosive pulse, though it possesses a significantly high-pressure magnitude, it is short-lived, and it does not produce hammer since it has no volumetric displacement; leading to an impulse of 2110 +/- 36 Pa·s. The bubble collapse pulse has a comparable impulse to the explosive of 2030 +/- 61 Pa·s. The bubble expansion and collapse have transient and oscillating volumetric changes; hence it would not cause any significant hammer wave. The implosion event has the highest areal impulse at the closed end (3080 +/- 157 Pa·s) due to the implodable volumetric change that leads to a water hammer wave and the high-pressure pulses emitted by the implodable during collapse.

The impulse of the implosion hammer component from the UNDEX case is about 10% higher than the hydrostatic case as shown in Figure 4.7 (b). Since the initial implosion collapse in the UNDEX case happens during an over-pressure (leading to higher center point collapse velocities as mentioned earlier), it would be expected to emit higher pressures. However, longitudinal buckle propagation does not happen during the bubble over-pressure; hence the pressures emitted are not necessarily higher. In Figure 4.7 (b), it is shown that the impulse from the implosion of both the hydrostatic and UNDEX cases is comparable in both magnitude and duration. The small discrepancies seen in Figure 4.7 (b) are due to the ongoing bubble pulses, and differences in collapse pressure.

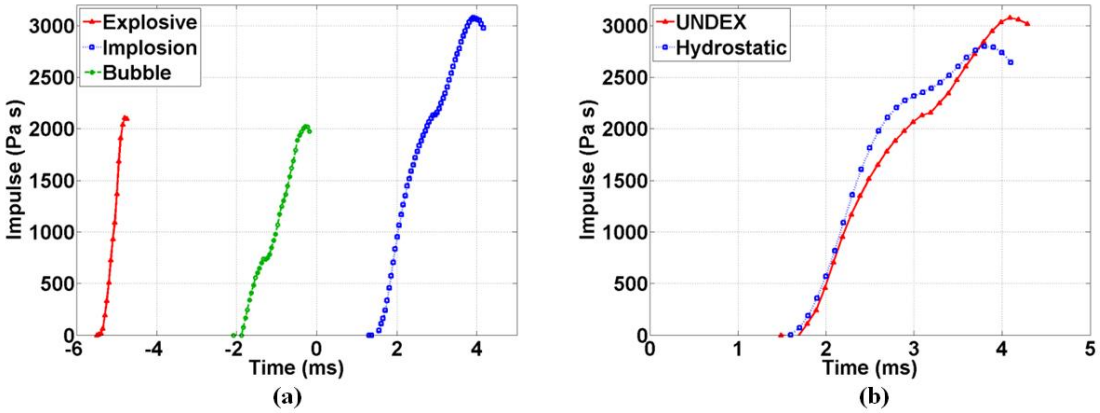

Figure 4.7 Impulses from hammer pressures (CH7) of (a) components from the UNDEX case and (b) areal impulse comparison of the implosion impulse from the UNDEX and Hydrostatic cases

3.3. Polyurea Coatings

For the hydrostatic initiated implosion experiments, the 1:1 volume ratio polyurea coating in the exterior (EC) and interior (IC) provided a small but notable changes in collapse mechanics when compared to the no coating (NC) case. For instance, the implosion process was seen to be prolonged. This is better illustrated by the center point velocity of the specimens as shown in Figure 4.8 (a). The initial rate of collapse is slower for the EC and IC cases which are due to the resistivity of the polyurea coating. For confining conditions, the symbiosis of collapse rate and surrounding pressure is exceptionally sensitive. From the decrease in collapse rate, the drop in surrounding pressure is also affected; leading to a sharper collapse soon after the implosion begins (seen between -2 and 0 ms in Figure 4.8 (a)). Figure 4.8 (b) and (c) illustrates the pressures near the specimen (about 70 mm away) and at the confinement's bottom closed end respectively. It is seen from these figures that pressures are comparable. The largest discrepancy is seen by the slight reduction in peak pressure from the closed end at 2 ms in Figure 4.8 (c). This small reduction is

likely due to a phase shift of the implosion pulse rather than energy mitigation through the coating. The pressures at the closed end are a combination of water hammer and implosion pulses [6]. Since the majority of the volumetric displacement happens before wall contact, and there are little changes in out-of-plane velocities between the three hydrostatic cases, then it is reasonable to assume that the low-pressure pulses, water particle velocity, and water hammer pulses are also about the same for these three cases. However, polyurea coatings have a strong delay effect in longitudinal buckle propagation [26]. This delay would also postpone the high-pressure pulses from the implosion as seen by the slight increase in pressure around 3 ms in Figure 4.8 (c).

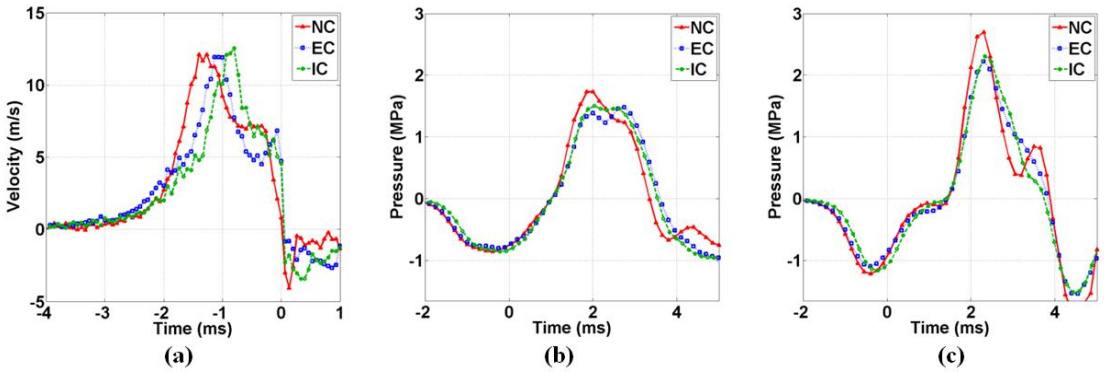

Figure 4.8 Hydrostatic implosion cases with polyurea coating showing (a) velocities, (b) sensor pressure from CH4, and (c) hammer pressure from CH7

For the UNDEX initiated implosion experiments, the 1:1 volume polyurea coating had a greater effect on the implosion mechanics when compared to the hydrostatic initiated experiments. First, the peak velocities at wall contact for both the EC and IC cases decrease by 5 +/- 0.5 m/s. Second, the oscillation cycle was extended; meaning that the implosion was delayed through polyurea coating (especially by the IC case). This reduction in velocity and delay is seen in Figure 4.9 (a); note that t =0 represent wall contact, also, the charge ignition happens at - 7 ms for the IC, -6 ms for the EC,

and -5.5 ms for the NC cases (illustrated by Figure 4.9 (b)). Finally, the peak pressure at the hammer end seems to be lower for both coated cases (shown in Figure 4.9 (c)); some of the higher frequencies from the shock could've been damped as the shock passed through the coated specimen. The implosion pressures seen after 0 ms are also reduced. Like for the hydrostatic case, the reduction in the implosion high-pressures is due to a phase shift in the implosion pulse rather than energy mitigation. The phase shifts in the UNDEX cases are more prominent than the ones from the hydrostatic cases. The initially higher collapse velocities and the strain rate sensitivity of the polyurea coatings are the cause for these stronger shifts. Note that for the IC case, the implosion and water hammer pulses are nearly separated between 1 and 4 ms in Figure 4.9 (c); this is indicative that the IC leads to a larger delay in buckle propagation, which leads to a stronger phase shift when compared to the EC case.

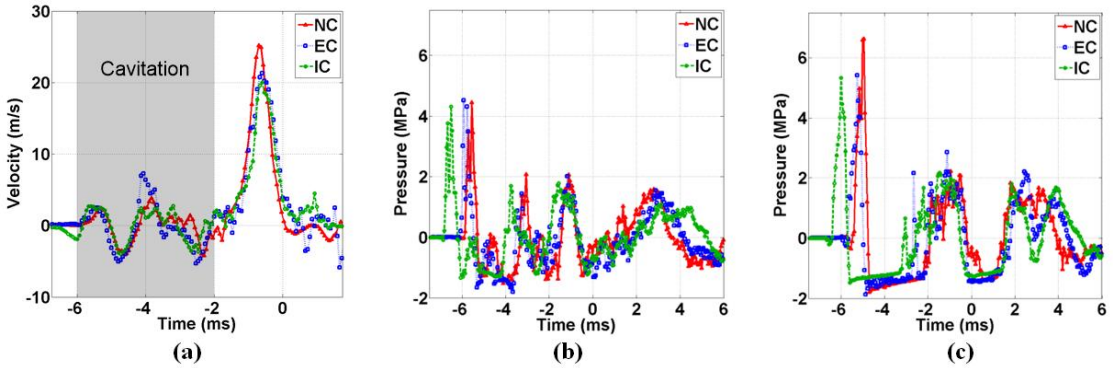

Figure 4.9 UNDEX implosion cases with polyurea coating showing (a) velocities, (b) sensor pressure from CH4, and (c) hammer pressure from CH7

3.4. Hammer Energy

The impulse is an excellent representation of the damage potential from a pressure pulse. Also, it can be directly related to the energy flux, E_F, of the pressure pulse [27, 29]. The energy flux at the confinement radius, R_c, up to time, t, is defined in Eq. (3).

Note that impulse is expressed in terms of a pressure integral, thus, it can be simplified into Eq. (4).

$$E_F = \frac{1}{2\rho_0 R_c}\left[\int_0^t p\,dt\right]^2 \tag{3}$$

$$E_F = \frac{I^2}{2\rho_0 R_c} \tag{4}$$

Where, p is the dynamic pressure, I is the areal impulse, and ρ_0 is the density of the fluid.

The implosion event generates an energy flux with a spherical surface area [26, 27]. Half of the spherical pulse will travel upwards and leave through the open end of the confinement. The second half will travel downwards, transition from half sphere to planar, reach the closed end of the confinement, and reflect upwards. Since the focus of this study is on the closed end, only the second half of the implosion pulse will be considered. To find the energy at the closed end, the energy flux (where p is taken from CH7) is multiplied by the confinement's cross sectional area ($2\pi R_c^2$). The energy at the closed end will be referred to as implosion energy, E_I; this is the energy required to cause the high pressure surge seen in CH7 for all experiments after t=0 ms.

Recall that the low-pressures and cavitation regimes after wall contact are not taken into account in the impulse calculations since discrepancies are only present during the high-pressure pulses. For this reason, the subsequent energy calculations also only pertain to the high-pressure pulses. Figure 4.10 (a) shows the impulse from the high-pressure waves as a function of time for all six cases. For the hydrostatic initiated cases, the phase shifts from the addition of polyurea led to a small decrease in impulse. For the UNDEX initiated cases, the phase shift was much larger in time, leading to more distinct reductions in impulse. Figure 4.10 (b) shows the energy as a

function of time calculated from the impulses to have a similar trend as the impulse curve. The results of Figure 4.10 are summarized in Table 4.3. The polyurea coating does not mitigate much of the available energy, but it does cause a phase shift so that the high-pressures from the water hammer does not align with the high pressures from the implosion; this effect is stronger during higher collapse velocities due to the high strain rate sensitivity of the polyurea. It seems plausible that at specific collapse velocities, the high-pressure implosion pulse could be aligned with the low-pressure hammer pulse, and cancel out most of the subsequent oscillatory behavior within the confinement; however, this feat would be beyond the scope of this study.

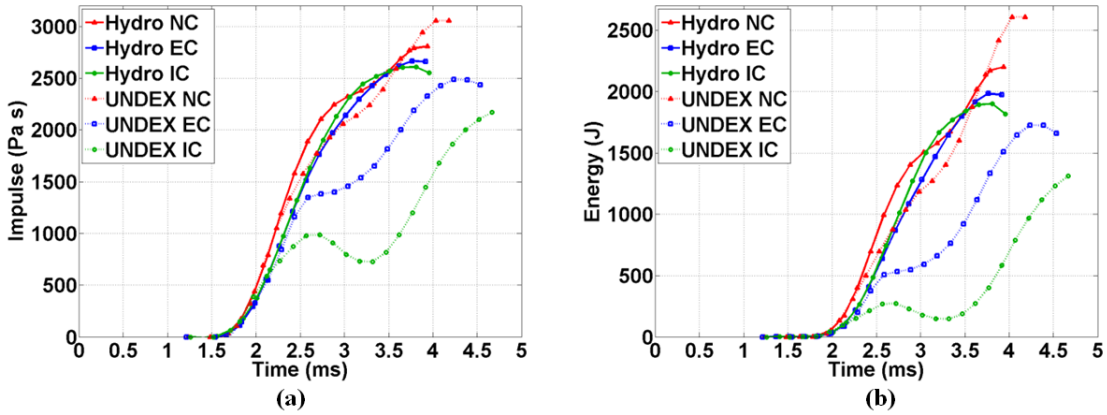

Figure 4.10 (a) Areal impulses and (b) energies from high-pressure waves for all experimental cases

Table 4.3 Peak impulse and energy measurements due to implosion's high pressure

Cases	I (kPa·s)	E_H (kJ)
Hydrostatic No Coating	2.81+/-0.14	2.21+/-0.31
Hydrostatic External Coating	2.67+/-0.05	1.99+/-0.11
Hydrostatic Internal Coating	2.61+/-0.16	1.91+/-0.33
UNDEX No Coating	3.07+/-0.12	2.64+/-0.29
UNDEX External Coating	2.49+/-0.08	1.73+/-0.16
UNDEX Internal Coating	2.18+/-0.09	1.34+/-0.16

3.5. Implosion Instabilities

Previous work on the collapse behavior of cylindrical shells shows that the quasi-static non-linear pressure-deformation curve of a cylindrical shell characteristically defines the change in structural stiffness in a buckling problem [30-31]. The maximum stiffness of a cylindrical shell is at zero hydrostatic pressure, but with increasing deformation and pressure in the pre-buckling regime, the stiffness of the structure is degraded to the point of instability. Beyond the instability point, the pressure needed to continue deformation decreases with increasing deformation indicating the presence of negative stiffness in the structure. This negative structural stiffness makes the structure more submissive to deformation [20].

From a non-linear buckling analysis using the Riks algorithm in ABAQUS, the pressure-deformation curve for the cylindrical shell used in this study can be generated. The ABAQUS model uses symmetry planes oriented at half of the length and half of the circumference of the shell (quarter symmetry model). Standard linear and non-linear properties for AL6061-T6 were used without any failure criteria. The critical pressure was applied to the outer surface of the shell, a shell-edge load was placed to account for the pressure at the end-caps, and the symmetry conditions were used on the two remaining planes. Imperfections were accounted for by introducing the collapse modes information from a buckling analysis of an identical model to the input file.

For results, nodal pressure and displacement values were extracted from the nodes at the deformed valley (R_{min}) and the lobe (R_{max}) of the length-wise mid-plane. The elliptical cross sectional area of the mid-plane ($\pi R_{max} R_{min}$) and the constant cross

sectional area at the end-cap locations has a linear transition between each other prior to collapse such that the volume (V) and the change in volume (dV) as hydrostatic pressure increases can be calculated. With the volume information and the nodal pressure values (P_N), the hydrostatic potential energy (E_H) can be found with Eq. (5). The change in volume of the fluid can be assumed to be the same as the collapsing cylindrical tube, thus the work done by the fluid during collapse (dw) can be expressed as Eq. (6).

$$E_H = VP_N \tag{5}$$

$$dw = dVP_N \tag{6}$$

An instability plot is shown in Figure 4.11 (a) where the left vertical axis is the normalized critical pressure in percentage, the right vertical axis is the potential hydrostatic energy, and the horizontal axis is the change in volume of the specimen. At nearly 1% volume change (dV), the pressure is 100% of the critical pressure (P_{cr}), which indicates hydrostatic instability and the natural collapse of the structure. Everything to the left of the maximum in the instability plot is stable, and everything to the right is unstable at 100% P_{cr}. As pressure drops from critical, then this instability threshold shifts from a maximum at 100% P_{cr} to a value that coincides with the hydrostatic pressure. To collapse a structure from 70% P_{cr}, there needs to be sufficient energy to deform the structure to 3.7% dV which is the unstable threshold for the 70% P_{cr} (from point A to point B in Figure 4.11 (a)).

The strain energy for thin cylindrical shells (U) during changing cylindrical volume can be estimated using Eq. (7) and Eq. (8) [32]. Figure 4.11(b) illustrates the coordinate system used in Eq. (7) and (8). After Eq. (8) is substituted into Eq. (7) and

integrated with respect to the radial direction, r from a-h/2 to a+h/2 (inside and outside radius respectively) the strain energy can be obtained in terms of displacements. As mentioned, the radial deformation, w, starts as an elliptical cross-sectional area of the mid-plane and transitions linearly to zero at both end-cap locations. Longitudinal deformation, u, and tangential deformation, v, are assumed to be negligible as well as any strain energy at the end-cap locations due to small changes in curvature. Note that these assumptions and Eq. (7) are only suitable for small deformations where non-linear effects are not present; in turn, this method cannot be used to estimate required strain energies for very low pre-pressures.

$$U = \frac{E}{2(1-\nu^2)} \iiint \left[\varepsilon_z^2 + \varepsilon_\theta^2 + \frac{1-\nu}{2}\gamma_{\theta z}^2 + 2\nu\varepsilon_z\varepsilon_\theta\right] drdzrd\theta \tag{7}$$

$$\varepsilon_z = \frac{\partial u}{\partial z} + (r-a)\frac{\partial^2 w}{\partial z^2} \tag{8a}$$

$$\varepsilon_z = \frac{1}{a}\frac{\partial v}{\partial \theta} + \frac{r-a}{r\,a}\frac{\partial^2 w}{\partial r^2} - \frac{w}{r} \tag{8b}$$

$$\gamma_{\theta z} = \frac{1}{r}\frac{\partial u}{\partial \theta} + \frac{r}{a}\frac{\partial v}{\partial z} + \frac{\partial^2 w}{\partial \theta\,\partial z}\left(\frac{r-a}{a} + \frac{r-a}{r}\right) \tag{8c}$$

Where the parameters represent: Young's modulus, E; Poisson's ration, ν; mean radius, a; shell thickness, h; longitudinal displacement, u; tangential displacement, v; and radial displacement, w.

The energy requirement for dynamic instability (E_{ins}) is calculated as the energy required to achieve the strain energy at a given deformation and the energy needed to displace the fluid as shown in Eq. (9) and illustrated by Figure 4.11 (b); where the vertical axis is the strain energy of the cylindrical structure plus the work done by the moving fluid, and the horizontal axis is the change in volume of the specimen. For instance, at 70% pre-collapse pressure (1.06 MPa in this case), an additional 305 J is

required to cause the cylindrical specimen to volumetrically deform from 0.05% (the dV at 70%P_{cr}) to 3.7%, which will lead to instability.

$$E_{ins} = U + dw \tag{9}$$

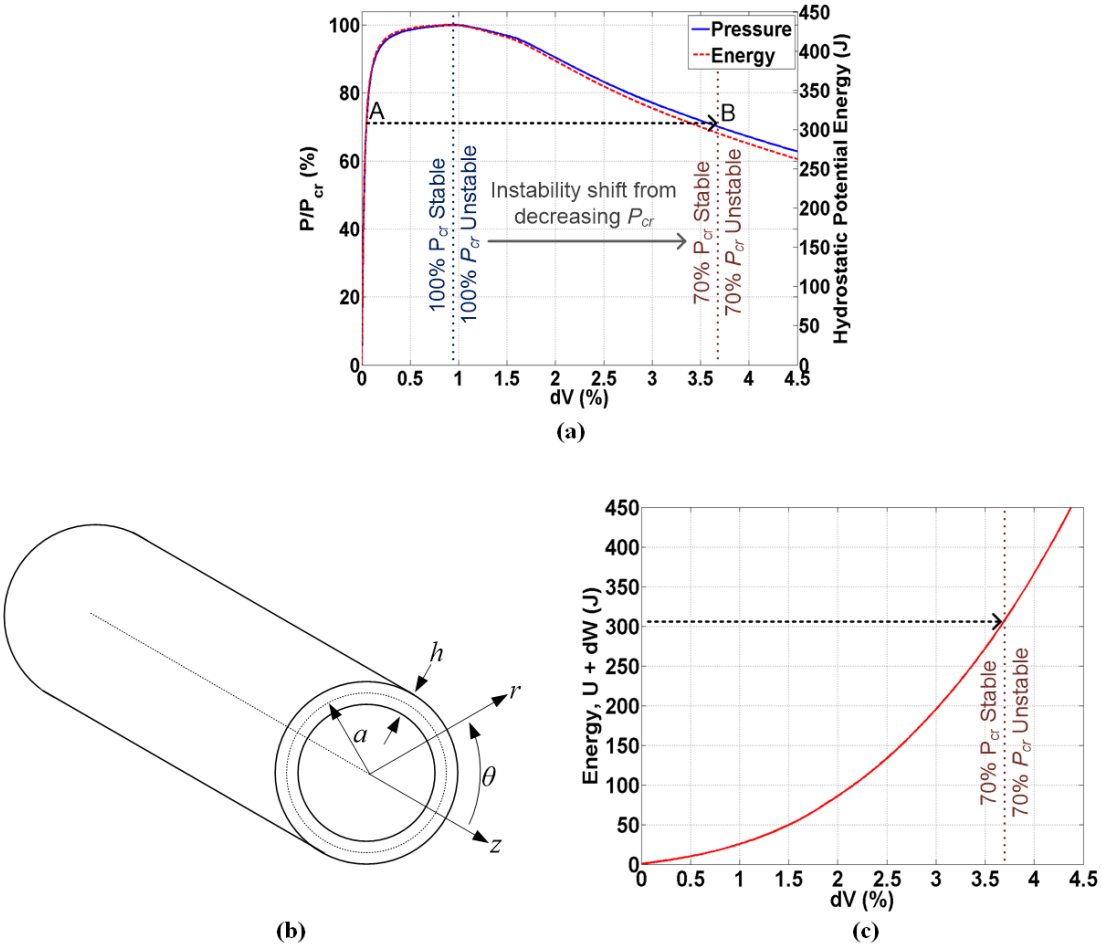

Figure 4.11 (a) ABAQUS non-linear Riks results for the hydrostatic instability of the specimen, (b) coordinate system for cylindrical shell, and (b) estimated energy requirements for instability

The impulse delivered to the specimen by the RP-80 charge can be found by using the pressure information at the charge location (Figure 4.9 (b)) and integrating it with respect to time. The maximum areal impulse at the specimen location is ~1241 Pa·s for all cases. From the impulse, and Eq. (4), the maximum energy flux passing through the specimen due to the UNDEX charge is 8,565 J/m^2 and the energy can be found as

261 J by using the surface area of the specimen. This energy is below the required 305 J for specimen instability. For this reason the specimen oscillates in a stable manner after the initial pressure from the explosive. However, the additional energy supplied by the first bubble collapse is enough to push the specimen to the unstable regime for the 70% hydrostatic pressure as shown in previous sections.

4. Conclusions

An experimental investigation is conducted to understand the behavior of confined implosions subjected to UNDEX loading. Both pressure measurements along with high-speed DIC measurements are carried out to correlate the structural deformation with pressure history. The key findings of this study are as follows:

- The bubble from an explosive will lead to particle movement in a confinement during its contraction phase that can cause a water hammer. However, this hammer wave though prominent in the frequency, is relatively small in magnitude with respect to the magnitude of the pressure waves from the bubble collapse and the explosive charge.
- The implosion pressure pulse of a confined implosion that is hydrostatic and UNDEX initiated are relatively similar, at the closed end, after the wall contact phase.
- The surface center-point velocity from an implosion specimen does not have a two-phase region in cases where the surrounding pressure is much higher than the critical collapse pressure, such as the UNDEX cases in this study (shown in Figure 4.6 (a)).

- The high-pressure's impulse from the first bubble collapse and implosion, in the UNDEX case, is about the same and ~50% higher respectively than the impulse from the explosive itself. This illustrates that volumetric changes within a confinement can be more detrimental than explosives (under the parameters of this study) due to the water hammer effect.
- An UNDEX implosion has two oscillatory components (the bubble collapse pulses and the periodic oscillation within the confinement) that are combined. These superpositioned pulses will lead to either extremely high pressures, or it could also negate each other depending on their respective phase.
- Polyurea coating the specimens does not necessarily help reduce pressure surges within the parameters of this study. However, the coating does cause phase shifts which delays the implosion pulse. The polyurea coating thickness can be used to control the delay period (since coating thickness affects buckle propagation velocity [26]).
- Through polyurea coating, a delay in implosion and lower collapse/buckle velocities can be achieved, which helps reduce the peak implosion pressures by decoupling the water hammer wave and the implosion high-pressures. For the UNDEX cases, where collapse velocities reached greater values, the polyurea coating has a greater delay effect in collapse mechanics due to the strain rate sensitivity of the polyurea when compared to the hydrostatic cases.
- The energy from the high-pressure waves found at the closed end of the confinement is nearly the same for the hydrostatic case, since the polyurea coating did little to mitigate and delay the implosion pulse (due to the lower collapse

velocities). However, for the UNDEX initiated cases, polyurea coating caused a longer delay in the implosion pulse which was sufficiently large to reduce the peak energy values by ~35% for external coatings and ~50% for internal coatings.

- A Riks non-linear model can be used to estimate the required energy needed to push a pre-pressurized cylindrical structure into the unstable mode. The structure in this study was found to need an additional 277 J to become unstable at 70% pre-pressure. The explosive used did not supply sufficient energy for instability. However, the bubble collapse and confining nature of the problem led to additional energy inputs that caused the implosion instability.

Acknowledgements

The authors kindly acknowledge the financial support provided by Dr. Thomas Fu under the Office of Naval Research (ONR) Grant No. N00014-15-1-2046.

References

[1] Turner, S. E. (2007). Underwater implosion of glass spheres. The Journal of the Acoustical Society of America, 121(2), 844. doi:10.1121/1.2404921

[2] Turner, S. E., & Ambrico, J. M. (2012). Underwater Implosion of Cylindrical Metal Tubes. Journal of Applied Mechanics, 80(1), 011013. doi:10.1115/1.4006944

[3] Urick, R. J. (1963). Implosions as Sources of Underwater Sound. The Journal of the Acoustical Society of America, 35(11), 1903. doi:10.1121/1.2142767

[4] Vath, F. (1968). Development of buoyancy material for the deep submergence search vehicle. Evaluation of sympathetic implosion of buoyancy modules. Defense Technical Information Center. Naval Applied Science Laboratory, Brooklyn, New York

[5] Orr, M., & Schoenberg, M. (1976). Acoustic signatures from deep water implosions of spherical cavities. The Journal of the Acoustical Society of America, 59(5), 1155. doi:10.1121/1.380977

[6] Gupta, S., Matos, H., Shukla, A., & Leblanc, J. M. (2016). Pressure signature and evaluation of hammer pulses during underwater implosion in confining environments. The Journal of the Acoustical Society of America J. Acoust. Soc. Am., 140(2), 1012-1022. doi:10.1121/1.4960591

[7] Gupta S, LeBlanc JM, Shukla A (2015) Sympathetic underwater implosion in a confining environment. Extreme Mech Lett 3:123–129. doi: 10.1016/j.eml.2015.03.007

[8] Costa, L., & Turner, S. (2008). Implosion Testing within a Small-Scale Torpedo Tube. NAVSEA NUWC-NPT Technical Memo 08-014.

[9] Accident Grounds Neutrino Lab. (2001). Retrieved January 13, 2016, from http://physicsworld.com/cws/article/news/2001/nov/15/accident-grounds-neutrino-lab

[10] R.I.P. A.B.E. (2010). Retrieved January 13, 2016, from http://www.whoi.edu/oceanus/feature/rip-abe

[11] Robotic Deep-sea Vehicle Lost on Dive to 6-Mile Depth. (2014). Retrieved January 13, 2016, from http://www.whoi.edu/news-release/Nereus-Lost

[12] Farhat, C., Wang, K., Main, A., Kyriakides, S., Lee, L., Ravi-Chandar, K., & Belytschko, T. (2013). Dynamic implosion of underwater cylindrical shells: Experiments and Computations. International Journal of Solids and Structures, 50(19), 2943-2961. doi:10.1016/j.ijsolstr.2013.05.006

[13] Ikeda, C. M., Wilkerling, J., & Duncan, J. H. (2013). The implosion of cylindrical shell structures in a high-pressure water environment. Proceedings of the Royal Society A: Mathematical, Physical and Engineering Sciences, 469(2160), 20130443-20130443. doi:10.1098/rspa.2013.0443

[14] Gish, L., & Wierzbicki, T. (2015). Estimation of the underwater implosion pulse from cylindrical metal shells. International Journal of Impact Engineering, 77, 166-175. doi:10.1016/j.ijimpeng.2014.11.018

[15] Gupta, S., Parameswaran, V., Sutton, M. A., & Shukla, A. (2014). Study of dynamic underwater implosion mechanics using digital image correlation. Proceedings of the Royal Society A: Mathematical, Physical and Engineering Sciences, 470(2172), 20140576-20140576. doi:10.1098/rspa.2014.0576

[16] Pinto, M., Gupta, S., & Shukla, A. (2015). Study of implosion of carbon/epoxy composite hollow cylinders using 3-D Digital Image Correlation. Composite Structures, 119, 272-286. doi:10.1016/j.compstruct.2014.08.040

[17] Pinto, M., Gupta, S., & Shukla, A. (2015). Hydrostatic Implosion of GFRP Composite Tubes Studied by Digital Image Correlation. Journal of Pressure Vessel Technology, 137(5), 051302-051302.

[18] Gupta, S., LeBlanc, J., & Shukla, A., (2014) Mechanics of the implosion of cylindrical shells in a confining tube. Int J Solids Struct 51:3996–4014. doi: 10.1016/j.ijsolstr.2014.07.022

[19] Gupta, S., LeBlanc, J., & Shukla, A., (2015) Implosion of longitudinally off-centered cylindrical volumes in a confining environment. J Appl Mech 82:051001. doi: 10.1115/1.4029917

[20] Gupta, S., Matos, H., Leblanc, J. M., & Shukla, A. (2016). Shock initiated instabilities in underwater cylindrical structures. Journal of the Mechanics and Physics of Solids, 95, 188-212. doi:10.1016/j.jmps.2016.05.034

[21] Ghidaoui, M. S., Zhao, M., Mcinnis, D. A., & Axworthy, D. H. (2005). A Review of Water Hammer Theory and Practice. Applied Mechanics Reviews Appl. Mech. Rev., 58(1), 49. doi:10.1115/1.1828050

[22] Tijsseling, A. (2007). Water hammer with fluid–structure interaction in thick-walled pipes. Computers & Structures, 85(11-14), 844-851. doi:10.1016/j.compstruc.2007.01.008

[23] Keramat, A., Tijsseling, A., Hou, Q., & Ahmadi, A. (2012). Fluid–structure interaction with pipe-wall viscoelasticity during water hammer. Journal of Fluids and Structures, 28, 434-455. doi:10.1016/j.jfluidstructs.2011.11.001

[24] Meniconi, S., Brunone, B., & Ferrante, M. (2012). Water-hammer pressure waves interaction at cross-section changes in series in viscoelastic pipes. Journal of Fluids and Structures, 33, 44-58. doi:10.1016/j.jfluidstructs.2012.05.007

[25] J. LeBlanc, J. Ambrico, and S. Turner, “Underwater implosion mechanics: Experimental and computational overview,” in Blast Mitigation - Experimental

and Numerical Studies, edited by A. Shukla, Y. Rajapakse, and M. Hynes (Springer, New York, 2014). doi: 10.1007/978-1-4614-7267-4_6

[26] Matos, H., & Shukla, A. (Submitted 2016). Mitigation of Implosion Energy from Aluminum Structures. International Journal of Solid Structures.

[27] Pinto, M., Matos, H., Gupta, S., & Shukla, A. (2016). Experimental Investigation on Underwater Buckling of Thin-Walled Composite and Metallic Structures. Journal of Pressure Vessel Technology, 138(6), 060901. doi:10.1115/1.4032703

[28] Apazidis, N. (2016). Numerical investigation of shock induced bubble collapse in water. Physics of Fluids, 28(4), 046101. doi:10.1063/1.4944903

[29] Cole, R. (1948). Underwater Explosions. Princeton: Princeton Univ. Press.

[30] Hutchinson, J. W., and Koiter, W. T., (1970). Postbuckling Theory. Appl. Mech. Rev. 23(12), 1353-1366

[31] Kyriakides, S., & Babcock, C. (1981). Large deflection collapse analysis of an inelastic inextensional ring under external pressure. International Journal of Solids and Structures, 17(10), 981-993. doi:10.1016/0020-7683(81)90036-6

[32] Flügge, W. (1962). Statik und Dynamik der Schalen [Statics and dynamics of shells]. Berlin: Springer.

CHAPTER 5. Mitigation of Implosion-Induced Water Hammer Waves

by

Helio Matos and Arun Shukla

Dynamic Photo Mechanics Laboratory, Department of Mechanical, Industrial and Systems Engineering, University of Rhode Island, Kingston, RI 02881

In preparation for publication

Abstract

Generation of high-pressure water hammer waves along with the cavitation at the closed end in the open-ended tube implosion poses a significant risk to the hull safety. This study addresses the generation of water hammer waves from implosions and evaluates different solutions for mitigating the hammer waves. Specifically, four types of mitigation methods were selected and analyzed in this study aimed to reduce the degree of cavitation at the closed end while simultaneously reducing the damage potential caused by the water hammer wave. The four mitigation methods are: (1) a baffle system; (2) a granular polypropylene spheres technique; (3) a high-density foam method; and (4) a piston system. Two high-speed cameras are used to capture the imploding structures while various dynamic pressure transducers measure the emitted pressure pulses. The specimens are confined inside a thick-walled cylindrical structure that had one end open to the hydrostatic pressure inside the pressure vessel and the other end closed. This confinement configuration generates a water hammer at the closed end of the confinement. The results of these experiments show that optimized high-density foam can drastically mitigate the pressure within the confining tube

1. Introduction

In this study, an experimental investigation is conducted to evaluate different pressure mitigation techniques for implosion induced water hammer waves. This research arises from the concern of damage to naval and marine structures such as underwater pipelines, submarines, and autonomous underwater vehicles (AUVs). When these structures are submerged deep underwater and experience high

hydrostatic pressures, they can become unstable, collapse inward, and release powerful propagating shock waves in a process known as implosion [1-5]. In a confining environment, the implosion's pressure waves and any induced particle velocity can interact with its surroundings leading to water hammer waves that are stronger, and more destructive, than the implosion's pressure waves. Previous work shows the water hammer pressures reaching values of 150-200% the implosion's peak pressures [6-9].

Implosion has been of interest to the marine community since the mid-1900s [3-5]. However, one key accident that renewed the interest in this topic was the 2001 Super-Kamiokande laboratory accident in Japan where one photomultiplier tube imploded, and the pressure pulses from this implosion caused adjacent tubes to implode; leading to a chain reaction that destroyed 7000 photomultiplier tubes [10]. More recently in 2010, an AUV known as ABE was lost off the coast of Chile due to the glass sphere (that is used to control buoyancy) imploding; which created high-pressure pulses that destroyed all onboard systems [11]. Also, in 2014 the multi-million dollar AUV, Nereus, imploded off the coast of New Zealand [12]. These recent events highlight implosion as an ongoing issue.

The current work available on implosion characterizes the collapse mechanics for free-field environments [13-18]; meaning that the pressure pulses emitted during the implosion travel undisturbed. There is very limited work available on implosions within confining environments. These include implosions within a fully confined environment [19-21]; where it was shown that the limited hydrostatic pressure drastically affects the implosion process. Also, the implosions within a confining

environment that are open to a larger water body (held at the same hydrostatic pressure) leads to water hammers [6-9]. Water hammer and its mitigation is a well-established phenomenon in terms of piping mechanics [22-27]. However, there are no studies performed on water hammer mitigation techniques in large-scale naval structures.

Generation of powerful water hammer waves along with the cavitation at the closed end in the open-ended tube implosion poses a significant risk to the hull safety. This study addresses the generation of water hammer waves and evaluates different solutions for mitigating hammer waves. Specifically, four types of mitigation methods were selected and analyzed in this study aimed to reduce the degree of cavitation at the closed end while simultaneously reducing the damage potential caused by the water hammer wave. The four mitigation methods are: (1) a baffle system; (2) a granular polypropylene spheres technique; (3) a high-density foam method; and (4) a piston system. Digital Image Correlation (DIC) technique is used to capture real-time high-speed deformation for understanding fluid-structure interaction during implosion-induced water hammer.

2. Experimental Procedures

2.1. Specimen Geometry and Testing Facility

The implosion experiments are performed by using an 813 mm (32.0 in) long, thick walled (1 in), cylindrical confinement that is placed inside a 2.1 m diameter semi-spherical pressure tank as shown in Figure 1 (a) and (b). The confinement is made of two modular pieces; (1) an upper aluminum section that is 356 mm (14.0 in)

in length and has the top open to the pressure vessel's environment; (2) a lower optically clear acrylic section that is 457 mm (18.0 in) in length and is used to view the closed bottom end of the confinement as well as the implodable specimen (see Figure 1 (b)). Both sections of the confinement have 178 mm (7.0 in) inner diameter and are concentrically to one another. Six dynamic pressure sensors (PCB 138A05 from PCB Piezotronics Inc., Depew, NY) are used to obtain pressure data at 2 mega samples per second and are located along the walls of the confinement. Moreover, two high-speed cameras (Photron SA1 from Photron USA, Inc.) outside the vessel are used to capture high-speed images at 40,000 frames per second which are later analyzed through Digital Image Correlation (DIC). Additionally, the photographs from the high-speed cameras are captured through the optically clear windows located along the midspan of the vessel, and the lower acrylic section of the confinement as shown in Figure 1.

The implodable specimens are made from aluminum 6061-T6 tubes with a 38.1 mm (1.5 in) outer diameter (D), 0.89 mm (0.035 in) wall thickness (t). Two different unsupported lengths (L) were used in this study; 254 and 203 mm (10.0 and 8.0 in respectively). The specimens are coated with a thin high-contrast speckle pattern then sealed using two aluminum end caps with o-ring seals and placed concentric to the confining tubular structure as shown in Figure 1 (c). The end caps prevent water penetration in the specimen; therefore during the experiments, high-pressure water surrounds the specimen while low-pressure air resides inside. To perform the experiments, the pressure vessel is filled with water and then slowly pressurized with

compressed nitrogen gas until the specimen implodes under hydrostatic pressure (at 2.22 and 2.79 MPa for the 254 and 203 mm long implodables respectively).

Four types of mitigation methods were selected and evaluated in this study as shown in Figure 1 (d). The first method is a baffle system consisting of a 50% blockage ratio baffle. The second technique is granular polypropylene spheres, where 12.7 mm (0.5 in) diameter spheres are stacked in 4 layers (148 spheres per layer). The third approach is by using cylindrical-shaped high-density foams (PVC 130 from Gurit Inc., Bristol, RI). The fourth scheme is using the same high-density foam from the third approach, but with a rod through its center and a smaller diameter such that when the confinement is filled with water, the foam floats and can act as a piston. All four mitigation techniques were placed at the bottom closed-end of the confinement and given a physical restriction of 50.8 mm (2 in) height (or travel distance for the piston case) so that one technique does not outperform the other simply due to its size. More details on each method are listed in Table 5.1.

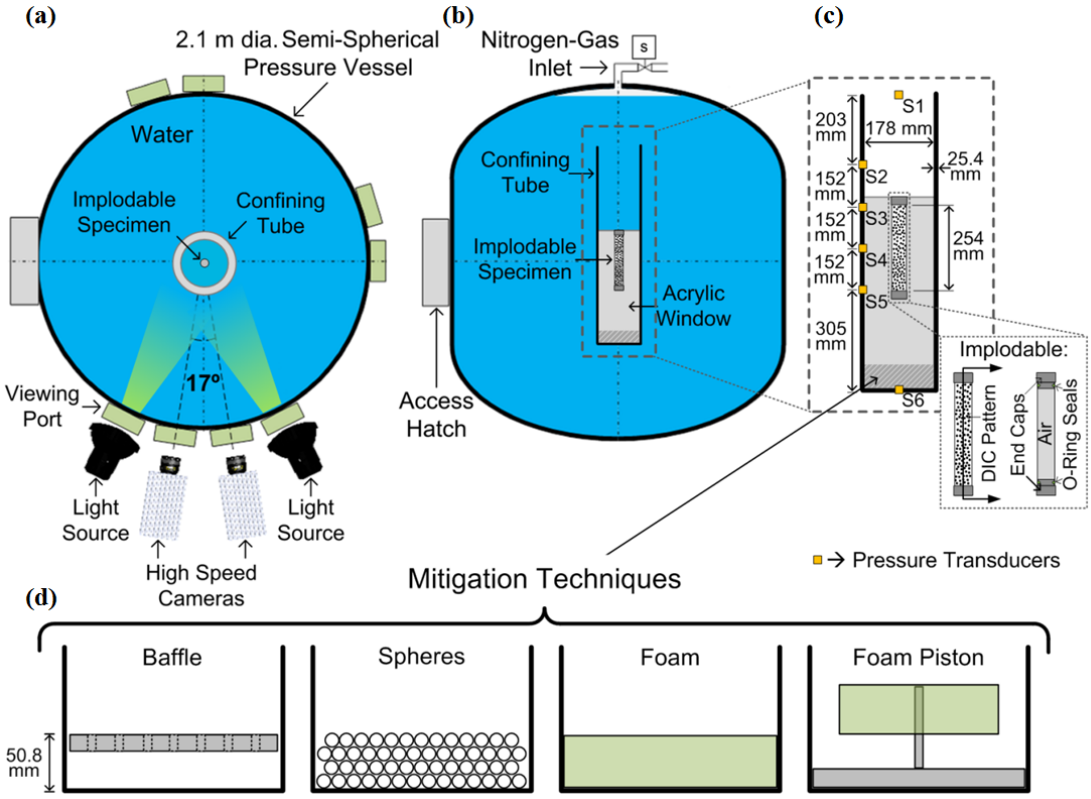

Figure 5.1 Experimental setup viewed from the (a) top, (b) front, (c) detailed confinement, and (d) the different mitigation methods

Table 5.1 Experimental series details

Cases	Mitigation Method	Description	Implodable Dimensions, L/D/t (mm)	Collapse Pressure (MPa)
C1	None	Used as a control case	254 / 38.1 / 0.89	2.22 +/- 0.02
B1	Baffle	AL baffle with 50% blockage ratio		
S1	Spheres	592 Polypropylene spheres of 12.7 mm dia. Stacked in 4 layers		
F1	Foam	503.8 mm thick1 178 mm dia., PVC130 high-density foam		
F2	Foam	503.8 mm thick1 178 mm dia., PVC130 high density foam	203 / 38.1 / 0.89	2.79 +/- 0.04
P1	Foam Piston	503.8 mm thick1 127 mm dia., PVC130 high density foam	254 / 38.1 / 0.89	2.22 +/- 0.02
P2	Foam Piston	503.8 mm thick1 102 mm dia., PVC130 high-density foam		
P3	Foam Piston	503.8 mm thick1 127 mm dia., PVC130 high density foam	203 / 38.1 / 0.89	2.79 +/- 0.04

The high-speed images are analyzed using commercially available DIC software (VIC3D 7 from Correlated Solutions, Inc., Columbia, SC) to measure full-field displacements across the viewable surface of the specimen. Previous work [6, 16] outlines the calibration procedures that validate the accuracy of the DIC results in the marine environment (where changes in refractive index are present). It was found that the flat-surface windows (located at the midspan of the pressure vessel) need to be perpendicular to the viewing axis [16], and the cylindrical window (from the confining structure) needs to be concentric to where viewing axis of both cameras meets (optical center) to minimize DIC displacement errors [6]. For this study, the in-plane displacement errors are ~2%, and the out-of-plane errors are ~5%.

3. Results and Discussion

3.1. Pressure Behavior

The pressure history for the four different types of mitigation techniques is compared to the no mitigation, control case (C1), in Figure 2 (a). It is seen that both the baffles (B1) and spheres (S1) techniques did not affect the magnitude or frequency of the pressure significantly. However, the high-density foam (F1) and foam-piston (P1) had a substantial effect on the frequency and well as the pressure magnitude. To further explore the impact from the high-density foam, the strain energy storage of the foam was optimized by increasing the collapse pressure of the implodable (by decreasing the length of the implodable) as seen by foam F2 in Figure 2 (b). Two additional piston cases were also explored to see the impact of piston diameter (P2) and foam behavior (P3).

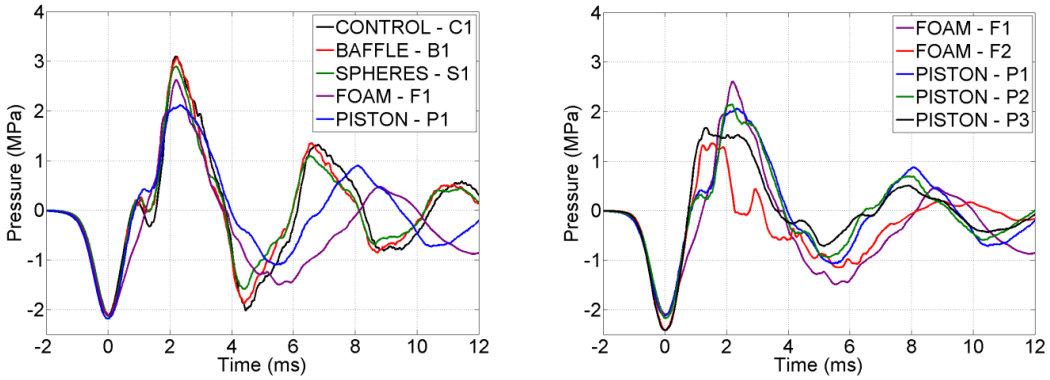

(a) **(b)**

Figure 5.2 Pressure history for (a) cases where Pcr= 2.22 MPa and (b) the foam and piston cases

The quasistatic compressive properties of the PVC130 foam were obtained by using an Instron 5585 and following ASTM Standards D3574 [28]. The dynamic properties were also achieved with an Instron 9210 drop weight tower (using an 8 kg weight and a 5 m/s impact velocity). All strains data were measured with 2-D DIC from images captured by a Prosilica camera (model GC2450 from Allied Vision Technologies GmbH). The quasistatic and dynamic true stress versus true strain behavior of the PVC 130 foam is plotted in Figure 3 (a) (average from six experiments). The strain rate sensitivity of the foam is illustrated by its 1.3 MPa increase of crushing strength (yield).

The foam behavior was optimized by having the collapse pressure (P_{cr} = 2.79 MPa) to be slightly lower than the foam's quasistatic crushing pressure (P = 2.85 MPa) as shown in Figure 3 (a). After the implodable goes unstable and the event becomes dynamic, the pressure must still rise until the dynamic crushing strength is reached and the foam fails in the flow region. For this reason, the pressures of the F2

and P3 cases still rises until the foam crushes in the flow region as shown in Figure 3 (b) by the overpressure of 1.3-1.5 MPa.

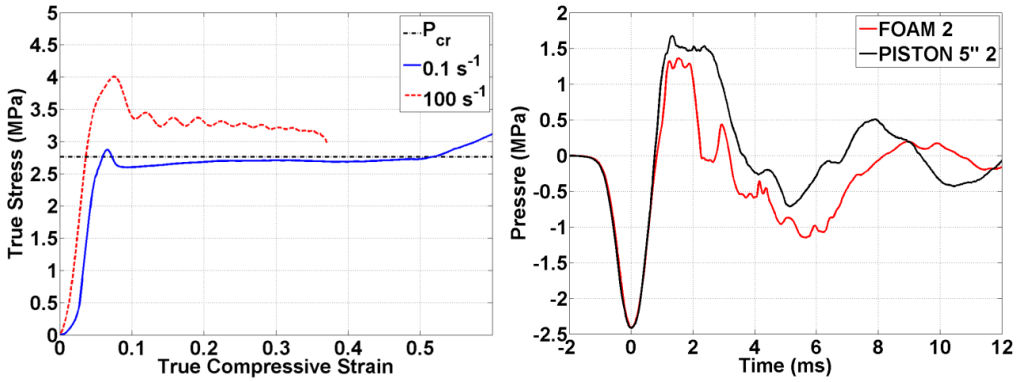

Figure 5.3 (a) PVC130 high-density foam Stress and strain properties under quasistatic and dynamic loading rates, and (b) pressure history for the Pcr = 2.79 MPa foam and piston cases

3.2. Frequency Response

The coupled pressure wave speed in a pipe, c_f, can be calculated by Eq. (1) [6, 9]. Eq. (1) represents a weighted average between wave speed in the aluminum tubular section ($c_w \Big/ \sqrt{1+\frac{KD}{E_{al}h}}$) and the acrylic tubular section ($c_w \Big/ \sqrt{1+\frac{KD}{E_{ac}h}}$) [6, 9]. The details for the parameters used in Eq. (1) can be found in Table 5.2. From Eq. (1), c_f is determined to be 931 m/s (952 m/s with a 50.8 mm (2 in) mitigation structure at the bottom closed end). Furthermore, the frequency of pressure wave oscillation, f, in a confining open tube that is partially open to larger water source is a function of wave speed (c_f) and the total length of the confining tube, $L = L_{al} + L_{ac}$, as shown in Eq. (2) [22]. From Eq. (2), f is determined to be 286 Hz (312 Hz with a 50.8 mm (2 in) mitigation structure at the bottom closed end). Also, since the cross-sectional area of the specimen is relatively small (< 5%) when compared to the total cross-sectional

area of the confining tube, then the implodable's impact is ignored when calculating frequency.

$$c_f = \left(\frac{L_{al}}{L_{ac}+L_{al}}\right)\frac{c_w}{\sqrt{1+\frac{KD}{E_{al}h}}} + \left(\frac{L_{ac}}{L_{ac}+L_{al}}\right)\frac{c_w}{\sqrt{1+\frac{KD}{E_{ac}h}}} \quad (1)$$

$$f = \frac{c_f}{4L} \quad (2)$$

Table 5.2 Dimensions and Properties of Confining Tube

Parameter	Value
c_w (Wave speed in water)	1483 m/s
K (Bulk modulus of water)	2.2 GPa
h (Wall thickness of confining tube)	25.4 mm (1.0 in)
D (Inner Diameter of confining tube)	178 mm (7.0 in)
E_{al} (Elastic modulus of aluminum)	69 GPa
E_{ac} (Elastic modulus of acrylic)	3.17 GPa
L_{al} (Length of aluminum section)	356 mm (14.0 in)
L_{ac} (Length of acrylic section)	457 mm (18.0 in)

By performing a Fast Fourier Transform (FFT) analysis on the recorded hammer pressure data, the dominant frequency of oscillation was obtained as shown in Table 5.3. For the control case (C1), the frequency is 26 % smaller than the theoretical value; since theory does not take into account any viscous losses or the impact of the implodable specimen [6]. The baffle and spheres cases (B1 and S1) had negligible changes in frequency; similar to the changes in pressure. However, all foam and piston cases (F1, F2, P1, P2, and P3) had a drastic decrease in its dominant frequency from the control case as shown in Table 5.3. The reduction in frequency is not explained by the change in tube length due to the additional of the mitigation technique; as mentioned earlier, decreasing tube length increases natural frequency. Unlike the decrease in pressures, optimizing the foam behavior by increasing the collapse

pressure did not decrease frequency significantly. Therefore, both phenomena are not related to each other. Rather, the change in prolonging of the hammer cycle is likely due to the dampening properties of the foam, which is why the smaller diameter foams (piston cases) have a lower frequency reduction.

Table 5.3 Experimental frequency response

Cases	Mitigation Method	Peak Pressure (MPa)	Peak Pressure Change (%)	Frequency, f (Hz)	Frequency Change (%)
C1	None	3.08 +/- 0.05	N.A.	226.5 +/- 0.7	N.A.
B1	Baffle	3.07 +/- 0.02	-0.3	226.7 +/- 0.9	0.1
S1	Spheres	2.96 +/- 0.02	-3.9	226.3 +/- 0.3	-0.1
F1	Foam	2.29 +/- 0.14	-25.6	169.9 +/- 0.3	-25.0
F2	Foam	1.36 +/- 0.18	-55.8	168.7 +/- 0.4	-25.5
P1	Foam Piston	2.06 +/- 0.09	-33.1	188.8 +/- 0.8	-16.6
P2	Foam Piston	2.14 +/- 0.14	-30.5	193.6 +/- 0.5	-14.5
P3	Foam Piston	1.67 +/- 0.11	-45.7	186.4 +/- 0.6	-17.7

4. Conclusions

An experimental investigation was conducted to evaluate mitigation methods for reducing the degree of cavitation at the closed end while simultaneously reducing the damage potential caused by the water hammer wave. Pressure measurements and high-speed DIC measurements were carried out to correlate the structural behavior with pressure history. The main findings of this study are as follows:

- The baffles (B1) and spheres (S1) techniques did not affect the magnitude or frequency of the pressure significantly. However, the high-density foam (F1) and foam-piston (P1) had a substantial effect on the frequency and well as the pressure magnitude.
- The foam behavior was optimized by having the collapse pressure (Pcr = 2.79 MPa) to be slightly lower than the foam's quasistatic crushing pressure (P = 2.85 MPa). After the implodable goes unstable and the event become dynamic, the

pressure rises until the dynamic crushing strength is reached and the foam fails in the flow region. The crushing of the foam in the flow region mitigates the pressure within the confining tube.

- Unlike the decrease in pressures, optimizing the foam behavior by increasing the collapse pressure did not decrease frequency significantly. Therefore, both phenomena are not related to each other. Rather, the change in prolonging of the hammer cycle is likely due to the dampening properties of the foam, which is why the smaller diameter foams (piston cases) have a lower frequency reduction.

Acknowledgements

The authors kindly acknowledge the financial support provided by Dr. Thomas Fu under the Office of Naval Research (ONR) Grant No. N00014-15-1-2046.

References

[1] Turner, S. E. (2007). Underwater implosion of glass spheres. The Journal of the Acoustical Society of America, 121(2), 844. doi:10.1121/1.2404921

[2] Turner, S. E., & Ambrico, J. M. (2012). Underwater Implosion of Cylindrical Metal Tubes. Journal of Applied Mechanics, 80(1), 011013. doi:10.1115/1.4006944

[3] Urick, R. J. (1963). Implosions as Sources of Underwater Sound. The Journal of the Acoustical Society of America, 35(11), 1903. doi:10.1121/1.2142767

[4] Vath, F. (1968). Development of buoyancy material for the deep submergence search vehicle. Evaluation of sympathetic implosion of buoyancy modules.

Defense Technical Information Center. Naval Applied Science Laboratory, Brooklyn, New York

[5] Orr, M., & Schoenberg, M. (1976). Acoustic signatures from deep water implosions of spherical cavities. The Journal of the Acoustical Society of America, 59(5), 1155. doi:10.1121/1.380977

[6] Gupta, S., Matos, H., Shukla, A., & Leblanc, J. M. (2016). Pressure signature and evaluation of hammer pulses during underwater implosion in confining environments. The Journal of the Acoustical Society of America J. Acoust. Soc. Am., 140(2), 1012-1022. doi:10.1121/1.4960591

[7] Gupta S, LeBlanc JM, Shukla A (2015) Sympathetic underwater implosion in a confining environment. Extreme Mech Lett 3:123–129. doi: 10.1016/j.eml.2015.03.007

[8] Costa, L., & Turner, S. (2008). Implosion Testing within a Small-Scale Torpedo Tube. NAVSEA NUWC-NPT Technical Memo 08-014.

[9] Matos, H., Gupta, S., & Shukla, A. (2017). Structural instability and water hammer signatures from shock-initiated implosions in confining environments. Mechanics of Materials. doi:10.1016/j.mechmat.2016.12.004

[10] Accident Grounds Neutrino Lab. (2001). Retrieved January 13, 2016, from http://physicsworld.com/cws/article/news/2001/nov/15/accident-grounds-neutrino-lab

[11] R.I.P. A.B.E. (2010). Retrieved January 13, 2016, from http://www.whoi.edu/oceanus/feature/rip-abe

[12] Robotic Deep-sea Vehicle Lost on Dive to 6-Mile Depth. (2014). Retrieved January 13, 2016, from http://www.whoi.edu/news-release/Nereus-Lost

[13] Farhat, C., Wang, K., Main, A., Kyriakides, S., Lee, L., Ravi-Chandar, K., & Belytschko, T. (2013). Dynamic implosion of underwater cylindrical shells: Experiments and Computations. International Journal of Solids and Structures, 50(19), 2943-2961. doi:10.1016/j.ijsolstr.2013.05.006

[14] Ikeda, C. M., Wilkerling, J., & Duncan, J. H. (2013). The implosion of cylindrical shell structures in a high-pressure water environment. Proceedings of the Royal Society A: Mathematical, Physical and Engineering Sciences, 469(2160), 20130443-20130443. doi:10.1098/rspa.2013.0443

[15] Gish, L., & Wierzbicki, T. (2015). Estimation of the underwater implosion pulse from cylindrical metal shells. International Journal of Impact Engineering, 77, 166-175. doi:10.1016/j.ijimpeng.2014.11.018

[16] Gupta, S., Parameswaran, V., Sutton, M. A., & Shukla, A. (2014). Study of dynamic underwater implosion mechanics using digital image correlation. Proceedings of the Royal Society A: Mathematical, Physical and Engineering Sciences, 470(2172), 20140576-20140576. doi:10.1098/rspa.2014.0576

[17] Pinto, M., Gupta, S., & Shukla, A. (2015). Study of implosion of carbon/epoxy composite hollow cylinders using 3-D Digital Image Correlation. Composite Structures, 119, 272-286. doi:10.1016/j.compstruct.2014.08.040

[18] Pinto, M., Gupta, S., & Shukla, A. (2015). Hydrostatic Implosion of GFRP Composite Tubes Studied by Digital Image Correlation. Journal of Pressure Vessel Technology, 137(5), 051302-051302.

[19] Gupta, S., LeBlanc, J., & Shukla, A., (2014) Mechanics of the implosion of cylindrical shells in a confining tube. Int J Solids Struct 51:3996–4014. doi: 10.1016/j.ijsolstr.2014.07.022

[20] Gupta, S., LeBlanc, J., & Shukla, A., (2015) Implosion of longitudinally off-centered cylindrical volumes in a confining environment. J Appl Mech 82:051001. doi: 10.1115/1.4029917

[21] Gupta, S., Matos, H., Leblanc, J. M., & Shukla, A. (2016). Shock initiated instabilities in underwater cylindrical structures. Journal of the Mechanics and Physics of Solids, 95, 188-212. doi:10.1016/j.jmps.2016.05.034

[22] Ghidaoui, M. S., Zhao, M., Mcinnis, D. A., & Axworthy, D. H. (2005). A Review of Water Hammer Theory and Practice. Applied Mechanics Reviews Appl. Mech. Rev., 58(1), 49. doi:10.1115/1.1828050

[23] Tijsseling, A. (2007). Water hammer with fluid–structure interaction in thick-walled pipes. Computers & Structures, 85(11-14), 844-851. doi:10.1016/j.compstruc.2007.01.008

[24] Keramat, A., Tijsseling, A., Hou, Q., & Ahmadi, A. (2012). Fluid–structure interaction with pipe-wall viscoelasticity during water hammer. Journal of Fluids and Structures, 28, 434-455. doi:10.1016/j.jfluidstructs.2011.11.001

[25] Meniconi, S., Brunone, B., & Ferrante, M. (2012). Water-hammer pressure waves interaction at cross-section changes in series in viscoelastic pipes. Journal of Fluids and Structures, 33, 44-58. doi:10.1016/j.jfluidstructs.2012.05.007

[26] Arastu, A. H., & Tom, E. (2003). Water Hammer Analysis/Prevention/Mitigation in Fire Protection Systems at Power Plants. Volume 1: Fora, Parts A, B, C, and D. doi:10.1115/fedsm2003-45679

[27] Chen, T., Xu, C., Lin, Q., Loxton, R., & Teo, K. L. (2015). Water hammer mitigation via PDE-constrained optimization. Control Engineering Practice, 45, 54-63. doi:10.1016/j.conengprac.2015.08.008

[28] ASTM Standard D3574-16. (2016). Standard Test Methods for Flexible Cellular Materials-Slab, Bonded, and Molded Urethane Foams. ASTM International, West Conshohocken, PA. doi: 10.1520/D3574-16

CHAPTER 6. Underwater Nearfield Blast Performance of Hydrothermally Degraded Carbon-Epoxy Composite Structures

by

Helio Matos[1], Carlos Javier[1], James LeBlanc[2], and Arun Shukla[1]

1 Dynamic Photo Mechanics Laboratory, Department of Mechanical, Industrial and Systems Engineering, University of Rhode Island, Kingston, RI 02881

2 Naval Undersea Warfare Center (Division Newport), Newport, RI 02841

In preparation for publication

Abstract

An experimental and numerical study was conducted to evaluate the response of weathered unidirectional composite plates subjected to near-field blast loading. Naval structures are subjected to aggressive marine environments during their service life that can significantly degrade their performance over time. The composite materials in this study are carbon-epoxy composite plates with [0, 90]s and [45, -45]s layups. The composites were aged rapidly through submersion in 65 ˚C seawater for 35 and 70 days; which simulates 10 and 20 years of real life operating conditions respectively. Experiments were performed by fully clamping the specimen plates to an air-backed enclosure in a water tank. An RP-503 explosive was placed underwater behind the composite structure to be loaded. During the experiments, transducers measured the pressure emitted by the explosive, and three high-speed cameras captured the entire event. Two of the cameras were placed apart facing the specimen to measure full field displacement, velocities, and strains through 3D Digital Image Correlation analysis and a third high-speed camera was used to record the explosive's behavior and bubble-to-specimen interaction. Additional experiments were performed to obtain the non-weathered and weathered material properties as well as the residual strength post blast experiments. Additionally, a Coupled Eulerian-Lagrange finite element simulation was conducted to complement the experimental findings. Results show that the diffusion of water into the composite material leads to the blast response degradation as well as weakening of mechanical properties, especially shear properties. Residual strength experiments also show a significant decrease in the structural integrity post blast loading for the weathered composites.

1. Introduction

In this study, an experimental and numerical investigation was conducted to evaluate the response of weathered unidirectional composite plates subjected to near-field explosive/blast loading. This research arises from the concern of damage to naval and marine composite structures such as ships, submarines, and underwater vehicles [1, 2]. During the service life of these structures, their mechanical properties degrade due to the continuous exposure to an aggressive environment [3]. In undesirable circumstances, marine structures can be further subjected to shock and blast loadings. If the degradation of mechanical properties is not accounted for under these highly dynamic conditions, the damages and losses could be fatal.

A major cause for mechanical degradation in composites in a marine environment is the diffusion of water into the matrix material [3]. The diffusion process is relatively well established and can be described by a diffusion coefficient that is a function of many parameters such as temperature, the composition of resin and curing agent, fillers, and so on. The value for diffusion coefficient and the theoretical models used to describe the diffusion varies in previous studies of diffusion in composites [4-18]. A common and well-accepted model for epoxy resins is a Fickian model [14] which uses Fick's second law to predict how a material's concentration changes over time [19-20].

Previous studies used a Fickian model to study the properties changes during low strain rate loading of diffused composites. These studies agreed that the mechanical property degrades over time due to an increase in mass, internal stresses due to

swelling, and loss of interlaminar strength [15-18]. Current research on the high strain rate response of weathered composites is very limited. Recently, there has been one work that analyzes the shock response of weathered composites plates [21]. Moreover, many experimental and numerical studies analyze the dynamic response of composite plates due to underwater explosives [22-26], but a study on the explosive response has never been made in regards to weathered composites.

The aim of this study is to understand better how a composite plate's blast performance is affected by prolonged exposure to seawater. This work experimentally and numerically analyses the dynamic response of weathered composite plates subjected to nearfield underwater blasts from explosives. In the experimental portion, a 3D Digital Image Correlation (DIC) technique is implemented to capture real-time high-speed deformation for understanding fluid-structure interaction. In the numerical portion, a Coupled Eulerian-Lagrange (CEL) simulation was used to model and go beyond the experimental conditions to predict the composite's performance in different scenarios.

2. Experimental Procedures

2.1. Composite Material

2.1.1. Material Manufacturing

The composite materials used consists of four unidirectional carbon fiber sheets with [0, 90]s and [45, -45]s layups. These materials were manufactured by the University of Rhode Island students at TPI Composites Inc. in Warren, RI. The composites were made from two layers of +/- 45˚ biaxial carbon fabric and an epoxy resin/hardener mixture. The fabric is composed of Tenax HTS40 F13 24K 1600tex

carbon fibers (1% polyurethane-based sizing finish) from Toho Tenax Inc. in Rockwood, TN. Also, the resin/hardener is a 100/30 weight mixture of the RIMR135/RIMH137 epoxy from Momentive Performance Materials Inc. in Waterford, NY.

The epoxy mixture was drawn into the fabric by Vacuum Infusion at a constant pressure of 730 mmHg. After hardening, curing was performed by placing the composite plate in an oven at 70 ˚C for 10 hours. All specimens for both layups were cut from a single large composite sheet to minimize variations in the epoxy mixture and fiber content. The final product was a 1.26 mm (0.050 in) thick composite plate with 1% void content (measured in accordance to ASTM Standard D2734 [27]) and 60% fiber volume content. Table 6.1 lists the product information and properties of interest for the fiber, fabric, epoxy, and composite plate.

Table 6.1 Carbon and epoxy product information and properties

	Carbon Fiber	**Fabric**	**Epoxy**	**Composite Plate**
Manufacturer	Toho Tenax Inc.	Saertex LLC.	Momentive Performance Materials Inc.	University of Rhode Island
Product Number	HTS40	XC611	RIMR135/RIMH137	---
Density	1600 tex (Linear)	602 g/m^2 (Areal)	1150/955 kg/m^3	1420 kg/m^3
Wet/Dry Glass Transition Temperature	---	---	72/86 ˚C	72/86 ˚C

2.1.2. Mechanical Testing

Quasistatic tensile and shear properties were obtained by using an Instron 5585 and following ASTM Standards D3039 [28] (with [0, 90]s specimens) and D3518 [29] (with [45, -45]s specimens) respectively. All strains data were measured with 2-D DIC from images captured by a Prosilica camera (model GC2450 from Allied Vision Technologies GmbH in Stadtroda, Germany). The tensile and shear tests were used to

calculate the material properties for the numerical models. The strain rate sensitivity of carbon/epoxy composites, though not negligible, is very small (especially for normal stresses) [30]; therefore, numerical results are reasonably comparable to the true (experimental) results with the quasistatic properties. Lastly, quasistatic compressive tests were performed on tested specimens using ASTM Standard 7137 [31] to measure and compared compressive residual strength properties between non-weathered and weathered samples.

2.2. Weathering Facility

The composite materials are placed in a 3.5% NaCl solution (prepared in accordance to ASTM Standard D1141 [32]) as shown in Figure 6.1; this salinity was chosen due to it being a normal concentration of several ocean bodies. Four water heaters (Model LXC from PolyScience in Niles, IL) are used to maintain a temperature of 65˚C. It is important for the solution temperature to be below the wet glass transition temperature of the composite material. Beyond glass transition, there will be changes in the mechanical properties unrelated to the aging aspect of this study [5]. However, a high temperature is still desired to attain a fast acceleration factor; hence, a temperature reasonably lower than the wet glass transition was chosen.

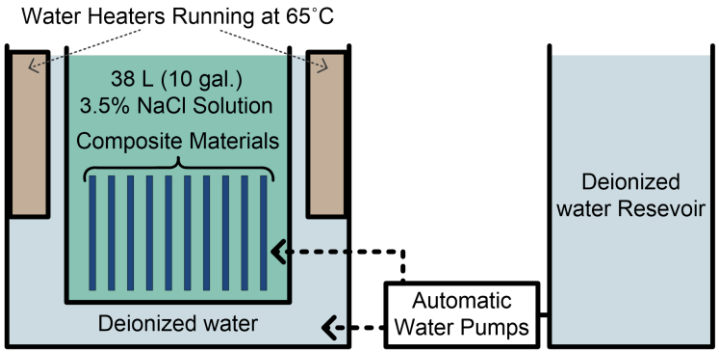

Figure 6.1 Weathering facility setup

Float switches and water pumps are used to maintain a constant water level. As water evaporates, one float switch in the deionized water and one in the saltwater tank will activate individual water pumps to replenish the volume lost; thus, the salinity remains constant, the heaters work properly at a low maintenance level, and water passively circulates as room temperature water is introduced. For this study, the composite materials are exposed to the salt water for consecutive 35 and 70 days. Experiments are initiated immediately after the specimens are removed from the salt water exposure to avoid moisture loss as suggested by ASTM Standard D5229 [33].

2.3. Blast Facility

2.3.1. Facility and Specimen Details

To perform the blast experiments, the 1.26 mm (0.050 in) thick carbon-epoxy composite plate is fully clamped inside an 1800 L (475 gallons) water tank. The water tank is made of 12.7 mm (0.5 in) thick steel, it is cubic in shape with dimensions of 1.2x1.2x1.2 m^3 (4x4x4 ft^3), and it has an inner 45 L (12 gallons) air chamber. The composite specimen is clamped between the water and air chambers with a 25.4 (1 in)

all-around clamping width; leaving a 254x254 mm^2 (10x10 in^2) exposed area as shown in Figure 6.2.

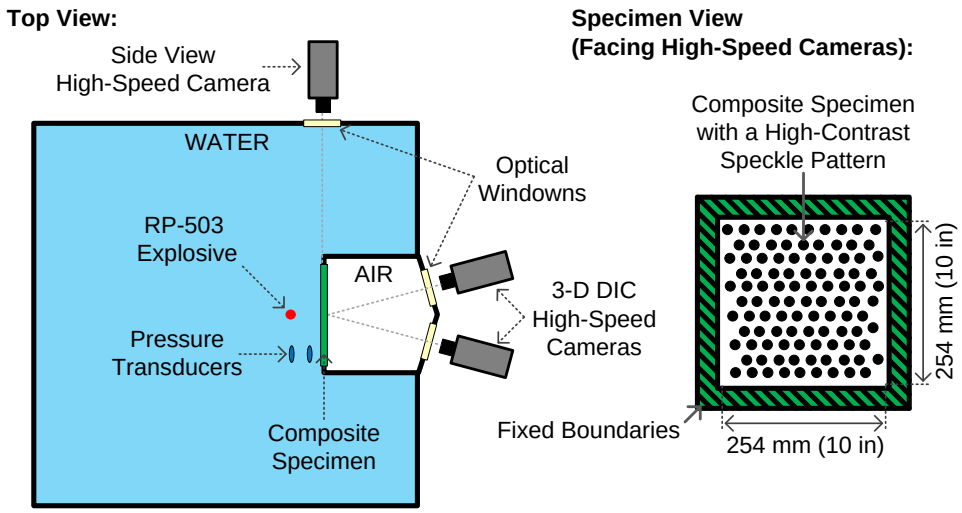

Figure 6.2 Blast facility experimental setup

An RP-503 explosive was used to load the composite structure; it is submerged in the water, centered to the specimen, and placed at a 152 mm (6 in) standoff distance (additional standoff distances were also explored; see Table 6.2 for details). Two dynamic pressure transducers (PCB 138A05, PCB Piezotronics Inc. in Depew, NY) are located next to the specimen and explosive (as illustrated in Figure 6.2) at 152 mm (6 in) and 203 mm (8in) distances from the explosive. During the experiments, a Dash 8HF data acquisition system (from AstroNova Inc. in Warwick, RI) captured the pressure data at two mega samples per second. Furthermore, two Photron SA1 high-speed cameras (from Photron USA Inc. in San Diego, CA) are placed 14˚ apart outside the blast facility and used to capture high-speed images of the specimen at 10,000 frames per second (each image has an 832x748 spatial pixel resolution). The photographs from the high-speed cameras are captured through optically clear windows in the tank. These images are later used for the Digital Image Correlation

analysis. A third Photron SA1 camera is used (as shown in Figure 6.2) to record the explosive and bubble-to-structure interactions at 10,000 frames per second (with a 576x992 spatial pixel resolution). High-intensity light sources (Super Sun-Gun SSG-400 from Frezzi Energy Systems Inc. in Hawthorne, NJ; not shown in Figure 6.2) are used to illuminate the recorded images. The experimental cases and its details are summarized in Table 6.2. Each experimental case has been repeated two times to validate the results (three for the 45s_0WD_D3 case in Table 6.2).

Table 6.2 Experimental cases details

Cases	Layup	Standoff Distance, mm (in)	Weathering Exposure, days
45s_0WD_D1	[45,-45]s	76 (3)	0
45s_0WD_D2	[45,-45]s	114 (4.5)	0
45s_0WD_D3	[45,-45]s	152 (6)	0
45s_35WD_D3	[45,-45]s	152 (6)	35
45s_70WD_D3	[45,-45]s	152 (6)	70
90s_0WD_D3	[0,90]s	152 (6)	0
90s_70WD_D3	[0,90]s	152 (6)	70

The composite specimen's 254x254 mm^2 (10x10 in^2) exposed area that is facing the high-speed cameras is coated with high-contrast speckle patterns. The speckle patterns are created by randomly placing flat-white paint dots (sized 9-12 pixels per dot) on a flat-black painted background until approximately 50% of the surface area of the specimens are covered by the white dots. When clamping the composite plate, a skin layer of silicon adhesive is applied to the clamping surface to avoid water penetration into the air chamber from the clamping boundaries; therefore during the experiments, the specimen has water and air-fluid boundaries similar to a ship hull.

2.3.2. Digital Image Correlation Reliability

The high-speed images are analyzed using commercially available DIC software (VIC3D 7 from Correlated Solutions, Inc., Columbia, SC) to measure full-field displacements across the viewable surface of the specimen by triangulating the position of each unique feature in the speckle pattern. Previous work [34] outlines the calibration procedures that validate the accuracy of the DIC results when capturing images through an optical window (where changes in refractive index are present). It was found that the optical windows need to be perpendicular to the viewing axis [34] to minimize DIC displacement errors. For this study, the in-plane displacement errors are 1.2%, and the out-of-plane errors are 2.5%.

3. Numerical Model

A numerical Finite Element Analysis (FEA) model similar to previous work [26] was created with the LS-DYNA code from the Liver Software Technology Corp. The model uses a Coupled Eulerian-Lagrange (CEL) formulation that is capable of capturing the fluid-structure interaction between the fluid and composite plate as well as an accurate representation of the explosive's detonation. All models were constructed using the CGS unit system, and simulations run in the double precision mode of LS-DYNA's Version 971, Release 4.2.1.

The FEA model consists of the air, composite specimen, water, and RP-503 charge as shown in Figure 6.3. This model is representative of a subdomain from the full experimental test facility for computational efficiency. The exposed loading area, 120 mm of air, and 200 mm of water is included in the modeled subdomain. The explosive is centered to the composite plate and has a standoff distance of 152 mm. During the

experiments, the reflections from the tank walls are relatively small in magnitude and have minor effects on the composite's response. Therefore, the experiments behave as they would in a free-field condition (where no reflections are present), a larger modeling subdomain is not necessary, and the model's external fluid faces are set as non-reflecting boundary conditions.

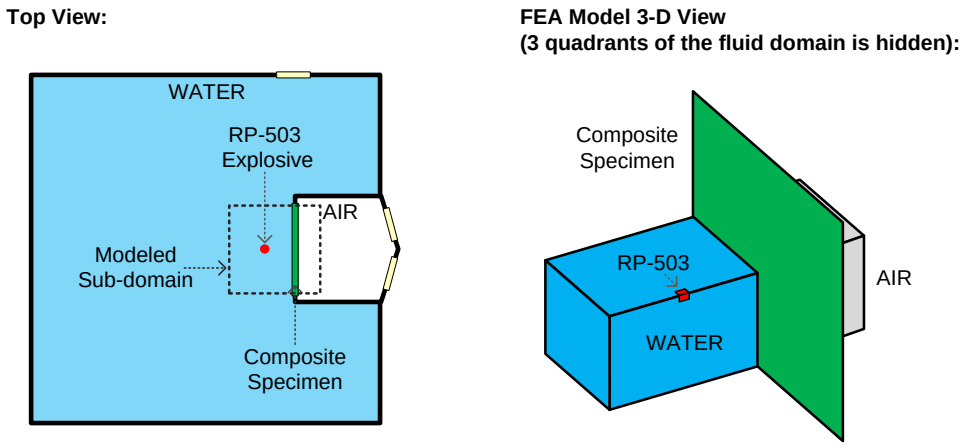

Figure 6.3 Finite element model configuration

All Eulerian components in the model use a combination of material definition and equation of state (EOS). For water, density is defined as 1 g/cm^3, and a Gruneisen EOS is used with a sound speed of 149,000 cm/s. For air, density is defined as 0.0013 g/cm^3 and a Linear Polynomial EOS is used as a gamma law EOS (where $C_0 = C_1 = C_2 = C_3 = C_6 = 0$ and $C_4 = C_5 = \gamma - 1 = 0.4$). The RP-503 explosive is created with a JWL EOS by assuming it is composed of 621 mg of RDX instead of the actual 454 mg of RDX and 167 mg of PETN. This assumption is acceptable since the explosive is mostly RDX and the JWL coefficient of the PETN is similar to the RDX's. The explosive's physical and EOS parameters are provided in Table 6.3.

Table 6.3 RDX (a) material and (b) JWL EOS parameters [35]

(a)

Material Parameters	
ρ	1.77 g/cm^3
D	850e3 cm/s
Chapman-Jouget Pressure	3.41e13 dyn/cm^2

(b)

JWL EOS Parameters	
A	7.78e12 dyn/cm^2
B	7.07e12 dyn/cm^2
R1	4.485
R2	1.068
ω	0.3
E_o	5.93e10

The composite plate is modeled using a single layer of shell elements. The density of the plate is set to 1.42 g/cm^3 stiffness of the plate is defined in Sec. 4.2. Composite damage is attained by using the material model from LS-DYNA (Mat_022). This material definition encompasses failure criterions such as tension, in-plain shear, and compression in the transverse direction. The loading on the composite plates occurs in a two-step process. First, a quasistatic pressure is uniformly applied over the entire face of the plate. The quasistatic pressure is representative of the depth pressure acting on the submerged plate. Second, the explosive detonation is initiated which leads to a transient response of the composite plate. In this study, six different numerical cases are analyzed as shown Table 6.4. The first four numerical cases are done to establish confidence in the numerical results while the last two cases analyze the performance of the composite plate to different loading conditions.

Table 6.4 Numerical cases details

Cases	Layup	Standoff Distance, mm (in)	Weathering Exposure, days
N45s_0WD_D1	[45,-45]s	76 (3)	0
N45s_0WD_D2	[45,-45]s	114 (4.5)	0
N45s_0WD_D3	[45,-45]s	152 (6)	0
N45s_70WD_D1	[45,-45]s	76 (3)	70
N45s_70WD_D2	[45,-45]s	114 (4.5)	70
N45s_70WD_D3	[45,-45]s	152 (6)	70

4. Results and Discussions

4.1. Weathering

Since the activation energy (E_a) for a material is constant, a mass diffusion study can be performed at various temperatures (different diffusion rates) to obtain the acceleration factor (AF) of submersion at for the material a specific temperature [36]. For this study, moisture absorption was measured for composites submerged in 3.5% NaCl solutions at 5, 25, 45, 65, and 85 ˚C in accordance to ASTM Standard D5229 [33]. The last temperature for moisture absorption (85 ˚C) is slightly higher than the wet glass transition temperature, and it is only used for calculating AF (since E_a is constant).

If the diffusivity into the composite plate obeys Fick's second law of diffusion [19] and is one dimensional, then the diffusion coefficient (D) can be calculated using Eq. (1) [20]. The diffusion coefficient must be calculated from a point that is within the initial linear portion of the mass diffusion curve (≤ 50% mass saturation). The diffusion coefficient can also be related to E_a by using Arrhenius' Relation given in Eq. (2). To solve for E_a, Eq. (2) is written in logarithmic form as shown in Eq. (3), then $-E_a/R$ can be found on the slope of a linear plot for the various diffusion temperatures [20]. Figure 6.4 (a) and (b) shows the mass diffusion for different temperatures and the logarithmic relationship between D and E_a respectively.

$$D = \frac{\pi}{t}\left(\frac{h}{4}\frac{M_t}{M_s}\right)^2 \tag{1}$$

$$D = Ce^{-\frac{E_a}{RT}} \tag{2}$$

$$\ln(D) = \ln(C) - \frac{E_a}{RT} \tag{3}$$

Where t is time; M_t is the composite's mass at time t; M_s is the composite's saturated mass; h is the composite plate's thickness; C is a constant; R is the universal gas constant; and T is absolute temperature.

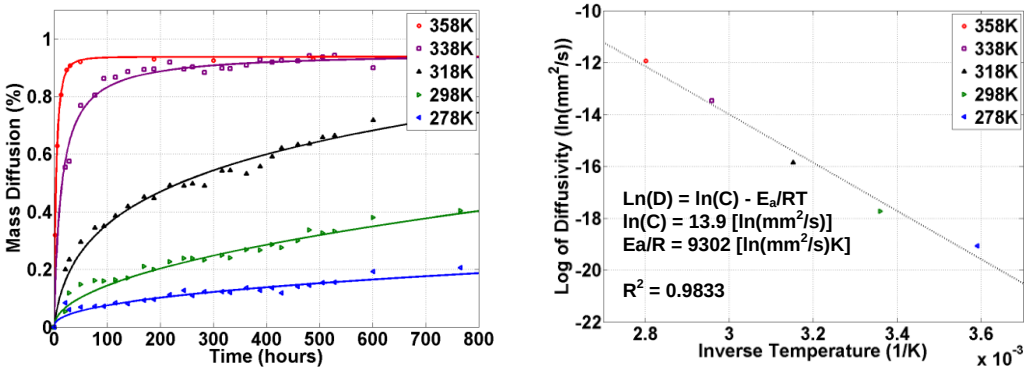

(a) **(b)**

Figure 6.4 (a) Mass diffusion for various temperatures and (b) logarithmic relationship between diffusivity and temperature

After obtaining the activation energy for the composite material, AF can be found as the ratio of working over experimental diffusion rates as shown in Eq. (4) [36]. Additionally, the submersion experiments are performed at a constant temperature (T_1= 338K), but the service temperature (T_2) can vary depending on application; hence, AF is application dependent. For instance, the AF for a ship operating in the Arctic Ocean will be much higher than one operating in the Mediterranean Sea. Assuming an average ocean temperature of 16 ˚C, 35 and 70 days of submersion approximates to 10 and 20 years of service respectively.

$$AF = \frac{Ce^{-\frac{E_a}{RT_2}}}{Ce^{-\frac{E_a}{RT_1}}} = e^{\left(\frac{E_a}{R}\right)\left(\frac{T_2-T_1}{T_1T_2}\right)} \quad (4)$$

4.2. Mechanical Properties

4.2.1. Composite Plate

To simplify the material model, a plane stress assumption (using shell elements in the numerical model) is made for the composite plate. The elastic modulus (E_1 and E_2), Poisson's ratio (v_{12} and v_{21}), shear modulus (G_{12}), and failure strains can be found by the standards outlined in Section 2 and are shown in Table 6.5. The elastic modulus and Poisson's ratio was found to be the same in both principle directions ($E_1 = E_2$ and $v_{12} = v_{21}$). The normal stress has a linear behavior until failure, but the shear stress has a bilinear behavior; the shear yield and failure stresses are listed in Table 6.5. All results for the material properties in Table 6.5 are given as the average from six experiments with its standard deviation.

Table 6.5 Composite's Mechanical Properties

Weathering time (Days)	0	35	70
E_1, E_2 (GPa)	78.4 +/- 1.8	78.0 +/- 2.1	74.9 +/- 2.6
v_{12}, v_{21}	0.039 +/- 0.014	0.040 +/- 0.010	0.042 +/- 0.009
Failure Normal Strain (%)	1.46 +/- 0.09	1.38 +/- 0.09	1.36 +/- 0.07
G_{12} (GPa)	7.38 +/- 0.19	5.32 +/- 0.24	4.92 +/- 0.22
Yield Shear Stress (kPa)	36.1 +/- 1.1	25.3 +/- 1.0	21.7 +/- 0.6
Failure Shear Stress (kPa)	45.3 +/- 1.2	41.3 +/- 1.9	38.7 +/- 2.6
Failure Shear Strain (%)	4.92 +/- 0.79	7.25 +/- 0.25	7.28 +/- 0.89

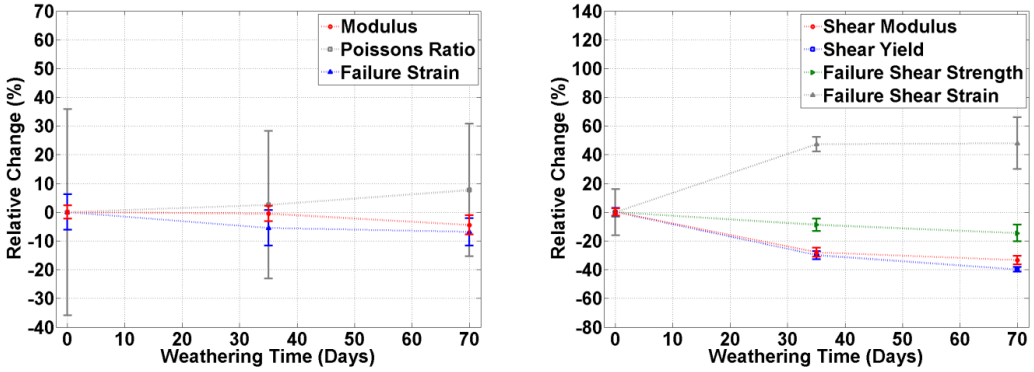

(a) **(b)**

Figure 6.5 Relative (a) normal and (b) shear properties change

4.3. Blast Response

4.3.1. Explosive Loading

During the experiments, the RP-503 underwater explosive (UNDEX) combusts at t = 0, and high-pressure waves load the composite specimen. The high pressures and velocities from the explosive lead to the formation of a cavitation bubble at the charge location as shown in Figure 6.6 (a) at t = 3 ms. Also, the high pressures loading the specimen leads to more cavitation on its surface as shown Figure 6.6 (a) at t = 15 ms. The cavitation bubble expands until its surrounding pressure is sufficiently large to cause it to collapse. After the bubble collapses, it emits another high-pressure pulse that causes the specimen's surface cavitation to collapse as well as shown Figure 6.6 (a) at t = 27 ms.

The high pressures from the explosive can be seen in Figure 6.6 (b) for different standoff distances. The shock from the explosive is distinguished by an immediate rise in pressure followed by exponential decay. The pressure, in this case, decreases spherically by 1/R from the explosive location. Also, the reflections from the tank's boundaries are small relative to the initial pressures which justify the non-reflective boundary conditions in the numerical model.

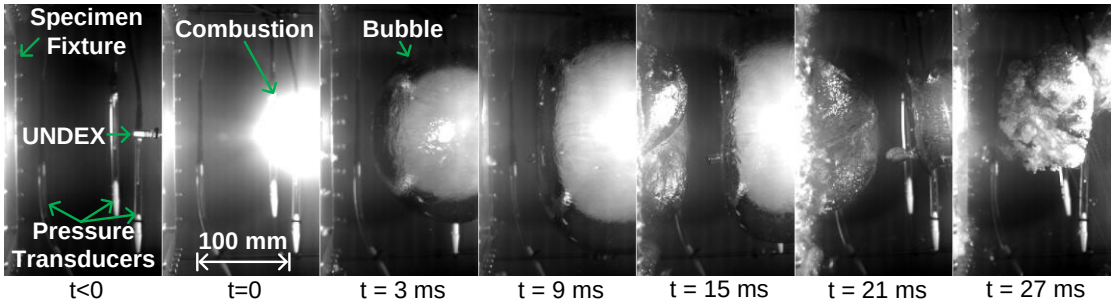

(a)

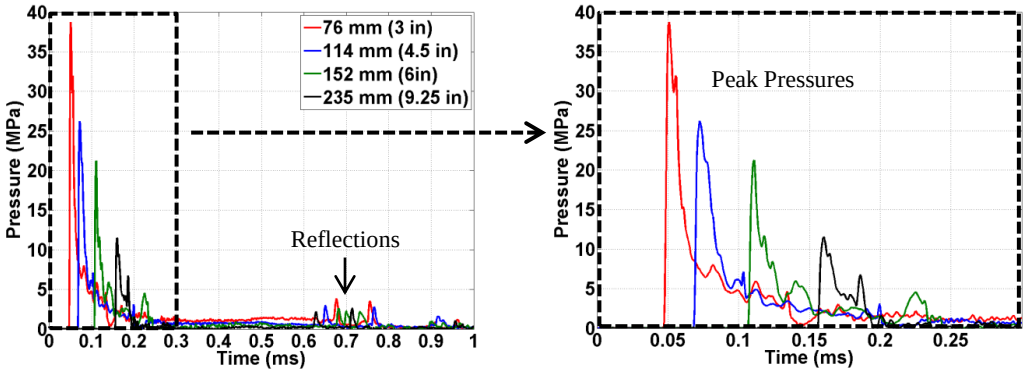

(b)

Figure 6.6 (a) Bubble dynamics and (b) high-pressures from the explosive

4.4. Deformation and Image Analysis

The out of plane deformation obtained from the 3D DIC is shown in Figure 6.7 as center displacements. Each of the displacement curves shown in Figure 6.7 is one representative experiment. The center point displacements for the non-weathered [45,-45]s composite plate at different standoff distances is shown in Figure 6.7 (a). Decreasing the standoff distance leads to higher loading pressure and higher deformation rates. The displacement curves for the 76 mm and 114 mm standoff stop when through thickness cracking is observed in the high-speed images; delamination is seen for the 152 mm standoff during post-mortem, but not during the experiments. For the 152 mm standoff, the specimen flexes towards the air-side until cavitation covers the composite's surface (on its water-side), which causes it to flex towards the

water-side (between 8 and 24 ms after combustion). At t = 24 ms, the cavitation bubble collapses, causing an abrupt increase of displacement towards the air-side. Figure 6.7 (b) illustrates the full center point displacement cycle of the composite plate as well as the typical repeatability of these experiments.

Weathering the composite plates led to an increase in displacement for the same loading condition. The center point displacement curves for the [45,-45]s composite plates at 152 mm (6 in) standoff is shown in Figure 6.7 (c) for the non-weathered, 35 weathering days (WD), and 70 WD cases. After weathering the [45,-45]s composite for 35 days, the maximum center point displacements increase by ~ 20%. An additional ~ 5% increase in displacement is seen for the 70 WD case (though this increase is within experimentation error). The overall [0,90]s composite plate displacements are higher than the [45,-45]s plates, and the 70 WD case has center point displacements ~ 15% greater than the non-weathered case as seen in Figure 6.7 (d). A post-mortem analysis shows that in comparison to the non-weathered case, the weathered composites have more visible damage in terms of delamination and cracking (larger delamination area and longer cracks along the diagonal). However, the post-mortem of the 35 WD and 70 WD plates are not visibly distinguishable.

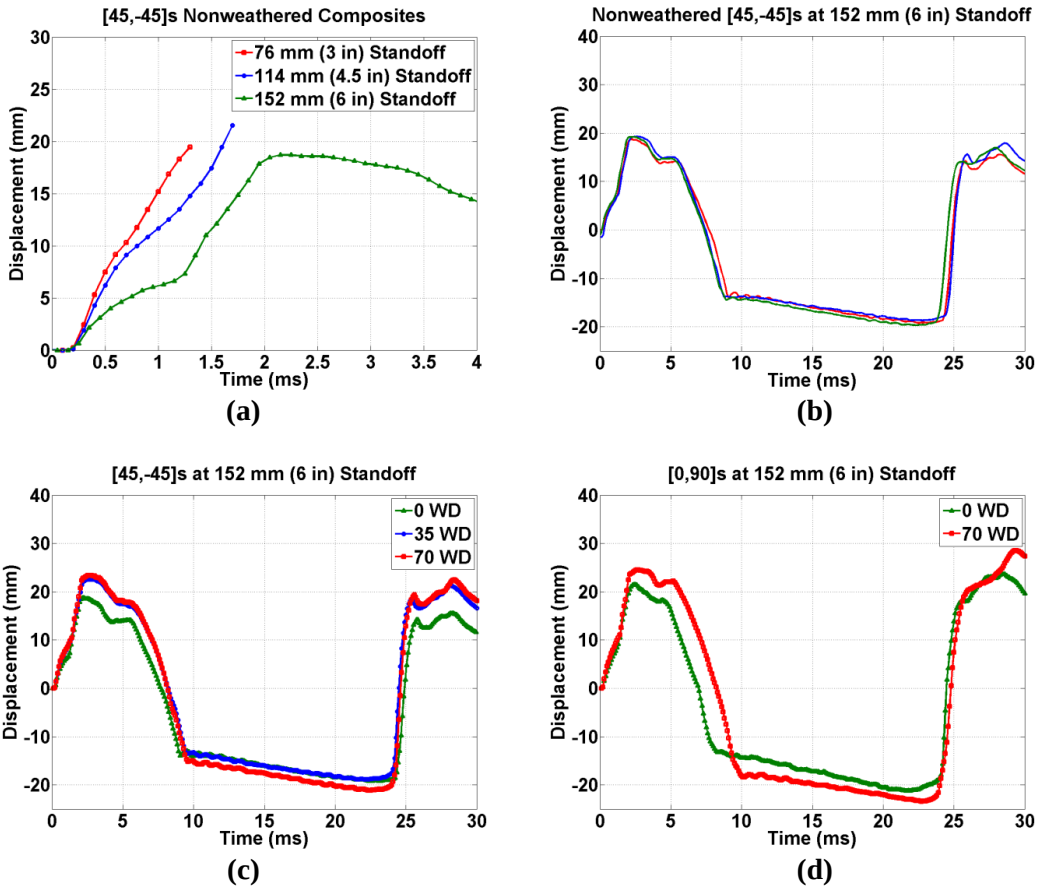

Figure 6.7 Center point displacements for (a) [45,-45]s non-weathered composites at different standoff distances, (b) [45,-45]s non-weathered composite at 152 mm (6 in) standoff, (c) [45,-45]s weathered composites, and (d) [0,90]s weathered composites

4.5. Residual Strength

Quasistatic compressive tests were performed on tested specimens using ASTM Standard 7137 [31] to measure and compared compressive residual strength properties between non-weathered and weathered samples. To perform the residual strength experiments, the composite specimen was simply supported at the 254x254 mm^2 (10x10 in^2) central area (same boundary locations as the blast experiments) as shown in Figure 6.8 (a). A schematic of the boundary and loading condition is shown in Figure 6.8 (b) as well as a 3D model for the loading fixture in Figure 6.8 (c). Figures 6.8 (d) and (e) show the residual strength in MPa versus the change in length over the

original length (this is not a measurement of strains). For the [45,-45]s composite plates, the average residual strength decrease by 29.6% for the 35 WD case, and 45.7% for the 70 WD when compared to the non-weathered case as shown in Figure 6.8 (d). For the [0,90]s composite plates, the average residual strength decrease by 46.5% for the 70 WD when compared to the non-weathered case as shown in Figure 6.8 (e).

During blast experiments, the difference in performance between the 35 WD and 70 WD cases not very distinguishable (within experimental error). However, a notable decrease in residual strength is observed between the 35 WD and 70 WD cases. This illustrates how material degradation occurs even after saturation.

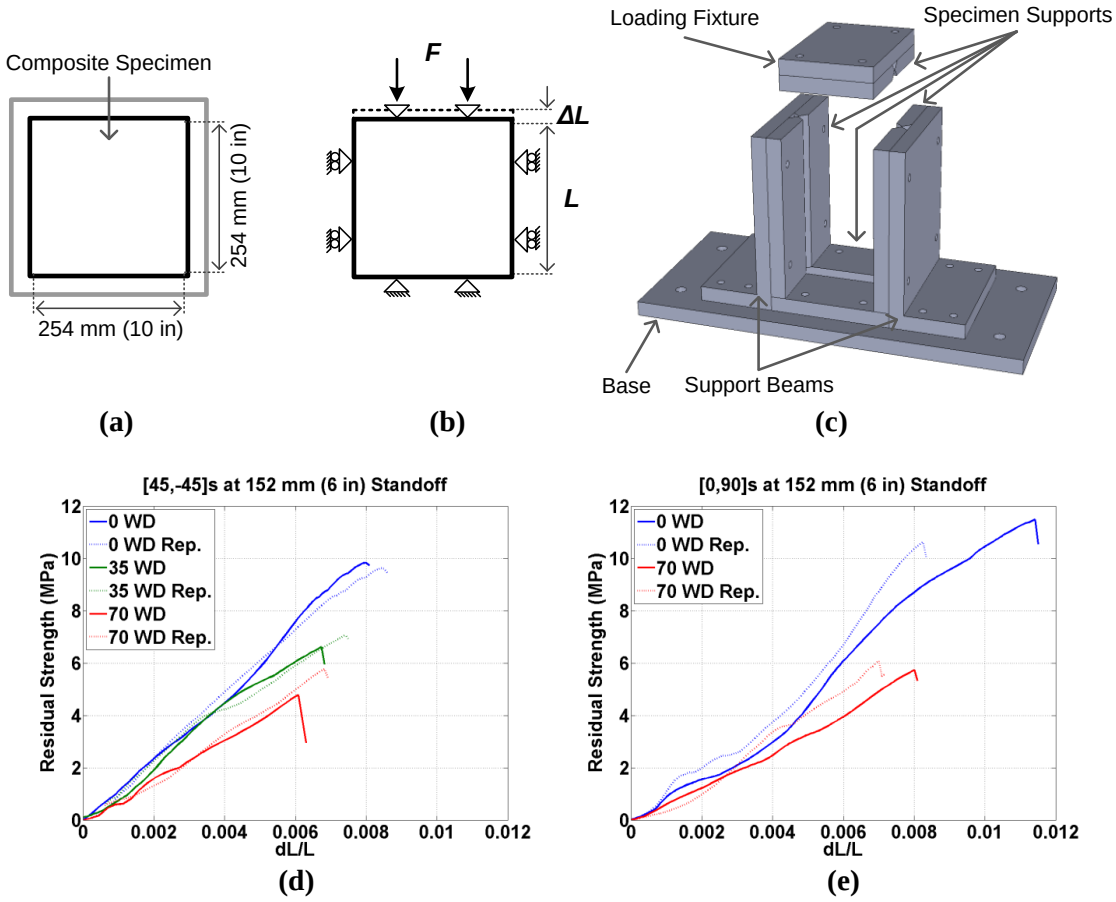

Figure 6.8 Residual strength for the (a) [45,-45]s weathered composites, and (d) [0,90]s weathered composites

5. Numerical Results

The JWL EOS and the using just RDX material to model the RP-503 explosive (instead RDX and PETN) worked well for the numerical simulations as shown in Figure 6.9 (a); where pressure from a 154 (6 in) standoff is measured as a function of time. The peak values for pressures are within 4% of error between experimental and numerical results. Also, the decay time pressure recording was accurately captured in the model.

The material response from the LS-Dyna simulation captured the peak displacement of the composite plate within 20% of error as shown in Figure 6.9 (b). However, the simulation shows a significantly faster rise time and shorter duration of motion than the experiments. A second simulation was performed using DYSMAS (a government owned software code managed by the Naval Surface Warfare Center at Indian Head, MD) instead of LS-Dyna to see how a different fluid-structure interaction (FSI) code solved the problem. DYSMAS was used in this second simulation because it is known to provide good FSI results as well as accurately capture the detonation of the charge and bubble behavior. Moreover, the DYSMAS simulation was full scale; hence the boundary reflections were included. The results from DYSMAS were closer to the experimental data with peak displacements within 15% of experimental values and longer rise time than the LS-Dyna simulation as shown in Figure 6.9 (b). However, the overall behavior or either simulation is still not very well captured by either simulations. With both FSI codes yielding similar results

independently of each other, the deformation mechanisms in the model are not well defined in either model.

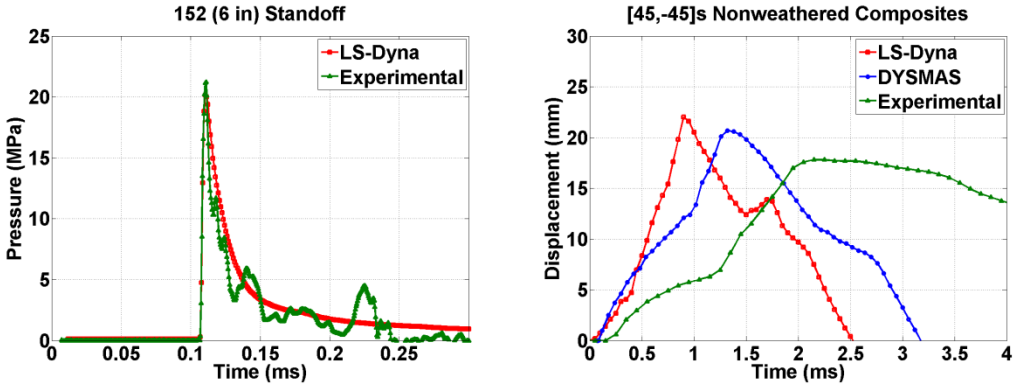

Figure 6.9 Numerical and experimental results for the (a) pressure and (6) center point displacement of the [45,-45]s [45,-45]s non-weathered composite at 152 mm (6 in) standoff

The specimens were carefully analyzed in the post-mortem, and no indication that slippage occurred was found near the boundaries. Also, by performing DIC analysis near the boundaries of the fixture, results indicate that in-plane displacements (slippage) were negligible during all experiments. However, some delamination was found near the boundaries of the specimen. With a plane stress assumption, delamination that occurs within the plate's thickness cannot be accounted for [37]; thus, the numerical results cannot represent this type of failure with shell elements. The shell element formulation can only account for in-plane damage mechanisms (such as fiber/matrix fracture) and not any debonding that occurs within composite's layers.

Delamination can cause the delay in rising time as well as the slower rebound rate with its weakening (damaging) stiffness in the experimental results seen in Figure 6.9 (b). To improve the numerical model solid elements, a tie-break type of contact can be

used to simulate delamination damage could be used. This model type of model would require the delamination strength to be equal to the tie-break force in the model.

6. Conclusions

This work experimentally and numerically analyzed the dynamic response of weathered composite plates subjected to nearfield underwater blasts from explosives. The aim of this study was to understand better how a composite plate's blast performance is affected during prolonged exposure to seawater. The main findings of this study are as follows:

- The mechanical properties of the carbon-epoxy composite used in this study degraded over 35 and 70 days of artificial weathering (hydrothermal degradation). Most notably, the shear properties degraded significantly due to the matrix material (epoxy) having a significant impact on the shear properties.
- The maximum center point displacements during the blast experiments for the [45,-45]s composite increase significantly (~ 20%) between the 35 WD and non-weathered specimen. Only a small increase in displacement (an additional ~5 %) was attained by doubling the exposure to 70 WD. Similarly, for the [0,90]s composite, a 70 WD exposure yielded ~ 15% higher than the non-weathered case.
- Residual strength experiments showed a significant discrepancy between the 35 WD and 70 WD cases in comparison to the blast experiments. This illustrates how material degradation occurs even after moisture saturation. For the [45,-45]s composite plates, the average residual strength decrease by 29.6% for the 35 WD case, and 45.7% for the 70 WD when compared to the non-weathered case.

- Material properties obtained with the plane stress assumption cannot be used to create an accurate numerical model for a nearfield blast on a carbon/epoxy plate unless a tie-break type contact is used to simulate delamination damage.

Acknowledgements

The authors kindly acknowledge the financial support provided by Kirk Jenne from the Naval Engineering Education Consortium (NEEC) Grant No. N00174-16-C-0012; the composite expertise of Tim Fallon and Mike Trapela from TPI Composites in Warren, RI; and the assistance in designing the residual strength fixture by Valentina Lopresto from the University of Naples Federico II [Università degli Studi di Napoli Federico II] in Naples, Italy.

References

[1] Mouritz, A., Gellert, E., Burchill, P., & Challis, K. (2001). Review of advanced composite structures for naval ships and submarines. Composite Structures, 53(1), 21-42. doi:10.1016/s0263-8223(00)00175-6

[2] Graham-Jones, J., & Summerscales, J. (2016). Marine applications of advanced fibre-reinforced composites. Woodhead Publishing. doi:10.1016/c2013-0-16504-x

[3] Davies, P. (2016). Environmental degradation of composites for marine structures: New materials and new applications. Phil. Trans. R. Soc. A Philosophical Transactions of the Royal Society A: Mathematical, Physical and Engineering Sciences, 374(2071), 20150272. doi:10.1098/rsta.2015.0272

[4] Shirrell, C., & Halpin, J. (1977). Moisture Absorption and Desorption in Epoxy Composite Laminates. Composite Materials: Testing and Design (Fourth Conference). doi:10.1520/stp26963s

[5] Browning, C., Husman, G., and Whitney, J. (1977). Moisture Effects in Epoxy Matrix Composites. Composite Materials: Testing and Design (Fourth Conference), STP26961S, J. Davis, Ed., ASTM International, West Conshohocken, PA, 481-496. doi:10.1520/STP26961S

[6] Deiasi, R. J., Whiteside, J. B., & Wolter, W. (1980). Effects of Varying Hygrothermal Environments on Moisture Absorption in Epoxy Composites. Fibrous Composites in Structural Design, 809-818. doi:10.1007/978-1-4684-1033-4_48

[7] Blikstad, M., Sjoblom, P. O., & Johannesson, T. R. (1984). Long-Term Moisture Absorption in Graphite/Epoxy Angle-Ply Laminates. Journal of Composite Materials, 18(1), 32-46. doi:10.1177/002199838401800103

[8] Neumann, S., & Marom, G. (1987). Prediction of Moisture Diffusion Parameters in Composite Materials Under Stress. Journal of Composite Materials, 21(1), 68-80. doi:10.1177/002199838702100105

[9] Amer, M., Koczak, M., & Schadler, L. (1996). Relating hydrothermal degradation in single fiber composites to degradation behavior in bulk composites. Composites Part A: Applied Science and Manufacturing, 27(9), 861-867. doi:10.1016/1359-835x(96)00049-8

[10] Choqueuse, D., & Davies, P. (2008). Aging of composites in underwater applications. Aging of Composites. doi:10.1201/9781439832493.ch18

[11] Sar, B., Fréour, S., Davies, P., & Jacquemin, F. (2012). Coupling moisture diffusion and internal mechanical states in polymers – A thermodynamical approach. European Journal of Mechanics - A/Solids, 36, 38-43. doi:10.1016/j.euromechsol.2012.02.009

[12] Joliff, Y., Belec, L., Heman, M., & Chailan, J. (2012). Experimental, analytical and numerical study of water diffusion in unidirectional composite materials – Interphase impact. Computational Materials Science, 64, 141-145. doi:10.1016/j.commatsci.2012.05.029

[13] Fichera, M., Totten, K., & Carlsson, L. A. (2015). Seawater effects on transverse tensile strength of carbon/vinyl ester as determined from single-fiber and macroscopic specimens. Journal of Materials Science, 50(22), 7248-7261. doi:10.1007/s10853-015-9279-3

[14] Popineau, S., Rondeau-Mouro, C., Sulpice-Gaillet, C., & Shanahan, M. E. (2005). Free/bound water absorption in an epoxy adhesive. Polymer, 46(24), 10733-10740. doi:10.1016/j.polymer.2005.09.008

[15] Choqueuse, D., Davies, P., Mazéas, F., & Baizeau, R. (1997). Aging of Composites in Water: Comparison of Five Materials in Terms of Absorption Kinetics and Evolution of Mechanical Properties. High Temperature and Environmental Effects on Polymeric Composites: 2nd Volume. doi:10.1520/stp11369s

[16] Faguaga, E., Pérez, C., Villarreal, N., Rodriguez, E., & Alvarez, V. (2012). Effect of water absorption on the dynamic mechanical properties of composites used for

windmill blades. Materials & Design (1980-2015), 36, 609-616. doi:10.1016/j.matdes.2011.11.059

[17] Tual, N., Carrere, N., Davies, P., Bonnemains, T., & Lolive, E. (2015). Characterization of sea water aging effects on mechanical properties of carbon/epoxy composites for tidal turbine blades. Composites Part A: Applied Science and Manufacturing, 78, 380-389. doi:10.1016/j.compositesa.2015.08.035

[18] Gunti, R., Prasad, A. R., & Gupta, A. (2016). Mechanical and degradation properties of natural fiber reinforced PLA composites: Jute, sisal, and elephant grass. Polymer Composites. doi:10.1002/pc.24041

[19] Davies, P., & Rajapakse, Y. (2014). Durability of composites in a marine environment. Dordrecht: Springer.

[20] Crank, J. (1975). The Mathematics of Diffusion, 2nd ed. Oxford University Press UK

[21] Shillings, C., Javier, C., LeBlanc, J., Tilton, C., Corverse, L., Shukla, A. (Submitted 2017). Experimental and Computational Investigation of Blast Response of Carbon-Epoxy Weathered Composite Materials. Composites B.

[22] Batra, R., & Hassan, N. (2007). Response of fiber reinforced composites to underwater explosive loads. Composites Part B: Engineering, 38(4), 448-468. doi:10.1016/j.compositesb.2006.09.001

[23] Wei, X., & Espinosa, H. D. (2013). Experimental and Theoretical Studies of Fiber-Reinforced Composite Panels Subjected to Underwater Blast Loading. Blast Mitigation, 91-122. doi:10.1007/978-1-4614-7267-4_4

[24] Leblanc, J., & Shukla, A. (2010). Dynamic response and damage evolution in composite materials subjected to underwater explosive loading: An experimental and computational study. Composite Structures, 92(10), 2421-2430. doi:10.1016/j.compstruct.2010.02.017

[25] Leblanc, J., & Shukla, A. (2013). Underwater Explosive Response of Submerged, Air-backed Composite Materials: Experimental and Computational Studies. Blast Mitigation, 123-160. doi:10.1007/978-1-4614-7267-4_5

[26] Leblanc, J., Shillings, C., Gauch, E., Livolsi, F., & Shukla, A. (2015). Near Field Underwater Explosion Response of Polyurea Coated Composite Plates. Experimental Mechanics, 56(4), 569-581. doi:10.1007/s11340-015-0071-8

[27] ASTM Standard D2734-16. (2016). Standard Test Methods for Void Content of Reinforced Plastics. ASTM International, West Conshohocken, PA. doi:10.1520/D2734-16

[28] ASTM Standard D3039-14. (2014). Standard Test Method for Tensile Properties of Polymer Matrix Composite Materials. ASTM International, West Conshohocken, PA. doi: 10.1520/D3039_D3039M-14

[29] ASTM Standard D3518-13. (2013). Standard Test Method for In-Plane Shear Response of Polymer Matrix Composite Materials by Tensile Test of a ±45° Laminate. ASTM International, West Conshohocken, PA. doi: 10.1520/D3518_D3518M

[30] Gilat, A., Goldberg, R. K., & Roberts, G. D. (2002). Experimental study of strain-rate-dependent behavior of carbon/epoxy composite. Composites Science and Technology, 62(10-11), 1469-1476. doi:10.1016/s0266-3538(02)00100-8

[31] ASTM Standard D7137-12. (2012). Standard Test Method for Compressive Residual Strength Properties of Damaged Polymer Matrix Composite Plates. ASTM International, West Conshohocken, PA. doi: 10.1520/D7137_D7137M-12

[32] ASTM Standard D1141-98. (2013). Standard Practice for the Preparation of Substitute Ocean Water. ASTM International, West Conshohocken, PA. doi: 10.1520/D1141-98R13

[33] ASTM Standard D5229-14. (2014). Standard Test Method for Moisture Absorption Properties and Equilibrium Conditioning of Polymer Matrix Composite Materials. ASTM International, West Conshohocken, PA. doi: 10.1520/D5229_D5229M-14

[34] Gupta, S., Parameswaran, V., Sutton, M. A., & Shukla, A. (2014). Study of dynamic underwater implosion mechanics using digital image correlation. Proceedings of the Royal Society A: Mathematical, Physical and Engineering Sciences, 470(2172), 20140576-20140576. doi:10.1098/rspa.2014.0576

[35] Dobratz, B. (1972). Properties of chemical explosives and explosive simulants. Lawrence Livermore National Laboratory. doi:10.2172/4285272

[36] Rice, M. (2011). Activation Energy Calculation for the Diffusion of Water into PR-1590 and Pellethane 2103-80AW Polyurethanes. NUWC-NPT Technical Memo 11-062.

[37] Hyer, M. W., & White, S. R. (2009). Stress analysis of fiber-reinforced composite materials. Lancaster, PA: DEStech Publications, Inc.

APPENDICIES

Appendix A. Collapse Pressure Calculation

```
%=====================================================================%
%================== Collapse Pressure Prediction Program ==================%
%=====================================================================%
% Program Description:
% - Estimates the collapse pressure of a cylindrical vessel subjected to hydrostatic pressure by using
Von Mises theorem.
clc; clear all;


%% Preliminary Data
t  = 0.059  ;       % Thickness (in)
OD = 2-.095*2;      % OD (in)
%ID = 1.81; OD  = ID + 2*t;
L  = 14.0;          % Unsupported Length (in)


N  = 30;            % Number of Eigen Values
%V  = pi*(OD-2*t)^2/4*L; % Implodable Volume


%% Material
% Modulus of Elasticity (psi) and Poisson's Ratio
%E  = 10.0*10^6; nu = 0.33; % AL - 6061-T6
E  = 10.4*10^6; nu = 0.33; % AL - 7075-T6
%E  = 28.0*10^6; nu = 0.28; % SS - 316
%E  = 29.7*10^6; nu = 0.28; % HY80 Steel
%% Calculation
```

```
R = (OD-t)/2;    % Mean radius
pp = zeros(1,N); % Allocating Memory


% Von Mises cylinder
for n = 1:N


pp(n) = E*(t/R)/(n^2-1+0.5*(pi*R/L)^2)*(1/(n^2*(L/(pi*R))^2+1)^2 + ...
      t^2/(12*R^2*(1-nu^2))*(n^2-1+(pi*R/L)^2)^2 );
end


[pmin,nn] = min(pp);
pminSI    = 0.006894759086775369*pmin;


fprintf('The Predicted Buckling Pressure is : \n %f MPa (%f psi)\n',pminSI,pmin);
%fprintf('The Implodable Volume is : %f in^3 \n',V);
```

Appendix B. End Cap Design

```
%=================================================================%
%==================== End Cap Design – By Helio Matos ==================%
%=================================================================%
% Description - This Program Design an end cap for implosion experiments based on The implodable dimensions.
clc; clear;

% User Defined Dimensions
OD = 1.25;   % Outer diameter
t  = 0.035;  % Thickness
TL = 3;      % Total length
UL = 1;      % Unsupported length

CR = 14;       % O-Ring Compression Ratio
tO = 0.103;    % O-Ring Thickness (100 series)
% tO = 0.139;  % O-Ring Thickness (200 series)
% tO = 0.210;  % O-Ring Thickness (300 series)\

% Preliminaries
L  = (TL-UL)/2; % Cap's Supporting Length
ID = OD - 2*t;  % Inner Diameter

GD = ID - 2*(1-CR/100)*tO; % Groove Diameter

figure(1)
hold on
```

```
rectangle('Position',[0,-ID/2,(L-tO)/2,ID])
    x = [(L-tO)/4,(L-tO)/4]; y =[-ID/2,ID/2]; str = {ID};
    %line('doublearrow',x,y) %,'String',str); clear x y str
rectangle('Position',[(L-tO)/2,-GD/2,tO,GD])
rectangle('Position',[(L-tO)/2 + tO,-ID/2,(L-tO)/2,ID])
rectangle('Position',[-0.50,-OD/2,0.5,OD])
%axis([-L,1.2*L,-OD/1.8,OD/1.8])
daspect([1,1,1])
hold off
```

Appendix C. Pressure Conversion Function

```
%================================================================%
%================== Pressure Conversion - Helio Matos ===================%
%================================================================%
function [t, Data] = Conversion(RAW)
% This function performs the following:
%   Converts Voltage into Pressure (psi)
%   Converts Location into time (s)
%    - Good for Specimen AL1,...
global cp Fs


% Obtaining the Pressure values
CH1 = RAW(:,2)/(1.000*10^(-3)); %
CH2 = RAW(:,3)/(1.000*10^(-3)); %
CH3 = RAW(:,4)/(1.000*10^(-3)); %
CH4 = RAW(:,5)/(1.000*10^(-3)); %
CH5 = RAW(:,6)/(1.000*10^(-3)); %
CH6 = RAW(:,7)/(1.000*10^(-3)); %
CH7 = RAW(:,8)/(1.000*10^(-3)); %
CH8 = RAW(:,9)/(1.000*10^(-3)); %


figure(1)
hold on
plot(CH2,'r')


% Filtering data using high pass and low pass filters
low_cut  = 10;   % Low cutoff frequency in Hz
```

```
high_cut = 100000; % High cutoff frequency in Hz


[Bh,Ah] = butter(2,(low_cut)*2/Fs,'high');

[Bl,Al] = butter(2,(high_cut)*2/Fs,'low');


CH1 = filter(Bh,Ah,CH1); CH1 = filter(Bl,Al,CH1);

CH2 = filter(Bh,Ah,CH2); CH2 = filter(Bl,Al,CH2);

CH3 = filter(Bh,Ah,CH3); CH3 = filter(Bl,Al,CH3);

CH4 = filter(Bh,Ah,CH4); CH4 = filter(Bl,Al,CH4);

CH5 = filter(Bh,Ah,CH5); CH5 = filter(Bl,Al,CH5);

CH6 = filter(Bh,Ah,CH6); CH6 = filter(Bl,Al,CH6);

CH7 = filter(Bh,Ah,CH7); CH7 = filter(Bl,Al,CH7);

CH8 = filter(Bh,Ah,CH8); CH8 = filter(Bl,Al,CH8);


% Wavelet filter

CH1 = cmddenoise(CH1,'db4',10,'s',NaN)';

CH2 = cmddenoise(CH2,'db4',10,'s',NaN)';

CH3 = cmddenoise(CH3,'db4',10,'s',NaN)';

CH4 = cmddenoise(CH4,'db4',10,'s',NaN)';

CH5 = cmddenoise(CH5,'db4',10,'s',NaN)';

CH6 = cmddenoise(CH6,'db4',10,'s',NaN)';

CH7 = cmddenoise(CH7,'db4',10,'s',NaN)';

CH8 = cmddenoise(CH8,'db4',10,'s',NaN)';


figure(1)

plot(CH2,'b')

title('Filtered vs Unfiltered Sensor Data')
```

```
legend('Unfiltered','Filtered')

axis tight

hold off


Data = [CH1,CH2,CH3,CH4,CH5,CH6,CH7,CH8];

Data = Data' + cp + 14.7; % Absolute pressure in psi


% Obtaining time vector

duration = -2; % Time duration to record backwards in time (s)

t = duration:1/Fs:0;

t = t(RAW(1,1):RAW(end,1));

end
```

Appendix D. Free-field Pressure Analysis

```
%================================================================%
%==============Free-field Implosion Experiment - By Helio Matos ==============%
%================================================================%
% This Program:
% 1 - Converts RAW data from the DAQ to usable pressure and time values.
% 2 - Plots Pressure Values


clc; clear all; clf;
%% 1 - Converting Raw Data


% Import Raw Data
%Specimen=inputdlg('Name a .mat raw voltage data:','Import Raw Data',1);
%Specimen=char(Specimen);
%load(Specimen);
global cp Fs t_shift


load('exp10_data.mat'); % Loads Experimental Sensor and DIC Values


%% ==================== Sensor Analysis ======================== %%
% Converting Voltage Values to SI units and filtering the data:
Fs = 2*10^6;  % Sampling rate of the Astro-Med (Hz)
cp = 243;     % Collapse pressure of tube (psi)
t_shift = -0.2854215; % Adjusted Sensor Time vector


L  = 15*25.4;      % Unsupported Length of Specimen (mm)
[t, Data] = Conversion(RAW); clear RAW;
```

```
figure(2)
hold on
plot(t,(Data(1,:)));
%plot(t,(Data(1,:)),'r',t,(Data(2,:)),':r',t,(Data(3,:)),':b',t,(Data(4,:)),'b');
%plot(t,(Data(5,:)),'r',t,(Data(6,:)),':r',t,(Data(7,:)),':b',t,(Data(8,:)),'b');
xlabel('Time (ms)')
ylabel('Normalized Pressure (P/P_c_r)')
title('Pressure Profile of the Center of the Specimen')
axis([-2,1.5,0.6,1.9]);
hold off

% Sensor locations
% All Sensor Locations: [-L/2,-L/3,-L/6,0,L/6,L/3,L/2]
y   = [-L/2,-L/6,0,L/6,L/2];          % Used sensor location in meters
y90 = [-L/2,-L/6,0,L/6,L/2];  % Used sensor location in meters
yy  = min(y):max(y)/50:max(y);

P0_y  = [Data(4,:);Data(2,:);Data(1,:);Data(2,:);Data(4,:)]; % Normalized Pressure
P90_y = [Data(8,:);Data(6,:);Data(5,:);Data(6,:);Data(8,:)]; % Normalized Pressure

P0_yy  = zeros(length(yy),length(Data(1,:))); % Allocating Memory
P90_yy = zeros(length(yy),length(Data(1,:))); % Allocating Memory

for i = 1:length(Data(5,:))
   P0_yy(:,i) = pchip(y,P0_y(:,i),yy);
   P90_yy(:,i) = pchip(y90,P90_y(:,i),yy);
```

```
end


figure(3)
imagesc(t,yy,P0_yy);
colormap jet; set(gca,'YDir','normal');h = colorbar;
ylabel('Tube Length (mm)'); xlabel('Time (ms)');
ylabel(h,'Normalized Pressure (P/P_c_p)');
title('Pressure History Map - 0 deg');
caxis([0.6 1.7])
axis([-2,1.5,min(y),max(y)]);


figure(4)
imagesc(t,yy,P90_yy);
colormap jet; set(gca,'YDir','normal');h = colorbar;
ylabel('Tube Length (mm)'); xlabel('Time (ms)');
ylabel(h,'Normalized Pressure (P/P_c_p)');
title('Pressure History Map - 90 deg');
caxis([0.6 1.7])
axis([-2,1.5,min(y),max(y)]);
```

Appendix E. Confinement Pressure Analysis

```
%=================================================================%
%======== Implosion Inside an Enclosed Tube Experiment - By Helio Matos =========%
%=================================================================%
% This Program:
% 1 - Converts RAW data from the DAQ to usable pressure and time values.
% 2 - Plots Pressure Values


clc; clear all;
%% 1 - Converting Raw Data


% Import Raw Data
%Specimen=inputdlg('Name a .mat raw voltage data:','Import Raw Data',1);
%Specimen=char(Specimen);
%load(Specimen);
global cp Fs


load('data.mat'); % Loads Experimental Sensor and DIC Values


%% ==================== Sensor Analysis ====================== %%
% Converting Voltage Values to SI units and filtering the data:


Fs = 2*10^6;  % Sampling rate of the Astro-Med (Hz)
[t, Data] = Conversion(RAW); clear RAW;
savefig('CH2')


%% Hammer Impulse
```

```
% A_cs = 0.0248258; % Cross Sectional Area of Open Tube
Ps = (Data(5,:)-Data(5,1))*6894.75729; % Dynamic Pressure in PA
Ph = (Data(2,:)-Data(2,1))*6894.75729; % ""

figure (2)
hold on
plot(Ps,'r')
plot(Ph,'b')
ylabel('Pressure (MPa)'); xlabel('Time (ms)');
axis tight

% %% Max Impulses
% clc
% s_start  = 9529;
% s_finish = 19340;
%
% h_start  = s_start;
% h_finish = s_finish;
%
% Ismax = max(cumtrapz((t(s_start:s_finish)-t(s_start)),(Ps(s_start:s_finish)-Ps(s_start))))
% Ihmax = max(cumtrapz((t(h_start:h_finish)-t(h_start)),(Ph(h_start:h_finish)-Ph(h_start))))
%
% EI = Ismax^2*pi*0.1778/1000
% Eh = Ihmax^2*pi*0.1778/1000
% %%
%
%
% figure (3)
```

```
% plot(t*1000,Is,'b',t*1000,Ih,'r')
% ylabel('Impulse (Pa?s)'); xlabel('Time (ms)');
% legend('Specimen Impulse','Hammer Impulse')
% axis tight

%% Sensor locations
% All Sensor Locations: [0,4,12,20,27,34,38,44] in inches
y  = [0,4,27,34,38,44]*0.0254;     % Used sensor location in meters
yy = min(y):max(y)/100:max(y);

P_y  = [Data(2,:);Data(3,:);Data(5,:);Data(6,:);Data(7,:);Data(8,:)]/(cp+14.7); % Normalized Pressure
P_yy = zeros(length(yy),length(Data(1,:))); % Allocating Memory

for i = 1:length(Data(5,:))
   P_yy(:,i) = pchip(y,P_y(:,i),yy);
end

figure(3)
imagesc(t*1000,yy,P_yy);
colormap jet; set(gca,'YDir','normal');h = colorbar;
ylabel('Tube Height (m)'); xlabel('Time (ms)');
ylabel(h,'Normalized Absolute Pressure (P/P_c_p)');
axis([0,15,0,max(y)]);
savefig('Pressure_evolution')

%% FFT Analysis
L    = length(P_y(1,:));              % Length of the Signal
```

```
NFFT = 2^(nextpow2(L)+ 3);              % Next power of 2
freq = Fs/2*linspace(0,1,NFFT/2+1);     % Frequency Vector

G = zeros(length(yy),length(freq)*2-2); % Allocating Memory
G_max = 0;

% High Pass Filter
low_cut  = 100;
[Bh,Ah] = butter(2,(low_cut)*2/Fs,'high');

for i = 1:length(yy)
   G(i,:) = fft(filter(Bh,Ah,P_yy(i,:)),NFFT)/L;     % Gain

   m = max(2*abs(G(i,:)));
   if m > G_max
   G_max = m;
   end
end

G_abs = 2*abs(G(:,1:NFFT/2+1));

figure(4)
imagesc(freq,yy,G_abs/G_max);
colormap jet; set(gca,'YDir','normal');h = colorbar;
ylabel('Tube Height (m)'); xlabel('Frequency (Hz)');
ylabel(h,'Normalized Gain');
axis([0,1000,0,max(y)]);
```

```
%savefig('Frequency_plot')

%save('matlab_workspace')
```

Appendix F. Volumetric Flow and Energy Calculation

```
%=================================================================%
%============ Volumetric Flow and Energy Calculation - By Helio Matos ==========%
%=================================================================%
% This Program:
% 1 - Analyses DIC data.
% 2 - Plots volumetric displacements and Velocities


clc; clear all;
%% DIC Analysis


load('dR.mat');load('t.mat'); load('L.mat'); load('W.mat');


% Preliminary Data
fps = 40000;  % Frames per second
dt = 1/fps;   % Time step
L  = 15*25.4; % Unsupported Length of Specimen (mm)
V0 = 1113.85; % Initial Volume (cc)
V  = V0 * ones(1,length(t)); % Volume Vector
dV = 0*V;                    % Initiating change in volume;


%Write a video
writerObj = VideoWriter('implosion.avi');
open(writerObj);


% Final line segment
W3 = W1.*0;
```

```
% Locations for the line segments;
y0 = 0;
y1 = 8.383;
y2 = 16.302;
y3 = 31.75 - 1/2*dR;

h1 = waitbar(0, 'Total Time', 'Units', 'normalized', 'Position', [0.25,0.4,0.25,0.2]);
h2 = waitbar(0, 'Local Time', 'Units', 'normalized', 'Position', [0.5,0.4,0.25,0.2]);

F(length(t)) = struct('cdata',[],'colormap',[]);

for i = 1:5:length(t)
   waitbar(i/length(t), h1);

   x  = [y0;y1;y2;y3(i)];   % Current Location vector
   xx = y0:y3(i)/25:y3(i);  % Refined Location vector

   A = (xx(2)-xx(1))*(y(2)-y(1));
   W = [W0(:,i),W1(:,i),W2(:,i),W3(:,i)];

   WW = zeros(length(xx),length(W0(:,i))); % Allocating Memory

   for j = 1:length(y)
      WW(:,j) = pchip(x,W(j,:),xx);
```

```
    for s = 2:length(WW(:,1))
        for k = 2:length(WW(1,:))
            U1 = WW(s-1,k-1);
            U2 = WW(s  ,k-1);
            U3 = WW(s-1,k  );
            U4 = WW(s  ,k  );

            U =(U1 + U2 + U3 + U4)/4;
            dV(i) = dV(i) + 4*A*U*0.001; % change in Volume in cc
        end
    end

    waitbar(j/length(y), h2);
end

figure(1)
hold on
imagesc(y,xx,WW);
imagesc(y,-xx,WW); box off
hold off
axis equal
colormap(flipud(jet));
set(gca,'YDir','normal');h = colorbar;
caxis([-30 0])
axis image
daspect([1,1,1])
F(i) = getframe(gcf);
writeVideo(writerObj,F(i));
```

```
end


close(h1); close(h2);

V = V + dV./100;


figure(2)

plot(t*1000,V);

axis([min(t) max(t) 0 V0])

xlabel('Time (ms)')

ylabel('Volume (cc)')

axis([-2.5 2 0 1113.85]);


dVdt = [0, -diff(V)./(dt*1000)];          % volumetric rate (cc/ms)


figure(3)

plot(t*1000,dVdt);

xlabel('Time (ms)')

ylabel('Volumetric Rate (cc/ms)')

axis([-2.5 2 -100 900 ]);


% movie(figure,F,1)
```